PhD-FSTC-2014-05
The Faculty of Sciences, Technology and Communication

DISSERTATION

Presented on 31/03/2014 in Luxembourg

to obtain the degree of

DOCTEUR DE L'UNIVERSITÉ DU LUXEMBOURG

by

M'hamed Rabie Djemour
Born on 9 April 1982 in Nabeul (Tunisia)

$Cu_2ZnSnSe_4$ polymorphs and secondary phases: characterization by Raman spectroscopy and photoluminescence

Contents

Introduction

"We are like tenant farmers chopping down the fence around our house for fuel when we should be using nature's inexhaustible sources of energy sun, wind and tide. ...
I'd put my money on the sun and solar energy. What a source of power!
I hope we don't have to wait until oil and coal run out before we tackle that."

Thomas Edison 1931 [1]

Renewable energy will play a crucial role in securing our energy needs in the future. It is projected that even with high growths in nuclear and wind energy, the electricity supply will fail to meet the rapidly growing needs of the worlds increasing population if actual CO_2 targets stay unchanged [2]. Depending on the CO_2 targets, shortages in the order of a few, to tens of terawatts[1] can be expected [2]. Among other promising technologies, Photovoltaics (PV) is a prime candidate to close this gap.

The main PV technologies on the market are based on crystalline silicon (c-Si), cadmium telluride (CdTe) and copper indium gallium selenide ($CuIn_xGa_{1-x}Se_2$ or CIGS) materials. However most of these technologies have a theoretical maximum annual production output, based on the fact that they are composed of materials which have limited world reserves or mining capabilities. The limiting components are tellurium in the CdTe and indium in the CIGS [2]. Silver is also a limiting component of the c-Si technology as it is used as the contact material. However some alternatives are being investigated. This shortage is further emphasized by their use in competing technologies, as is the case of silver and indium (which is widely used in the displays of consumer electronics). Gallium and indium are mainly produced in China and are not, or not sufficiently, recycled. They are therefore considered 'critical' materials by the EU i. e. economically important materials whose supply risks interruption [3]. Simply put: the production of today's PV technologies depends on the availability of scarce and potentially expensive materials.

[1] 1 terawatt $\approx$ 1000 nuclear reactors

The long term sustainability of PV production could be increased by switching to technologies that are based on abundant materials which are independent of geopolitical considerations. $Cu_2ZnSn(S,Se)_4$ (CZTS/Se) fulfills the above prerequisites while having the necessary properties to be suitable as a thin film solar cell absorber. It is therefore studied in this thesis.

The CZTS/Se crystal is a semiconductor that is intrinsically p-doped and has a direct band gap, and therefore has sufficiently high absorption coefficients for thin film solar cells ($> 10^4\, cm^{-1}$ [4]). The band gap can be tuned to reach maximum theoretical efficiencies above 30 % [5] by changing the S/Se ratio or by incorporating other elements such as Ge or Si. Finally, the biggest advantage of the CZTS/Se is that one can simply exchange the CIGS layer with a CZTS/Se layer to gain a working solar cell. This is possible as CZTS/Se conveniently has a suitable band alignment with the other layers of the CIGS solar cells. The already optimized substrates, buffer and window layers can be kept as they are, while the replaced absorber material i. e. CZTS/Se can be optimized.

CZTS/Se solar cells have already achieved an efficiency of 12.6 % [6]. In this project, pure selenide CZTSe absorbers are studied, motivated by the fact that the quaternary pure selenide system has demonstrated record efficiencies of 9.2 % by Repins et. al. [7] and 9.7 % by Brammertz et. al. [8] while being easier to study, since less secondary phases than in the pure sulfides (CZTS) or the mixed sulfur-selenides (CZTS/Se) can be expected [9, 10]. However, compared to other solar cell absorbers, a high number of secondary phases is still possible as the four composing elements (i. e. copper, zinc, tin and selenium) can form several unwanted binaries and ternaries. Also, only a small range of composition yields single phase CZTSe [10].

The reported record efficiencies for pure CZTSe [7, 8] are measured on CZTSe absorbers of different band gaps (0.96 eV and 1 eV as extracted from photoluminescence, respectively) although they were supposed to be the same material. This difference in band gaps is usually explained by a different order of the composing elements leading to crystal structures from other space groups (polymorphs) which have different band gaps.

The above discussed possibility of various polymorphs and secondary phases implies the importance of possessing tools to discernate the phases that tend to form whilst CZTSe is grown. This is one main goal of this thesis.

The main measurement techniques employed during this thesis are Photoluminescence (PL) and Raman spectroscopy. Both are optical, contact-less and non-destructive characterization techniques. Following on from the first chapter which provides relevant background information about the different polymorphs, secondary phases and measurement techniques used, the second chapter introduces the setup and the sample preparation techniques.

The third chapter reports the first results of this thesis: the discrimination of secondary phases encountered during the growth of CZTSe solar cell absorbers by Raman and PL. Chapter four discusses the Raman spectrum of CZTSe, especially focusing on the asymmetry of the mode of highest intensity, looking at the origins of this broadening. Additionally, a polarization and orientation Raman study is presented assigning the modes to their symmetry, therefore allowing the differentiation between crystals from various polymorphs. The next chapter examines the luminescences attributed to CZTSe. An intensity dependent PL study assigns the various luminescences encountered to a mixture of band gaps. In the final chapter, the findings reported on in this thesis are briefly summarized and discussed in the context of the ongoing research on the subject matter.

Chapter 1

Background

1.1 $Cu_2ZnSnSe_4$: multiple polymorphs

The main focus of this thesis is the compound $Cu_2ZnSnSe_4$ (CZTSe) which can have the same crystal structure as naturally occurring minerals: kesterite ($Cu_2(Zn,Fe)SnS_4$) or stannite (Cu_2FeSnS_4). The four elements Cu, Zn, Sn, and Se crystallize in a tetragonal structure where anions and cations are arranged in tetrahedral bonds similar to the zincblende structure. Different polymorphs given by varying the arrangement of the cations in the unit cell are introduced. Their calculated stabilities and band gaps are summarized when available in literature. A second part of the chapter introduces the experimental methods used to characterize CZTSe films in this thesis: Raman spectroscopy and Photoluminescence. A further complication during the growth of CZTSe is the occurrence of secondary phases. The properties of these phases are summarized in the last part of the chapter.

Structure

The compound material CZTSe can be seen as a modification of ZnSe where the cations are substituted, keeping the valence state constant and the charge neutral (schematized in figure 1.1). This substitution is based on postulations by Lewis [11] and Pauling [12] and was developed by Goodman [13] and Pamplin [14]. It first results in the ternary $CuInSe_2$ by doubling the unit cell and substituting the group II element Zn by group I and III elements Cu and In while keeping the basic elements of the crystal structure. In a second step, the group III element In is substituted by group II and IV elements Zn and Sn still retaining the tetrahedral coordination. This succession of substitutions suggests that different cation orderings are possible since Zn and Sn for example can be arranged in different ways leading to crystal structures from

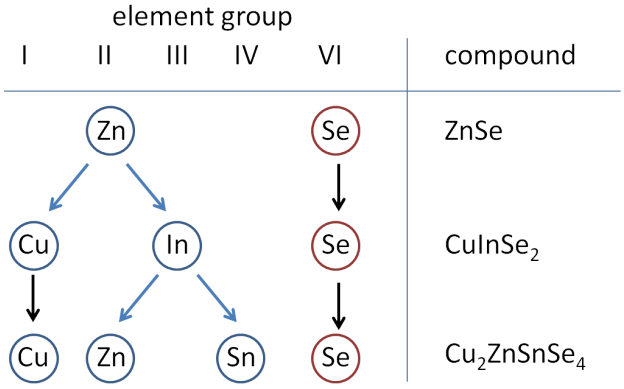

Figure 1.1: schematic representation of the isoelectronic substitution from ZnSe to CZTSe; from binary II-VI to quaternary I_2-II-IV-VI_4 compounds.

different space groups. This polymorphism is discussed below (for further details see [15]).

Possible polymorphs and their stability are discussed by Paier et. al. citePaier2009 and Ichimura et. al. citeIchimura2009, these two publications compare the stabilities of a large number of possible polymorphs. The phases discussed by Paier et. al. [16] are kesterite (space group $I\bar{4}$ (S^2-4; No. 82)), stannite (space group $I\bar{4}2m$ (D^{11}_{2d}; No. 121)), and three further structural modifications belonging to the space groups $P\bar{4}2_1m$ (D^3_{2d}; No. 113), $P\bar{4}2c$ (D^2_{2d}; No. 112) and $P2$ (C^1_2 No. 3) [16, 17]. These crystal structures are shown in figures 1.2 and 1.3.

In all the polymorphs of CZTSe, the selenium atoms are layered in the z=1/8, z=3/8, z=5/8 and z=7/8. The kesterite structure is composed of alternating CuSn (z=0, z=1/2 and z=1) and CuZn(z=1/4 and z=3/4) layers while stannite is composed of alternating ZnSn and Cu layers (shown respectively in figures 1.2 (a) and (b)). More than one representation of the unit cell is possible. Different representations can be found in literature: for instance the stannite unit cell in [15] is represented with a pure copper layer at z=0.

Kesterite and its variation from space group $P\bar{4}2c$ have the same layer stacking only differing in the orientation of the CuZn pairs. The CuZn layers are identical in the $P\bar{4}2c$ structure while they are rotated by 90° to each other in the kesterite unit cell. In the $P\bar{4}2c$ structure the Zn atoms are on one plane parallel to the c-axis of the unit cell (compare figures 1.3a and 1.3b).

The structures $P\bar{4}2m$ and $P2$ as discussed by Paier et. al. do not fulfill the charge neutrality: each chalcogen atom (S or Se) should always be bonded

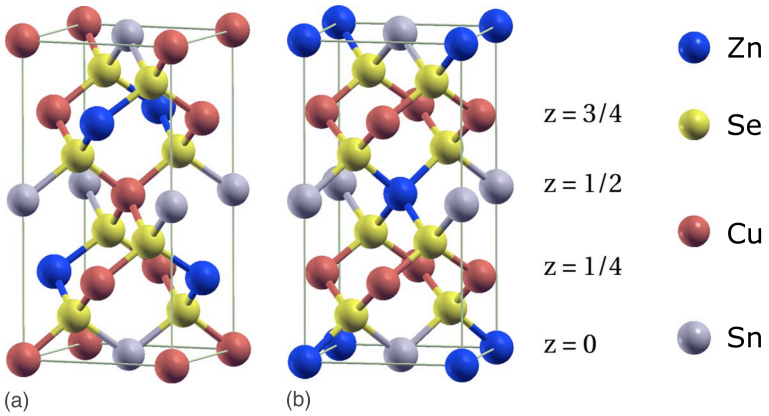

Figure 1.2: Unit cell representations of the CZTSe polymorphs: kesterite a) and stannite b). Taken from [16]

to two Cu, one Zn, and one Sn atom. These structures not following the so called octet rule are not further discussed.

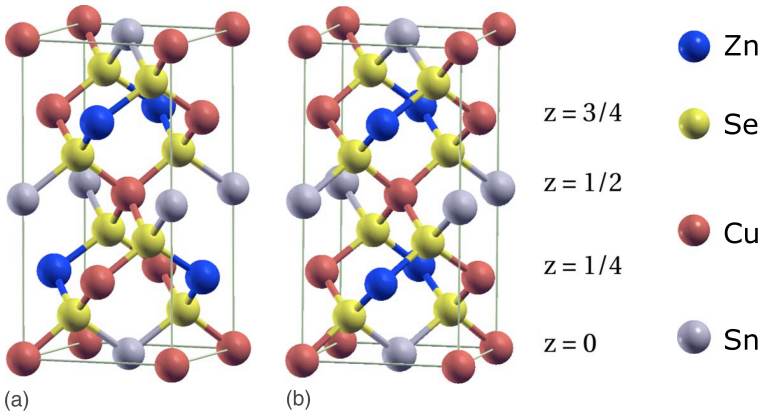

Figure 1.3: Unit cell representations of the kesterite CZTSe (a) and its modification from space group $P\bar{4}2c$ (b). Taken from [16]

Ichimura et. al. [18] discussed a slightly different group of structures: kesterite, stannite, $P\bar{4}2c$, $P\bar{4}2m$ and a further modification (not discussed by Paier et. al.) which consists of modifying the z=1/2 plane of the unit cell. The unit cell of the first modification of the kesterite structure schematized in figure 1.4c, differs from the kesterite only by moving the z=1/2 plane by 1/2 a in both x and y direction i.e. the CuSn layers at: z=0; 1/2; 1 are all identical in this structure. The second modification is a modification of the stannite structure namely $P\bar{4}2m$ (D^1_{2d}; No. 111) where the z=0 and 1/2 layers are the same. This modification has a cubic structure (see figure 1.4d).

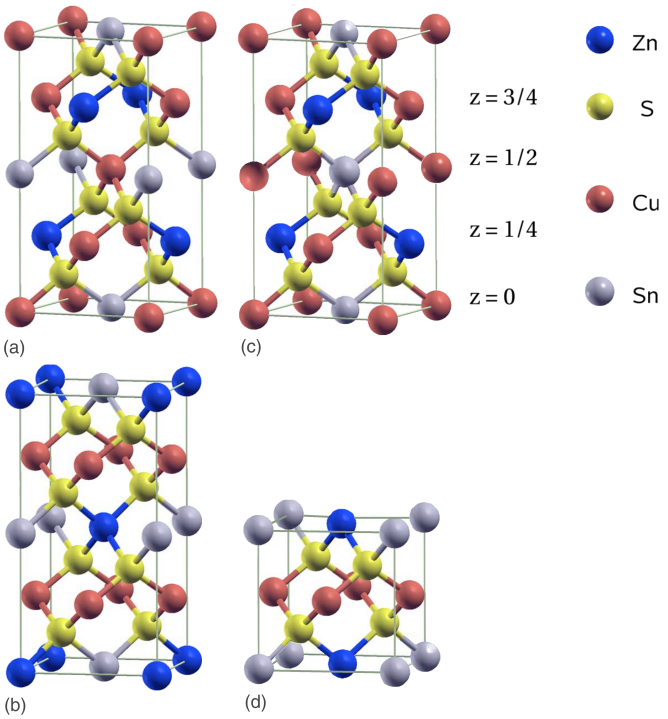

Figure 1.4: Unit cell representations of the CZTSe polymorphs: kesterite (a), stannite (b), modification of kesterite (c), modification of stannite: $P\bar{4}2m$ as discussed by Ichimura et. al. [18].

Another structure discussed in literature is the so called disordered kesterite. From neutron scattering measurements [17] one can find that the Cu and Zn atoms in z=1/4 and z=3/4 layers are exchanged. Assuming the atoms in those layers are randomly distributed, one can see them as as new atoms with averaged properties which leads to a structure from space group $I\bar{4}2m$ (D_{2d}^{11}; No. 121)). This latter space group is the same one as for stannite CZTSe.

Figure 1.5 compares the disordered kesterite and the stannite structures: the unchanged Cu atoms compared to kesterite (i. e. the Cu atoms on the corners and in the center of the unit cell) are on the 2a position, while for stannite this position is occupied by Zn atoms. The Cu/Zn atoms are on the 4d position which is occupied by copper in stannite. The Sn atoms are on the 2b position for both structures (the Wyckoff positions are further treated in section 1.2.4).

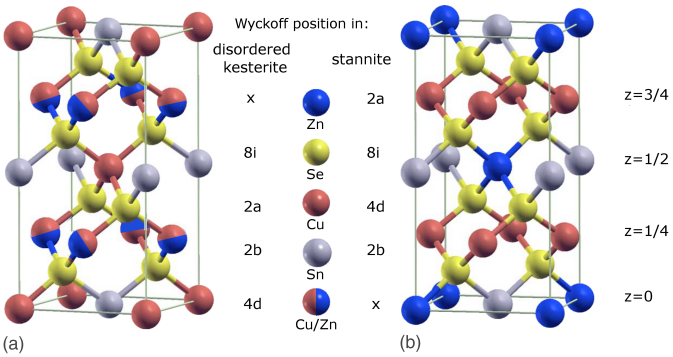

Figure 1.5: Representations of CZTSe Unit cells: disordered kesterite figure a), and stannite figure b). The occupied Wyckoff positions for both structures are indicated.

The stability of the polymorphs discussed earlier (except for the disordered kesterite) is calculated for CZTS and summarized in table 1.1.

		Paier [16]		Chen [19]	Ichimura [18]
structure	see figure	PBE	HSE	HSE	GGA
kesterite $I\bar{4}$	1.2a	0	0	0	0
stannite $I\bar{4}2m$	1.2b	46	54	2.9	3.3
$P\bar{4}2c$	1.3c	5	12	3.2	9.5
modification	1.4c	-	-	-	2.1
$P\bar{4}2m$	1.4d	-	-	-	4.4

Table 1.1: Stabilities of CZTS polymorphs as computed by DFT and expressed in meV/atom relative to the most stable structure (Kesterite).

The calculations by Paier et. al. [16] suggest that the $P\bar{4}2c$ is actually slightly more stable than the stannite phase which is opposed to the results of Ichimura et. al. [18] and Chen et. al. [19] who calculated a higher stability for the stannite than for the $P\bar{4}2c$. Ichimura et. al. also found out that the unspecified modification has a higher stability than the stannite and that the $P\bar{4}2m$ is more stable than the $P\bar{4}2c$.

These different structures discussed above are never discussed together. Usually the structure and band gap DFT calculations in literature only refer to kesterite and stannite pointing out that these structures are the most stable ones. This is plausible since the closely related naturally occurring minerals grow in the kesterite and stannite crystal structures, which suggests that these structures have the lowest formation energies.

It should be noted that the calculations presented in table 1.1 are made for the sulfide compound. For CZTSe the stability of the different polymorphs is only calculated for kesterite, stannite and the $P\bar{4}2c$. From the binding energy per atom calculations by Chen et. al. [19] and Persson et. al. [20] it follows that kesterite is the most stable compound followed by stannite (3.8 meV/atom and 3.3 meV/atom respectively). Maeda et. al. [21] confirm this order of stability since their calculated formation energy enthalpy difference between stannite and kesterite ordered CZTSe is 14.5 meV/atom. Chen et. al. [19] found the difference in binding energy for the $P\bar{4}2c$ structure compared to kesterite to be 5.5 meV/atom. According to these values the $P\bar{4}2c$ structure is less stable than the stannite structure.

Band gap

The different polymorphs have different band gaps which can be detrimental for the solar cell as will be shown in section 5.2. A few band gap calculations for CZTSe are available in literature. They are summarized in table 1.2. The DFT and GW calculations show that the band gap of kesterite CZTSe is higher (at around 1 eV) than the stannite band gap by around 150 meV. The $P\bar{4}2m$ structure was only considered by Chen et. al. [19] who found that it has an even lower band gap than the stannite.

	Chen et. al. [19]	Persson et. al. [20]	Botti et. al. [22]
structure	GGA (HSE)	GGA	GW
kesterite	0.96	1.05	1.02
stannite	0.82	0.89	0.87
$P\bar{4}2m$	0.79		

Table 1.2: CZTSe band gaps calculated by DFT (in eV).

1.2 Raman spectroscopy

This section briefly discusses the fundamental concepts of inelastic Raman light scattering. Besides the basics of Raman spectroscopy, a short introduction to group theory is given as it is needed for the interpretation of the data.

The Raman effect is based on the inelastic scattering of light with optical modes of quasi particles. Typical scatterers are phonons, but magnon, plasmons and electric excitations could also play a role. It was first detected by Sir Chandrasekhara Venkata Raman in 1928 [23].

Since the number of phonon modes and their energies are characteristic to the considered material, Raman spectroscopy can be used to identify the different compounds present in the investigated sample. This sensitivity to the structure and elemental composition of the material measured can help differentiate the polymorphs and secondary phases of CZTSe.

Raman measurements probe the zone center phonons. This is a direct result of the momentum conservation relating the wavevector $\vec{q}$ of the phonon with the momenta of incident $\vec{k_i}$ and scattered $\vec{k_s}$ light, respectively. It is given by: $\vec{k_i} - \vec{k_s} = \vec{q}$ and schematized in figure 1.6. Applying momentum conservation for the back scattering geometry ($\theta = 180°$) gives the maximum transferable momentum by light scattering (q_{max}). It is given by: $q_{max} \approx 2k_i$. The wave number $k_i = |\vec{k_i}|$ of light is given by $2\pi/\lambda$ while the maximum momentum (in the brilloin zone) is given by the length of the zone boundary wavevector given by: $2\pi/a$, where a is the lattice parameter. As the lattice parameter is orders of magnitude smaller than the wavelength of light (5 Åvs. 5000 Å), only phonons with momenta of a fraction of the maximum momenta (in the Brilloin zone) are involved in the scattering process (phonons near the zone center ($q \approx 0$))[24].

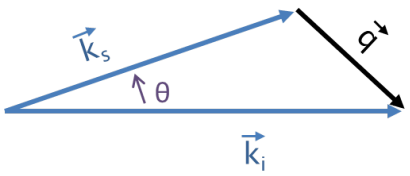

Figure 1.6: Scheme of momentum conservation for an inelastic light scattering event resulting in the creation of a phonon; $\vec{k_i}$, $\vec{k_s}$, and $\vec{q}$ are the momenta of the incident and scattered photons and the created phonon, respectively.

1.2.1 The Semi-classical model

The interaction of light with a vibrating crystal is discussed in the classical model. This section closely follows the book of Yu and Cardona [25].

In the classical model the interaction of matter with the electric field[1] $\vec{E}(\vec{r},t) = \vec{E}_i(\vec{k}_i,\omega_i)\cos(\vec{k}_i\cdot\vec{r}-\omega_i t)$ of the incident radiation results in an induced polarization following:

$$\vec{P}(\vec{r},t) = \chi(\vec{k}_i,\omega_i)\vec{E}_i(\vec{k}_i,\omega_i)\cos(\vec{k}_i\cdot\vec{r}-\omega_i t) \tag{1.1}$$

where χ is the susceptibility[2] represented by a second rank tensor giving the response of the system in all three dimensions, ω_i the frequency, and $\vec{k}_i$ the wave vector of the incident radiation.

The $\vec{k}$ and ω dependence of the susceptibility are due, among other responses, to atomic vibrations which in a crystal, are quantized into phonons, which can be expressed as plane waves:

$$\vec{Q}(\vec{r},t) = \vec{Q}(\vec{q},\omega_0)\cos(\vec{q}\cdot\vec{r}-\omega_0 t) \tag{1.2}$$

with wavevector $\vec{q}$ and frequency ω_0.

Using the adiabatic approximation, which in this case means assuming that the electronic frequencies are much higher than the frequency of the lattice vibrations, gives that χ is a function of $\vec{Q}$. This approximation can be understood as follows: the electronic levels are not disturbed by the vibration of the atom i. e. the electron cloud follows the movement of the atom instantaneously.

Since the amplitude of the vibration is low compared to the lattice constant, a Taylor expansion of the susceptibility χ in the lattice vibration $\vec{Q}(\vec{r},t)$ is carried out. It is evaluated at the rest position of the crystal:

$$\chi(\vec{k}_i,\omega_i,\vec{Q}) = \chi_0(\vec{k}_i,\omega_i) + \left.\frac{\partial\chi}{\partial\vec{Q}}\right|_0 \cdot \vec{Q}(\vec{r},t) + \cdots, \tag{1.3}$$

where χ_0 is the part of the susceptibility unperturbed by the atomic vibrations. Substituting equation 1.3 into equation 1.1 gives an expression for the polarization response to an external harmonic electromagnetic field in the presence of atomic vibrations. Using the trigonometric identitiy:

$$\cos\theta\cdot\cos\varphi = 1/2\cdot[\cos(\theta-\varphi)+\cos(\theta+\varphi)]$$

[1] Most books treat single molecules and not crystals. The same derivation is made using the dipole moment instead of the polarization and the polarizability instead of the susceptibility.

[2] The susceptibility is defined as the response of the polarization of a medium to an applied electric field, similar to the response of the dipole moment of a particle or a molecule to an applied electric field.

the polarization simplifies to:

$$\begin{aligned}\vec{P}(\vec{r},t,\vec{Q}) \approx\ & \chi_0\vec{E}(\vec{r},t) \\ & + \frac{1}{2}\frac{\partial\chi}{\partial\vec{Q}}\bigg|_0 \cdot \vec{Q}(\vec{q},\omega_0)\vec{E}_i(\vec{k}_i,\omega_i)\cos[\underbrace{(\vec{k}_i-\vec{q})\cdot\vec{r}-(\omega_i-\omega_0)t}_{\text{Stokes shift}}] \\ & + \frac{1}{2}\frac{\partial\chi}{\partial\vec{Q}}\bigg|_0 \cdot \vec{Q}(\vec{q},\omega_0)\vec{E}_i(\vec{k}_i,\omega_i)\cos[\underbrace{(\vec{k}_i+\vec{q})\cdot\vec{r}-(\omega_i+\omega_0)t}_{\text{anti-Stokes shift}}]\end{aligned} \tag{1.4}$$

Actually, equation 1.4 describes the different contributions of scattered light since oscillating polarization results in emitted radiation. The first term has the frequency of the dipole induced by the incident light, representing the elastically scattered light, referred to as Rayleigh scattering. The resulting radiation of the polarization described in the second and third term is shifted in frequency and wavevector and is referred to as Stokes and anti-Stokes radiation. The Stokes process can be seen as an energy loss of the incident radiation due to the creation of a phonon while the anti-Stokes process can be seen as the annihilation of a phonon.

Equation 1.4 shows that the phonon energies are measured as shifts of the energy of the incident radiation. Therefore they are usually given in relative spectroscopic units[3] to be independent of the excitation wavelengths.

Higher orders in equation 1.3 lead to induced polarizations which are shifted from the laser frequency by the sum and/or difference of multiple phonon energies. If multiple phonons of the same energy are involved, the Raman shift is called an overtone.

This classical derivation has many deficiencies. For example the Stokes and anti-Stokes radiations are predicted to have the same intensity. This is not the case since the derivation neglects the Boltzmann factor describing the temperature dependent population of excited vibrational states.

The quantum mechanical approach solves these problems. A detailed derivation can be found for example in the book of Derek A. Long [26].

[3]Spectroscopic energy unit: $(\mathrm{cm}^{-1}) = \frac{1}{\lambda_{laser}(\mathrm{cm})} - \frac{1}{\lambda_{Raman}(\mathrm{cm})}$.

1.2.2 Raman tensor and selection rules

The intensity of the scattered light is given by the power per area radiated by the oscillating polarization, averaged over time. Assuming the harmonic oscillator approximation, the Stokes/anti-Stokes Raman transition intensity is given by:

$$I_{\nu_{\text{Stokes}}} \sim (\omega_i - \omega_0)^4 \cdot \left| \vec{e}_s \cdot \left(\frac{\partial \chi}{\partial \vec{Q}} \bigg|_0 \cdot \vec{Q}(\omega_0) \right) \cdot \vec{e}_i \right|^2 \tag{1.5}$$

The polarizations of the incident and scattered light are denoted as $\vec{e}_i$, and $\vec{e}_s$.

In equation 1.5, $\frac{\partial \chi}{\partial \vec{Q}}\big|_0$ is a third rank tensor for the derivative of the susceptibility in the three dimensions (given by a 3×3 matrix) for all possible phonon modes (the third dimension of the tensor). For an individual mode, a second rank tensor (3×3 matrix) can be given: by introducing a unit vector parallel to the atomic displacement induced by a phonon, the second rank tensor of the derived polarizability is defined as:

$$\mathrm{R} = \frac{\partial \chi}{\partial \vec{Q}} \bigg|_0 \cdot \hat{Q}(\omega_0).$$

This tensor R is also called Raman tensor of that particular phonon mode. For a single phonon mode equation 1.5 transforms to:

$$I_{\nu_{\text{Stokes}}} \sim \nu^4_{Stokes} \cdot \left| \vec{e}_s \cdot \underbrace{\left(\frac{\partial \chi}{\partial \vec{Q}} \bigg|_0 \cdot \hat{Q}(\omega_0) \right)}_{\mathrm{R}} \cdot \vec{e}_i \right|^2. \tag{1.6}$$

This last equation leads to selection rules: the derivative of the polarizability resulting from phonon vibration needs to be different from zero so that the resulting Stokes/anti-Stokes shifts can be different from zero.

Depending on the polarization of the incident light, the Raman tensor of a given phonon can be used to predict the intensity of the scattered light depending on its polarization. Using group theory one can predict the symmetry, the number and the vibrating sites of the phonons that are possible for a given crystal structure. In other words, group[4] theory can predict the non zero entries of the derivated polarizability tensor by considering the possible symmetry operations in the crystal.

[4] A group is a set of elements plus an operation relating the elements of the group while satisfying the group axioms: closure, associativity, identity and invertibility.

1.2.3 Group theory and phonon classes

The symmetry of crystals is very important for all their physical properties, it plays an important role in the phononic dispersion as it does in the electronic band dispersion. This section provides a short summary on how symmetry considerations divide the possible phonons in a space group into classes of phonons of the same symmetry. In the second part a summary of the phonon symmetries and their Raman activity is given.

Group theoretical considerations of infinite crystals divide all crystals in space groups[5] depending on a specific set of symmetry operations[6] leaving the crystal invariant. For each space group, there exists a unique set of operations defining both the space group and all possible phonon symmetries. Since more than one phonon can have the same symmetry, one can speak of a class of phonons. The phonon symmetries are tabularized in literature. The most convenient summary is given online on the Bilbao crystallographic server [27, 28, 29] where the Raman tensors are given for the classes of phonons. The finite, non zero components of the polarizability tensor are represented by different letters. The symmetry of the Raman tensor is noted in its label along with the degeneracy of the phonons and polarization of the modes. Table 1.3 provides an overview of the Mulliken Symbols and other symbols indicating the symmetry , degeneracy and the polarization of the phonons.

The Raman tensors for kesterite $I\bar{4}$ (S_4^2; No. 82) are:

$$A = \begin{pmatrix} a & 0 & 0 \\ 0 & a & 0 \\ 0 & 0 & b \end{pmatrix};\ B_z = \begin{pmatrix} c & d & 0 \\ d & -c & 0 \\ 0 & 0 & 0 \end{pmatrix};$$
$$E_x = \begin{pmatrix} 0 & 0 & e \\ 0 & 0 & f \\ e & f & 0 \end{pmatrix};\ E_y = \begin{pmatrix} 0 & 0 & f \\ 0 & 0 & -e \\ f & -e & 0 \end{pmatrix}. \tag{1.7}$$

The stannite and disordered kesterite structures from space group $I\bar{4}2m$ (D_{2d}^{11}; No.121) and the polymorphs from space groups $P\bar{4}2_1m$ (D_{2d}^{3}; No. 113),

[5] A space group is the symmetry group of a three-dimensional crystal.

[6] The symmetry elements are rotation axes, screw axes, inversion centres, mirror planes and glide planes.

and $P\bar{4}2c$ (D^6_{2d}; No. 116) have the same Raman tensors which are:

$$A_1 = \begin{pmatrix} a & 0 & 0 \\ 0 & a & 0 \\ 0 & 0 & b \end{pmatrix}; B_1 = \begin{pmatrix} c & 0 & 0 \\ 0 & -c & 0 \\ 0 & 0 & 0 \end{pmatrix}; \; B_{2z} = \begin{pmatrix} 0 & d & 0 \\ d & 0 & 0 \\ 0 & 0 & 0 \end{pmatrix}; \\ E_x = \begin{pmatrix} 0 & 0 & 0 \\ 0 & 0 & e \\ 0 & e & 0 \end{pmatrix}; E_y = \begin{pmatrix} 0 & 0 & e \\ 0 & 0 & 0 \\ e & 0 & 0 \end{pmatrix}. \tag{1.8}$$

Mulliken Symbol	
A	Symmetric with respect to the main axis of symmetry
B	Antisymmetric with respect to the main axis
E	Doubly degenerate with respect to the main axis
T	Triply degenerate with respect to the main axis
G	Fourfold degenerate with respect to the main axis
H	Fivefold degenerate with respect to the main axis
prime	Symmetric with respect to a plane of symmetry
double prime	Antisymmetric with respect to a plane of symmetry

Subscripts	
g	Symmetric with respect to the center of symmetry
u	Antisymmetric with respect of the center of symmetry
1,2	Symmetric or antisymmetric with respect to a rotation axis
x,y,z	Indicate the polarization direction of the modes

Table 1.3: Summary of the Mulliken Symbols and other symbols indicating the symmetry and degeneracy of phonons [30].

1.2.4 Raman active phonons

The total number of modes in the crystal is given by $\Gamma_{Total} = 3n$ where n is the number of atoms in the primitive unit cell. To calculate the number of atoms in the primitive cell, the number of atoms in the unit cell needs to be divided by a factor m that is given in the international symbol for the space groups ($m = 1$ for P, R; $m = 2$ for A, B, C, I; and $m = 4$ for F) [30]. For CZTSe the number of atoms in the Bravais unit cell is 16 (as can be seen in figure 1.4). Applying the above rule one finds a total of 8 atoms in the primitive Wigner-Seitz unit cell, which results in a total of 24 vibrational modes.

The next part of this section describes how group theory can predict how many modes of which symmetry are expected for a crystal. When the infinite crystal is described by a unit cell, the different sites in the unit cell are split into sites of equivalent symmetry. The symmetry of these sites results in the number and symmetry of the vibrational modes associated with that site [30]. The unit cell is useful since it shows which of the possible atom sites are occupied by which atomic species while showing the symmetries of the crystal [31]. This consideration of a single unit cell instead of an infinite crystal along with screw axis, glide planes and the point group symmetry operations, defines a factor group[7] of the space group. Applying the symmetry operations of a factor group on equivalent symmetry sites either leaves the site unchanged or transferred to a site of the same symmetry [31]. The symmetry equivalent sites are the so called Wyckoff positions. In fact all possible atomic positions, in all the possible unit cells of a given space group, can be divided into Wyckoff positions i. e. into sites of equivalent symmetry. The multiplicity, i. e. the number of these symmetry equivalent unit cell atoms, is given along with a letter representing the symmetries of the site[8]. For example, kesterite CZTSe space group $I\bar{4}$ has four Cu atoms on the 2a and 2c sites, two Sn atoms on the 2b sites, two Zn atoms on the 2d sites and eight Se atoms on the 8g sites. The unit cell of CZTSe in the kesterite structure is shown with the according occupancy of the Wyckoff positions in figure 1.7.

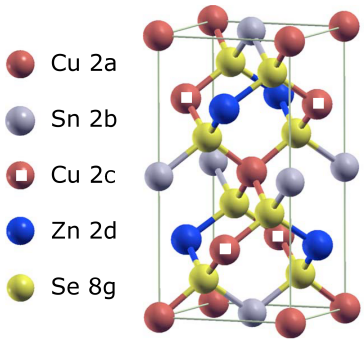

Figure 1.7: Unit cell of CZTSe in the kesterite structure. The occupancy of the Wyckoff positions is shown.

The symmetries of the Wyckoff positions define the number and the symmetries of the possible phonon modes. The total count of the phonons of different symmetries associated to Wyckoff position is its irreducible representation.

The irreducible representations for lattice vibrations of the whole unit cell

[7]The Quotient group is a subgroup of a larger group using an equivalence relation. It is usually called factor group in spectroscopy related applications of group theory.

[8]The letters are just a reference to the different symmetry equivalent sites.

(i. e. all vibrational modes in the crystal) are given by the direct sum of the irreducible representations of the Wyckoff positions defining the considered crystal. For the kesterite example the irreducible representation for lattice vibrations of the whole unit cell is [32, 28, 29]:

$$\begin{aligned}\Gamma_{total} &= B \oplus E_x \oplus E_y \text{ (2a; Cu)} \\ &\oplus B \oplus E_x \oplus E_y \text{ (2c; Cu)} \\ &\oplus B \oplus E_x \oplus E_y \text{ (2d; Zn)} \\ &\oplus B \oplus E_x \oplus E_y \text{ (2b; Sn)} \\ &\oplus 3A \oplus 3B \oplus 3E_x \oplus 3E_y \text{ (8g; Se)} \\ &= 3A \oplus 7B \oplus 7E_x \oplus 7E_y \text{ (24 modes in total)} \end{aligned} \tag{1.9}$$

The Raman or infra-red (IR) activity of the modes or their silent character depends on the selection rules described in section 1.2.2. The Raman/Infrared activities of the modes is tabularized in literature in the character table[9]. A mode is Raman active if its derived polarizability is non zero which is the case when the according coordinate transformation functions contain second order terms i. e. x^2, y^2, z^2, xy, yz or xz. This follows from group theoretical calculations [33]. For kesterite all the optical modes are Raman active.

The acoustic modes result from the in phase vibration of all atoms in the lattice which leads to vanishing energies at the Γ point[10]. Since Raman only probes the vibrational energies at the Γ point, the acoustic modes are not accessible by Raman measurements. The acoustic modes (tabulated in [28, 29]) are therefore subtracted from the total sum of vibrational modes to have the final count of the Raman active modes Γ_{Raman} [28, 29]:

$$\begin{aligned}\Gamma_{Raman} &= \Gamma_{total} - \Gamma_{acoustic} \\ &= 3A \oplus 7B \oplus 7E_x \oplus 7E_y - (B \oplus E_x \oplus E_y) \\ &= 3A \oplus 6B \oplus 6E_x \oplus 6E_y \text{ (21 Raman active modes)} \\ &= 3A \oplus 6B \oplus 6E \end{aligned} \tag{1.10}$$

It should be noted that the notation *6E* implies 6 doubly degenerated E symmetry modes i. e. 6 different mode energies but 12 phononic vibrations.

For the stannite structure, the zone center phonon representation is:

$$\Gamma_{Raman} = 2A_1 \oplus 2B_1 \oplus 4B_2 \oplus 6E. \tag{1.11}$$

[9] A character table summarizes for a space group for each class of vibrations their symmetry, their degeneracy, the symmetry operations that define them and how the coordinates are transformed.

[10] The Γ point is the center of the Brillouin zone.

The disordered kesterite has the same zone center representation as stannite as it can be assigned to the same space group with the same occupied Wyckoff positions (with the assumption that the Cu and Zn atoms in the disordered z=1/4 and z=3/4 layers (i. e. on the 4d position) can be treated as one average atomic species, as discussed in section 1.1). It should be noted that the phonon frequencies expected for stannite and disordered kesterite are different since the Wyckoff positions are occupied by different atomic species for each structure. The expected difference between ordered and disordered kesterite lies mainly in the number of A symmetry modes (3 for kesterite and 2 for the disordered kesterite).

For the $P\bar{4}2c$ structure, which is according to simulation the third most stable structure, the zone center phonon representation can not be made. This is the case since the space group and unit cells given in [16, 17] do not coincide with the according Wyckoff positions as found in the Bilbao crystallographic server [34, 28, 29]. This leads to the assumption that either the space group determination or the plotting went wrong in the previously mentioned papers.

1.2.5 Polarization orientation Raman spectroscopy

This section discusses how polarization measurements can probe the symmetry of the different modes seen in the Raman spectrum.

Equation 1.6 (repeated for convenience):

$$I_{\text{Stokes}} \sim (\omega_i - \omega_0)^4 \cdot \left|\vec{e}_s \cdot R \cdot \vec{e}_i\right|^2.$$

shows that the intensity of the modes depends on the symmetry of the modes given by the Raman tensor, the excitation polarization, and the polarization direction of the detection.

This formula for the intensity of the Raman modes leads to an experimental technique able to assign the modes to their symmetry: polarization and orientation (P/O-Raman) dependent Raman spectroscopy. The space group of the crystal is needed to know the Raman tensors of the different phonon classes. Further, the Raman mode intensities of an oriented crystal need to be measured depending on the polarization and propagation directions of both incident and scattered light. Taking into account that the Raman tensor is oriented with respect to the crystal, the Raman mode intensities also need to be measured depending on the rotation of the crystal around the three axes of the lab coordinates. Next, the above formula is used to predict the intensity variations in dependence of the rotation and the polarization, to finally assign the modes to their symmetry by comparing experiment and calculation.

This implies that the phonons of the same symmetry have the same rotation angle dependence. This means that this method can result in an estimation of the ratios of the non zero entries of the Raman tensor, as the intensity variation depends on these ratios. It should also be noted that the different modes have different ratios of Raman tensor entries since the polarizability is phonon dependent.

A useful short hand to describe the polarization dependent Raman measurement is given by the Porto notation[35]. It consists of four letters representing the excitation propagation direction, the excitation polarization direction, the scattering polarization direction, and the scattering propagation direction, respectively. One can note that the Porto notation does not account for the crystal orientation. For a confocal measurement in a perpendicular configuration (i. e. the incoming light polarization direction and the scattered light polarization direction are perpendicular) the Porto notation is $\bar{z}(x,y)z$. This latter configuration and its Porto notation is schematized in figure 1.8.

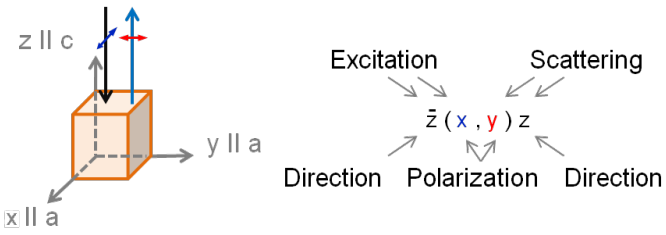

Figure 1.8: Schematic representation and corresponding short hand Porto notation for a confocal perpendicular polarization configuration Raman experiment. x, y, z represent the lab coordinates, a and c represent the lattice parameters of a tetragonal crystal.

For the polarization dependent measurement the Raman intensity I given in the last equation becomes:

$$I_{\bar{z}(x,y)z} \sim |\hat{e}_y \cdot R \cdot \hat{e}_x|^2 \tag{1.12}$$

for the perpendicular polarization configuration, and similarly:

$$I_{\bar{z}(x,x)z} \sim |\hat{e}_x \cdot R \cdot \hat{e}_x|^2 \tag{1.13}$$

for the parallel polarization configuration. $\hat{e}_x$ and $\hat{e}_y$ are the unit vectors of the lab coordinate system and R the Raman tensor.

The Raman tensor is defined for an oriented crystal. This is based purely on convention, it is usually chosen so that the excitation light propagation direction is aligned with the highest symmetry axis, as in figure 1.8.

For CZTSe it is given for a crystal aligned so that its unit cell c axis is parallel to the z direction of the lab coordinates, and one of its a axes is oriented along the lab x coordinate axis (as defined in figure 1.8). When the crystal is oriented differently, the polarizability tensor needs to be rotated by multiplication rotation matrix $Q_{(\theta/\phi/\psi)}$:

$$Q_{(\theta)} = \begin{pmatrix} \cos\theta & -\sin\theta & 0 \\ \sin\theta & \cos\theta & 0 \\ 0 & 0 & 1 \end{pmatrix};$$
$$Q_{(\phi)} = \begin{pmatrix} 1 & 0 & 0 \\ 0 & \cos\phi & -\sin\phi \\ 0 & \sin\phi & \cos\phi \end{pmatrix};$$
$$Q_{(\psi)} = \begin{pmatrix} \cos\psi & 0 & \sin\psi \\ 0 & 1 & 0 \\ -\sin\psi & 0 & \cos\psi \end{pmatrix}.$$

where θ, ϕ, ψ represent the rotations around the three axes of the lab coordinate system as defined in figure 1.9. Accordingly, the polarizability tensor R transforms to: $R_{(\theta,\phi,\psi)} = Q^T_{(\theta,\phi,\psi)} \cdot R \cdot Q_{(\theta,\phi,\psi)}$. It should be noted that the order of successive rotation is important since rotations are not commutative [36].

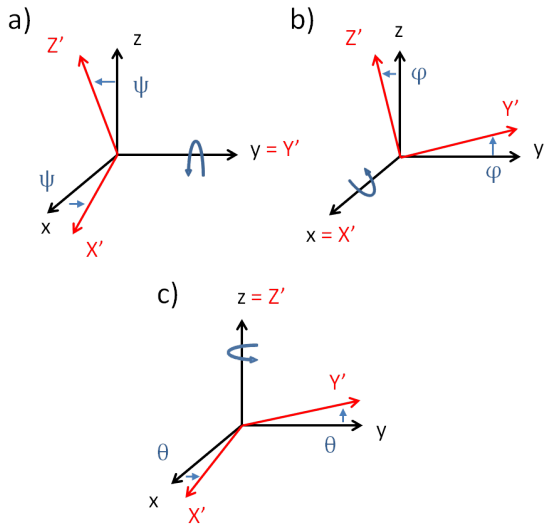

Figure 1.9: Schematic representation defining a set of rotations needed to describe a rotation of an object in 3D space: the angles θ, ϕ, and ψ are used to describe the rotations around the fixed z, x and y axes, respectively. X', Y' and Z' are the rotated local coordinates.

1.2.6 Polar mode scattering

Raman modes are either non-polar (A modes of kesterite CZTSe) or polar (all other symmetries in kesterite CZTSe). It is important to consider the interaction of polar Raman modes with the incident light since this can influence the energetic position of the modes depending on the geometry of the polarization orientation Raman measurement. This section closely follows the book by Hayes and Loudon [11] [37]. The non-polar Raman mode energies are independent of the phonon propagation direction. This is not the case for polar modes. The atomic displacement of polar Raman modes induces a dipole moment which results in a macroscopic electric field. These electromagnetic fields resulting from the vibration of polar modes influence the frequencies of these modes.

The change in mode frequency can be understood in the harmonic oscillator description of the lattice vibration where the electric field acts as an extra restoring force that increases the Raman mode energies of phonons propagating along the phonon polarization direction ξ.

According to Hayes and Loudon [37] the harmonic oscillator equation that has to be solved to get the phonon mode energies is given by:

$$\ddot{W}_\sigma + \omega_\sigma^2 W_\sigma = -\frac{N Z_\sigma(\vec{q}\cdot\vec{\xi_\sigma}) \sum_r Z_r(\vec{q}\cdot\vec{\xi_r}) W_r}{\epsilon_0 V(\kappa_{x_\infty} q_x^2 + \kappa_{y_\infty} q_y^2 + \kappa_{z_\infty} q_z^2)} \tag{1.14}$$

where ϵ_0 is the permittivity of the vacuum, V is the volume, N is the considered number of primitive cells, W is the amplitude of the vibrations of frequency ω_σ, Z is the effective charge of the vibration, $\vec{\xi}$ is the unit-vector of the polarization and κ_{i_∞} is the constant electronic contribution of the relative permittivity in the direction i. The sub-scripts r and σ indicate the direction of the polarization of the considered mode and the resulting effective charge of such a vibration. The phonon wavevector $\vec{q}$ is given by momentum conservation therefore it is parallel to the incident/scattered light directions in a confocal setup.

The right hand side of equation 1.14 is zero since for non polar modes $Z_\sigma = 0$. It is also zero for transversal modes $\vec{q}\cdot\vec{\xi_\sigma} = 0$ since $\vec{q} \perp \vec{\xi_\sigma}$. The sum in equation 1.14 couples modes of polarization vectors which are not aligned with the principal axes of the crystal, these modes have a mixed symmetry character [37]. This is not the case for CZTSe since all the polar modes of the considered polymorphs are aligned along the principal symmetry axes of the

[11] The book by Hayes and Loudon is the most complete book about Raman spectroscopy encountered during literature search.

crystal (either parallel or perpendicular to it). For example the B_z modes of kesterite CZTSe have a polarization in the z direction.

This effect of electric field coupling can lift the degeneration of polar Raman modes predicted by group theory. It is referred to as longitudinal transverse optical splitting (LO/TO) of the modes.

The example of LO/TO splitting of the triply degenerated T symmetry modes of ZnSe is discussed below: ZnSe is cubic and fully optically isotropic, the principal axes are therefore not restricted to a particular direction. All components of relative permittivity are equal. For any orientation of the crystal, and any direction of the wave-vector it is possible to choose the polarization vectors $\vec{\xi_\sigma}$ such that two are perpendicular to $\vec{q}$ and one polarization vector $\vec{\xi_\sigma}$ is parallel to $\vec{q}$ which leads to the splitting of the triply degenerate phonon mode into a transverse doublet (TO) and a longitudinal singlet (LO). The optical isotropy of the crystal leads to the independence of the phonon mode energies from the crystal orientation.

The CZTSe crystal has a distinct optical axis which is aligned parallel to its c-axis and perpendicular to the other two principal axes. For a coordinate system as discussed earlier with $z \parallel c$ and $x, y \parallel a$: the relative permittivities are $\kappa_{x_\infty} = \kappa_{y_\infty}$. Equation 1.14 can then be expressed as a function of the parallel and perpendicular relative permittivities ($\kappa_\infty^{\parallel}$ and $\kappa_\infty^{\perp}$) and of the angle θ_c between the wavevector $\vec{q}$ and the c axis. This shows that the polar mode frequencies only depend on θ_c and vary between the extremal values given by phonon mode energies for $\theta_c = 0°$ and $\theta_c = 90°$.

1.2.7 The phonon confinement model

An asymmetric broadening of some Raman peaks is often observed. It can be explained by the confinement of the phonons to a smaller volume, for example by lattice defects or small crystallites. The Phonon Confinement Model (PCM) first derived by Richter et. al. [38] and developed by Campbell et. al. [39] is a model describing the asymmetric broadening of Raman modes when the phonons are confined in space. A detailed discussion of the PCM can be found in the book by Singh et. al. [40].

The PCM explains the asymmetrical broadening of the Raman modes by the relaxation of the momentum conservation rule when the phonons are confined to a small coherent volume. A small coherent volume can be caused by a reduced particle size but it also can be limited by the presence of lattice defects which break the translational symmetry. The phonon wave function is confined in real space to a small length L, leading to a broadening in reciprocal space which is equivalent to the activation of non-centre phonons. This broadening in reciprocal space gives a momentum range $[q, q']$ centered

around the Γ point where phonons are activated. The symmetry of the broadening of the Raman modes therefore depends on the phonon density of states in the momentum range $[q, q']$ which is given by the dispersion relation of the considered mode around the Γ point. For example a maximum in the dispersion relation leads to asymmetric contributions at lower energies which is the case for most directions of the phonon dispersion of the main mode of CZTSe. This can be seen in figure 1.10 showing the calculated phonon dispersion of the Raman active A modes. For the stannite the phonon dispersion relation of the A_1 mode has a local maximum at the Γ point. For the kesterite the dispersion relation of the A mode of the highest energy is a bit more complicated: it has a maximum at the Γ point going from Γ to X, P and N, with a minimum at the Γ point going to Z. At first glance, a saddle point seems contradictory to prior statements; this is not the case since the slope of the decreasing phonon energies (Γ to X or P) is higher than the slope of the increasing phonon energies (from Γ to Z). The A modes of lower energy for both kesterite (two A modes) and stannite (the A_1 mode) exhibit the opposite phonon dispersion behavior around the Γ point i. e. a minimum at the Γ point. This would lead to an asymmetry towards higher energies.

It should be noted that the observed asymmetric broadening can also be explained by effects that lead to a shift of the Raman mode energies, if they are asymmetrically distributed in the probed volume: the resulting Raman spectrum is the sum of the shifted spectra weighted by the distribution function. These effects are: inhomogeneous laser heating [43, 44, 45], a distribution of defects or nanocrystallites, a strain distribution [46], and composition gradients [47].

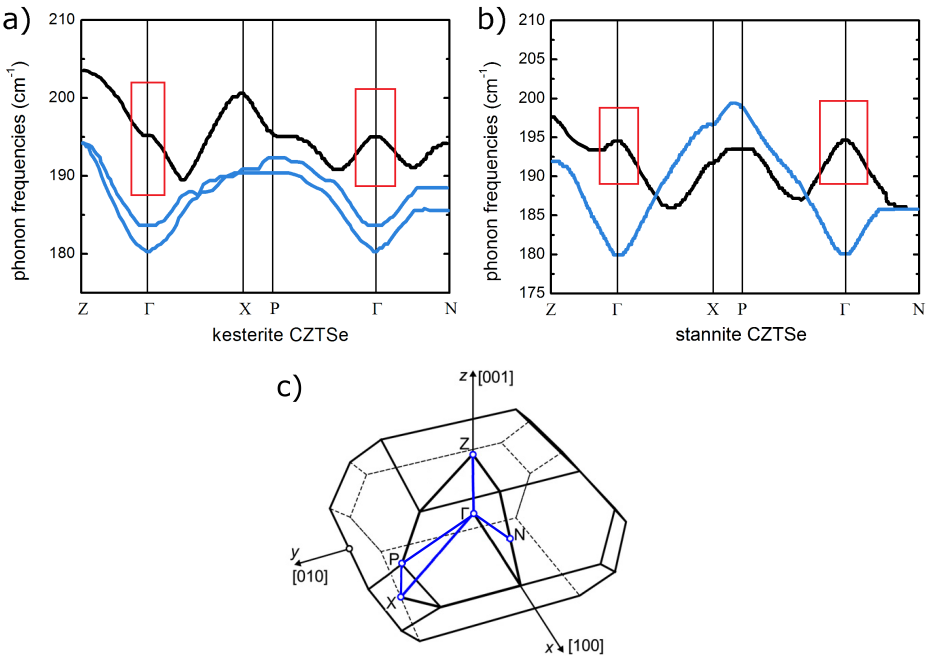

Figure 1.10: Phonon dispersion of the Raman active A modes of kesterite figure a) and stannite figure b) CZTSe calculated by DFT by Gürel et. al. (digitized from [41]). The main mode is plotted in black. The red rectangles highlight the phonon dispersion of the main modes around the Γ point. Figure c) depicts the first Brillouin zone of a body centered tetragonal lattice, the high symmetry points discussed in figures a and b are marked along with the direction in real space. The phonon is depicted for the blue paths. Figure c) is adapted from [42].

1.2.8 Raman in CZTSe literature

The zone center phonon energies have been calculated for kesterite and stannite CZTSe. The calculation results are summarized in this section in table 1.4 as calculated by DFT by Gürel et. al. [41], Amiri et. al. [48], and Khare et. al. [49].

The exact values of the calculated phonon energies differ considerably. For the kesterite structure Amiri et. al. [48] and Gürel et. al. [41] agree that the two A modes with the highest energy are separated by around 11 cm^{-1}. Khare et. al. [49] and Gürel et. al. [41] agree that the two lower energy A modes are separated by around 4 cm^{-1}. The two stannite A modes are separated by 15 cm^{-1} to 28 cm^{-1} depending on the reference.

Comparing kesterite and stannite one sees that no significant difference in the zone center phonon energies can be expected. There is no clear trend which of the polymorphs is expected to have higher or lower phonon energies.

	Kesterite references				Stannite references		
	[41]	[48]	[49]		[41]	[48]	[49]
A	196.2	203	213.1	A1	194.6	203	213.8
A	183.6	192	193	A1	180	175	184.5
A	181	178	188.1				
B (LO TO)	231.1 - 236.0	237	236.3 - 247	B1	220.2	232	205.4
	223.4 - 226.0	230	226.8 - 229.6		69.2	72	73.6
	202.5 - 211.3	216	193.2 - 199.3	B2 (LO TO)	233.0 - 240.3	254	248.0 - 255.4
	171.5 - 171.8	187	158.0 - 159.3		226.6 - 228.4	222	213.9 - 218.0
	85.4 - 85.6	88	93.3 - 93.6		161.9 - 162.5	180	151.1 - 152.3
	74.4 - 74.6	75	85.4 - 85.9		79.4 - 79.4	79	94.3 - 94.3
E (LO TO)	223.6 - 231.9	239	233.0 - 242.9	E (LO TO)	222.6 - 228.5	232	237.1 - 245.3
	217.4 - 219.9	224	221.5 - 236.4		211.6 - 213.4	226	199.0 - 205.2
	205.4 - 208.8	211	194.5 - 198.0		201.7 - 211.3	209	185.5 - 190.6
	159.0 - 159.1	174	147.8 - 148.3		163.1 - 163.3	180	155.4 - 155.8
	81.0 - 81.0	81	101.6 - 101.7		86.2 - 86.2	90	100.4 - 100.4
	60.6 - 64	64	80.7 - 80.75		59.9 - 59.6	60	80.8 - 80.9

Table 1.4: Summary of DFT calculated zone centre phonon energies for CZTSe (in cm^{-1}).

Also the the LO/TO splitting of the modes does not follow a trend. In fact, the phonon energies differences ($\Delta = TO - LO$) differ between calculations in absolute values and in trends as can be seen in table 1.5

The values given by Guc et. al. [50] are phonon energies elucidated by polarization orientation Raman measurements on single crystals.

The Raman mode energies vary significantly in both theoretical calculation and in the experimentally measured values. This can be seen in figure 1.11 depicting some normalized Raman spectra in the energy range between $140\,cm^{-1}$ and $280\,cm^{-1}$. These spectra are chosen since they represent the differences in the spectral shape of CZTSe Raman measurements.

	[50]	Δ	[41]	Δ	[51]	Δ	[49]	Δ
E	x	x	60.6-60.6	0	62.6-62.7	0.1	80.70-80.75	0.05
B	x	x	74.4-74.6	0.2	73.6-73.8	0.2	85.42-85.87	0.45
B	77	-	85.4-85.6	0.2	82.8-82.9	0.1	93.33-93.55	0.22
E	82	-	81-81	0	83-83.5	0.5	101.58-101.71	0.13
E	138	-	159-159.1	0.1	141.1-141.8	0.7	147.82-148.34	0.52
B	157	-	171.5-171.8	0.3	156.7-157.3	0.6	157.98-159.24	1.26
A	170		181		162.8		188.1	
A	174		183.6		166.5		193.01	
B	178	-	202.5-211.3	8.8	175.3-178.7	3.4	193.22-199.29	6.07
E	189	-	205.4-208.8	3.4	179-180.5	1.5	194.47-198.01	3.54
A	196		196.2		186.3		213.05	
E	224-231	7	217.4-219.9	2.5	199.8-202.8	3	225.50-226.37	0.87
B	235-239	4	223.4-226	2.6	204.2-205.4	1.2	226.81-229.55	2.74
B	245-250	5	231.1-236	4.9	227.1-228.8	1.7	236.30-246.97	10.67
E	x	x	223.6-231.9	8.3	222.8-226.2	3.4	233.02-242.85	9.83

Table 1.5: Zone center phonon frequencies (in cm^{-1}) for CZTSe measured by Guc et. al. [50] and calculated by Khare et. al. [51, 49] and Gürel et. al. [41]. The symmetry of the modes is indicated in the first column. 'Δ' indicates the energetic difference between the LO and TO values. 'x' symbolizes phonon modes that are not detected in the experiment and '-' is used for the modes where no splitting is detected.

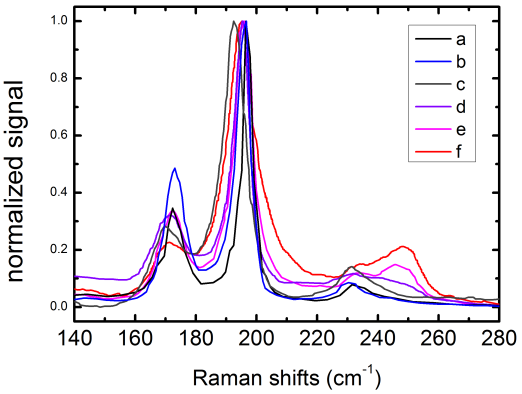

Figure 1.11: Normalized CZTSe Raman spectra. The spectra marked e to f are digitized from a: [52](sample prepared at 673 K); b: [53]; c: [54]; d: [52] (sample prepared at 723 K); e: [55](sample prepared at 450 °C) and f: [55] sample prepared at 550 °C).

In fact, the spectra differ in the relative intensity of all the modes and in their energy position. The variation of the main mode energy is easiest to see: it varies between 192 cm^{-1} and 198 cm^{-1}. For the other modes in the energy ranges (160-180) cm^{-1} and (220-260) cm^{-1} the exact energetic position of the modes can only be determined by fitting since two or more modes of low intensity can be present in those energy ranges as predicted by theory. This multi-mode behavior is clear in the (220-260) cm^{-1} energy range. For the (160-180) cm^{-1} energy range this behavior can best be seen in figure 1.12 where the spectrum by Uday et. al. [52] shows a clear shoulder at 170 cm^{-1}.

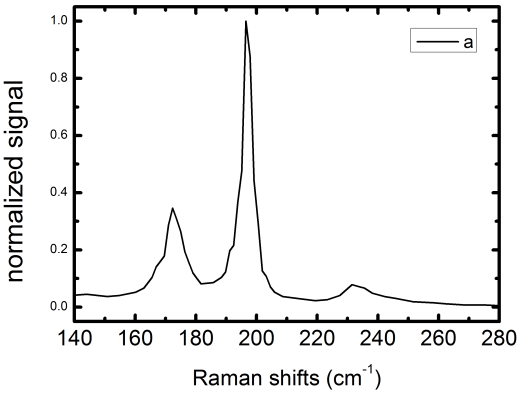

Figure 1.12: Normalized CZTSe Raman spectra digitized from [52] (sample prepared at 673 K). This is spectrum a from figure 1.11

1.3 Photoluminescence

Photoluminescence (PL) is the radiative recombination of thermalized electron hole pairs that were generated by the absorption of radiation. During a photoluminescence experiment a photon is absorbed, exciting electron hole pairs which lose energy till they get to the conduction and valence band extrema (electrons to the lowest available energy level in the conduction band, and holes to the highest available energy level in the valence band) where they can recombine. The light emitted by the recombination of electrons and holes is measured and spectrally resolved. The free carrier approximation leads to an expression for the emission intensity $I_{PL}(\omega)$ for an ideal semi conductor [25]:

$$I_{PL}(\omega) = \begin{cases} (\hbar\omega - E_G)^{1/2} \cdot \exp\left(\dfrac{-(\hbar\omega - E_G)}{k_B T}\right) & \text{for } \hbar\omega > E_G; \\ 0 & \text{else} \end{cases}$$

with E_G the band gap, k_B the Boltzmann constant, and T as the temperature. The root-like density of states of free charge carriers is reflected in the first part of the expression. The second part reflects the Boltzmann distribution function of electrons and holes.

This ideal photoluminescence shape discussed above is not used to fit the room temperature spectra measured on CZTSe in this work. For all measured samples a higher defect density is expected leading to a deviation from the ideal root-like behavior of direct semiconductors. A Gaussian shape is therefore used to fit the PL.

Intensity dependent photoluminescence

Room temperature photoluminescence (RT-PL) can be used to check for the presence of different phases with various band gaps in the absorber. The RT-PL measurements show the luminescent recombination involving either only the bands, or the band and the deep defects [56]. When the sample is at room temperature, PL is not expected from shallow defects and excitons. Shallow defects do not cause luminescent transitions since they are thermally emptied at room temperature. Further, excitonic bonds are very unlikely to be stable as they are usually weaker [57] than the thermal energy. Monitoring the evolution of the PL signal intensity with the excitation laser intensity (P) hints at the nature of the examined transition. The PL signal intensity for a given energy is proportional to the PL yield (Y_{PL}):.

$$Y_{PL}(P) = P^k; \tag{1.15}$$

where k is a characteristic parameter for the transition permitting the differentiation between transitions of different types. Y_{PL} is proportional to the density of involved charge carriers:

$$Y_{PL} \propto n \cdot p;$$

where n is the density of electrons and p the density of holes, which are not necessarily the free ones.

In our measurement conditions we have to consider the high injection case where the number of charge carriers in thermal equilibrium is negligible compared to the injected charge carriers (see section 2.1)

In the case of high injection, band to band transitions have a k of 2 as electron and hole densities n and p are each proportional to the excitation intensity.

For defect related transitions, one charge carrier is limited by the defect density which leads to $k = 1$. These k values are diminished by competing non luminescent recombination paths which results in $k < 1$ for defect-band transitions and $k < 2$ for band-band transitions (see chapters 7 in [56], and in [58] or the publication by Schmidt et. al. [59]).

This lowering of k due to non luminescent recombinations of electrons and holes leads to the fact that only a $k > 1$ leads to a definitive assignment to band to band recombinations while a $k < 1$ only hints at a defect-related recombination.

1.4 Secondary phases

The last section discussed how CZTSe can grow in a multitude of polymorphs. The growth of CZTSe can also result in many undesired secondary phases. The coexistence of different materials in the solar cell absorber is probable in CZTSe since it has a small existence region as discussed by Dudchak et. al. [10]. The secondary phases that can be expected along with their structural and opto-electronic properties are summarized here.

1.4.1 Phase diagram

The phase content of a sample can be predicted by plotting its composition in the ternary phase diagram assuming thermal equilibrium. The phase diagram usually shown in CZTSe literature is adapted from the one proposed by Dudchak et. al. [10]. This quasi-ternary phase diagram is a 2D plot representing the isothermal section of the Cu_2Se-ZnSe-$SnSe_2$ system assuming a sufficient Se partial pressure [60, 10]. This phase diagram thus does not discuss the phases that only differ by their Se content like SnSe/$SnSe_2$ and Cu_2SnSe_3/Cu_2SnSe_4.

Figure 1.13 depicts the isothermal (at 670 K) quasi-ternary phase diagram proposed by Dudchak and Piskach [10]. Five pure phase regions are discernable: pure CZTSe (labeled 1 and marked blue), the Cu_2SnSe_3 region and the $SnSe_2$, ZnSe, and Cu_2Se regions at the corners of the phase diagram.

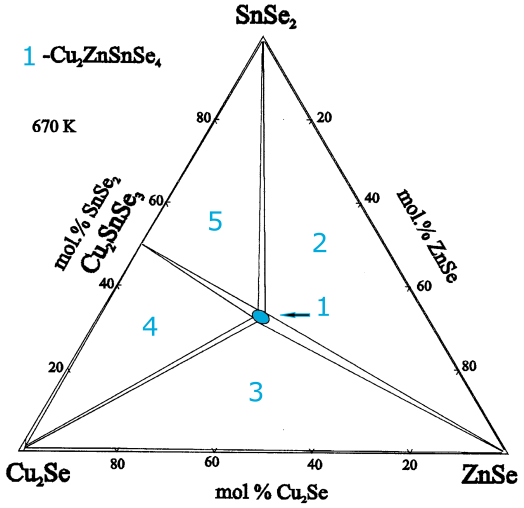

Figure 1.13: Quasi-ternary phase digram from [10] representing the 670 K isothermal section of the Cu_2Se-ZnSe-$SnSe_2$ system.

It further shows eight two-phase regions represented by the tie-lines connecting the phase pure regions. Finally four three-phase regions (labeled 2-5 in figure 1.13) are represented by a triangular range of compositions.

Each triphasic region is composed of the phases present at the corners of the triphasic regions. For example a sample of a composition in region 2 would be composed of ZnSe, $SnSe_2$, and CZTSe.

1.4.2 Properties of secondary phases

The properties of the secondary phases of CZTSe that are treated in the next chapters are summarized in this section (if reported in literature).

Copper-tin-selenide

Most publications find that the ternary Cu_2SnSe_3 crystallizes in the monoclinic structure [61, 62, 63, 64, 65], while only Babu et. al. [66] and Skoug et. al. [64] find a cubic sphalerite structure. Also Rivet [67] found an orthorhombic phase. Marcano et. al. [68] prepared a selenium richer compound i. e. Cu_2SnSe_4. The Cu_xSnSe_y ternaries are referred to as CTSe.

Orthorhombic Cu_2SnSe_3

An orthorhombic ordering was found at low temperature growth (<450 °C) by Rivet [67] with lattice parameters $a = 4.03\,\mathring{A}$, $b = 5.7\,$Å, $c = 12.08\,$Å. No Raman fingerprints or band gap measurements were found for this structure.

Sphalerite Cu_2SnSe_3

The calculated lattice parameter for the sphalerite structure Cu_2SnSe_3 is $a = 5.73\,$Å [66], which is in agreement with the d spacing measured by Skoug et. al. [64]. No Raman fingerprints or band gap measurements were found for this structure.

Cubic Cu_2SnSe_4

Marcano et. al. [68] prepared Cu_2SnSe_4 crystals of cubic structure with space group $F\bar{4}3m$ (T_d^2; No. 216). Their measured lattice parameter of the cubic Cu_2SnSe_4 is $a = 5.6846(3)\,$Å, which is in accordance with the results of Li et. al. [69]. Zainal et. al. measured a direct band gap of 1.2 eV [70]. The Cu_2SnSe_4 should rather be denoted $Cu_2Sn\square\ Se_4$ where the $\square$ is the cation vacancy needed to maintain the same number of cation and anion sites [68]. No Raman fingerprints were found for this structure.

Monoclinic Cu_2SnSe_3

The monoclinic structure with space group Cc (C_s^4; No. 9) is the most studied CTSe ternary. The structure was confirmed by powder X-ray diffraction measurements (XRD). The unit cell parameters are $a = 6.9670(3)$ Å, $b = 12.0493(7)$ Å, $c = 6.9453(3)$ Å, and $\beta = 109.19(1)°$ [63]. Optical absorption measurements have shown that monoclinic Cu_2SnSe_3 has a direct band gap of $E_G = 0.84$ eV at room temperature [62].

First reference Raman spectra of Cu_2SnSe_3 were measured by Altosaar et. al. [53]. Marcano et. al. [61] provided more detailed Raman measurements assigning some of the found Raman modes to their symmetry through comparison with lattice dynamical calculations. The measured Raman spectrum is shown in figure 1.14. The main mode is at 178 cm^{-1} followed by lower intensity modes at (83, 204, 231, 244, 291, 263) cm^{-1}.

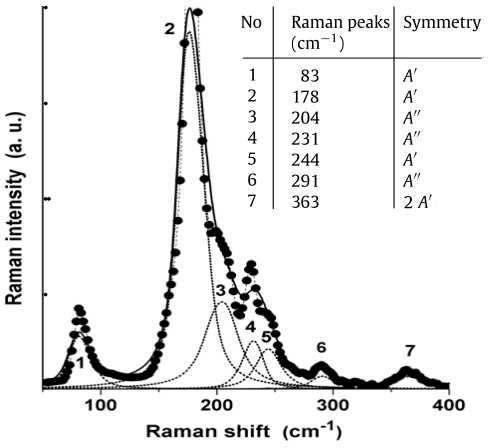

No	Raman peaks (cm^{-1})	Symmetry
1	83	A'
2	178	A'
3	204	A''
4	231	A''
5	244	A'
6	291	A''
7	363	2 A'

Figure 1.14: Raman spectrum measured on a Cu_2SnSe_3 crystal. The dashed line marks single peaks. The full line depicts the sum of fits. The insets shows the peak positions and their symmetry assignment. Taken from Marcano et. al. [61]

Zinc-selenide

Zinc-selenide (ZnSe) is a secondary phase that can occur during the growth of CZTSe. ZnSe forms in the cubic zincblende structure, with a lattice parameter of $a = 5.669$Å(ICDD database PDF No. 00-037-1463).

Khan et. al. [71] measured the band gap of ZnSe at room temperature by transmission at 2.76 eV, by photoluminescence at 2.74 eV, and by ellipsometry at 2.82 eV.

Arslan et. al. further showed that the incorporation of copper in the ZnSe, lowers its band gap down to 2.36 eV for 20 % copper incorporation in the ZnSe layers[72].

Copper and oxygen related defect luminescences on ZnSe were observed by cathodoluminescence at room temperature by Morozova et. al. [73]. Two

defect related luminescences were found at 640 nm (1.94 eV), and at 740 nm (1.67 eV).

The vibrational properties of ZnSe are studied in the publication of Irwin and LaCombe [74]. The factor group analysis of ZnSe in the zincblende structure space group $F\bar{4}3m(\mathrm{T}_d^2$; No. 216) gives one triply degenerated T_2 Raman active mode which is split due to the polarization of the crystal into LO-TO split modes [74]. The TO split mode is at 206 cm^{-1} and the LO split T mode is at 251 cm^{-1}.

The Raman tensors of the T_2 modes needed in this thesis are listed here [32, 28, 29]:

$$T_{2,x} = \begin{pmatrix} 0 & 0 & 0 \\ 0 & 0 & d \\ 0 & d & 0 \end{pmatrix};\ T_{2,y} = \begin{pmatrix} 0 & 0 & d \\ 0 & 0 & 0 \\ d & 0 & 0 \end{pmatrix};\ T_{2,z} = \begin{pmatrix} 0 & d & 0 \\ d & 0 & 0 \\ 0 & 0 & 0 \end{pmatrix}; \tag{1.16}$$

Tin-selenide

Tin-selenide (SnSe), a further possible secondary phase, grows in the orthorhombic crystal structure space group $Pnma$ (D_{2h}^{16}; No. 62) with lattice parameters $a = 4.44\,\text{Å},\ b = 11.498\,\text{Å},\ c = 4.153\,\text{Å}$(according to the ICDD database PDF No. 00-048-1224).

Lefebvre et. al. [75] calculated the band structure of SnSe using DFT and found a direct band gap at 1.3 eV and an indirect one at 0.9 eV. These predictions are confirmed by Soliman et. al [76].

The factor group analysis of this space group gives 21 optical modes of which 12 are Raman active: $3A_g + 2B_{1g} + 4B_{2g} + 2B_{3g}$. The publication by Chandrasekhar et al. [77] resolves the vibrational spectrum of SnSe as summarized in figure 1.15. The Raman modes visible in the energy range measurable by our setup are at 108 cm^{-1} (B_{3g}), 130/133 cm^{-1}($\mathrm{A}_g/\mathrm{B}_{1g}$), and 151 cm^{-1} (A_g).

Tin-diselenide

Tin-diselenide ($SnSe_2$) crystallizes in the trigonal $P\bar{3}m1(D_{3d}^3$; No. 164) leading to two Raman active modes, namely an A_{1g} symmetry mode and an E_g symmetry mode. The lattice parameters of the trigonal $SnSe_2$ are: $a = b = 3.811\,\text{Å},\ c = 6.137\,\text{Å}$(according to the ICDD database PDF No. 01-089-2939).

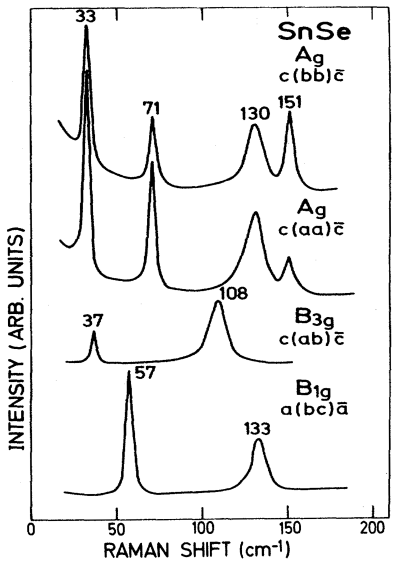

Figure 1.15: Room temperature Raman measurements of SnSe measured under different polarization configurations. Taken from [77].

Mead and Irvin [78] measured the Raman modes of $SnSe_2$ and their symmetries as summarized in figure 1.16. The polarization dependent measurement shows an A_{1g} mode at 185.5 cm^{-1} and an E_g mode at 116 cm^{-1}.

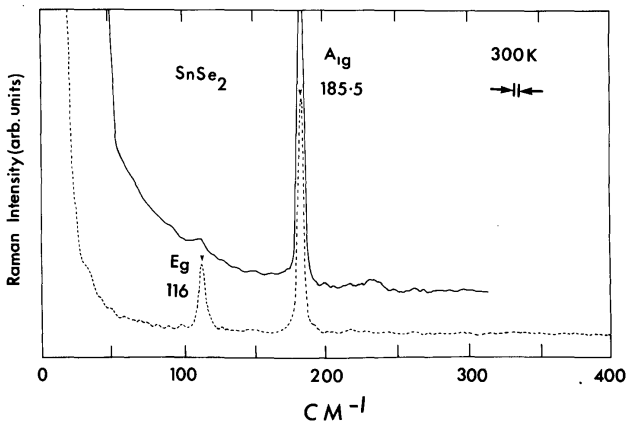

Figure 1.16: Room temperature Raman measurements of $SnSe_2$ (488 nm excitation) measured in different polarization configurations. Taken from [78].

There is no clear agreement on the band gap of $SnSe_2$. It is reported to be between 1 and 1.6 eV depending on the publication. The most convincing reports are from Chung et. al. [79] who measure two phases: an amorphous $SnSe_2$ with a 1.52 eV band gap and a crystalline phase with a 1.33 eV band gap. Another convincing report is from Bindu et. al. [80] who measure a band gap between 1-1.27 eV.

Chapter 2

Experimental

2.1 Experimental setup

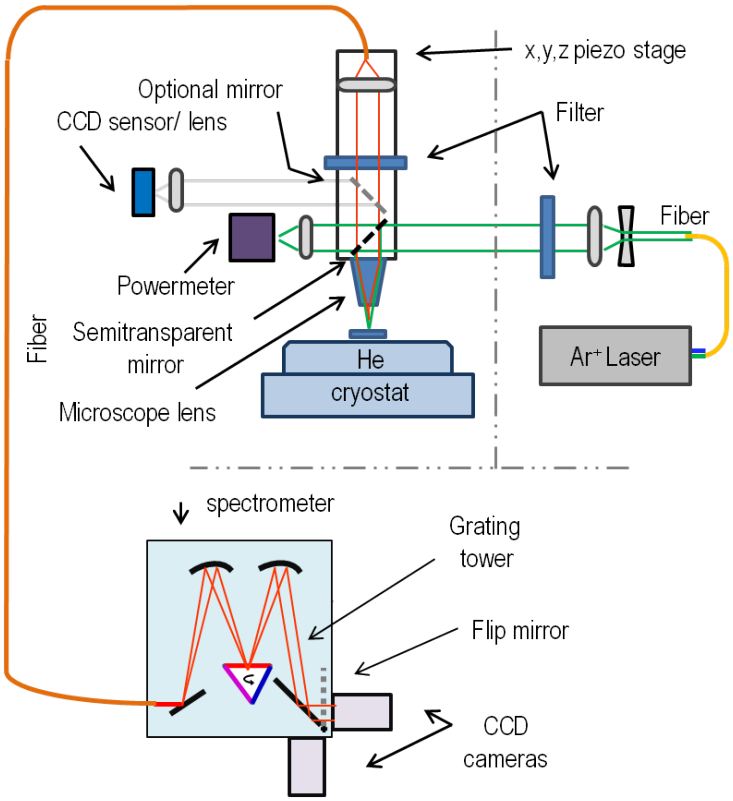

Figure 2.1: Schematic representation of the μPL/μRaman setup. The dashed lines represent movable parts. The dashed-dotted lines divide the setup into three parts: the laser, the microscope and the spectrometer.

The PL and Raman measurements presented in this thesis, unless stated differently, are made on a home built setup schematized in figure 2.1. The setup is composed of the following elements: a laser for the excitation, a fiber to connect the laser to the μPL/μRaman microscope, a lens system to enlarge the laser beam, filters to clean the laser, a semi-transparent mirror, a microscope lens for focusing, a helium cryostat, filters to remove the laser line, a lens to focus the emitted radiation into a fiber connecting the microscope with a spectrometer, a powermeter and a CCD sensor.

The setup was built by Jes Larsen and Levent Gütay. Updates to the setup were added during this thesis permitting Raman measurements, a more precise monitoring of the laser power, the usage of further excitation wavelengths, and giving the possibility to simultaneously image the surface of the sample and the measured laser spot in a light microscope.

The experimental setup can be divided into three parts: the excitation source (the laser), the microscope and the spectral acquisition (the spectrometer). The excitation is made using the 514.5 nm and 457.9 nm lines of an Ar ion laser. Besides these lines unwanted plasma lines are generated. These unwanted lines are filtered out by the fiber connecting the laser to the μPL/μRaman setup (not shown in figure 2.1) and a set of filters that cut out the remaining lines and whatever might be generated in the fiber. The plasma lines emitted very close to the laser line are removed by a line filter.

The laser light spot is enlarged using a lens system in order to fully illuminate the microscope lens used to focus the laser on the sample. This needs to be done since the diameter of the focal cylinder d depends on the diameter of the laser beam[1] D, the wavelength of the light λ and f the focal length of the lens (see figure 2.2) [81]. d is given by:

$$d = \frac{4\lambda f}{\pi D}$$

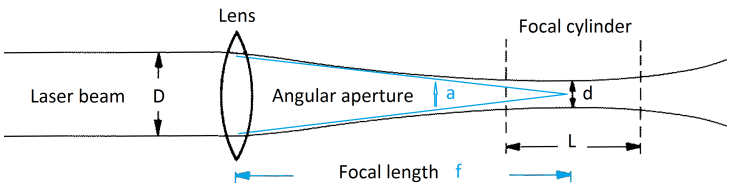

Figure 2.2: Schematic representation of laser beam focusing. Adapted from [81].

[1]The diameter of the laser beam is limited by the lens diameter.

The second part of the setup is the light collection and spectral analysis. The setup is a confocal one so the collection optics are the same optics used for excitation. One half of the emitted radiation collected by the microscope lens is transmitted through the semi transparent mirror. The laser light reflected or back-scattered from the sample is filtered out using either a color filter (PL) or an edge filter (Raman) before it is focused into a fiber transmitting it into the spectrometer used for spectral analysis. The diameter of this fiber is important since it serves as the entrance slit to the spectrometer defining the resolution of the measurement. It is chosen as a compromise between signal strength and resolution. A resolution (defined by the measured full width at half max of the laser line) of $3.2\,\mathrm{cm}^{-1}$ is achieved by a $50\,\mu$m fiber[2]. Doubling the diameter of the fiber leads to a fourfold signal increase but also lowers the resolution since the effective entrance slit is bigger.

To be able to perform Raman measurements, the spectrometer was updated with a 2400 lines grating resolving a narrow energy range (Raman shifts are in the order of $200\,\mathrm{cm}^{-1}$ corresponding to $\approx 6\,$nm for 514.5 nm excitation laser wavelength). The spectrometer is equipped with two CCD cameras so that the whole UV-IR range (400 nm to 1600 nm) can be measured.

Two updates to the setup were made, a CCD camera and a powermeter are added behind the semi transparent mirror. The CCD camera is a webcam modified with a matching lens that can be used along with a mirror to finish an alternative microscope enabling to look at both the sample and the excitation laser. This extra feature means the same area measured by other techniques can be identified. The excitation power on the sample is not linearly dependent of the power output set on the laser. Therefore the actual laser power at the sample is measured behind the semitransparent mirror. The linearity of the power dependence of the latter configuration is checked over several orders of magnitude with a constant proportionality factor of ≈ 1.

The usually used laser powers range between 0.01 mW and 4 mW. It is important to know the laser power as it is, for example, needed for the estimation of the injected charge carriers during a PL experiment. The injected charge carrier densities are estimated to be $4{\cdot}10^{17}/\mathrm{cm}^{-3}$ for the lowest used excitation intensities of about 0.01 mW, assuming 500 nm penetration depth, and 10 ns carrier lifetime. This is consistent with the high injection mode since the doping densities for working solar cells are estimated to be less than $5{\cdot}10^{16}/\mathrm{cm}^{-3}$.

[2]The same FWHM was found by measuring the narrow lines of sulphur reported at $214.4\,\mathrm{cm}^{-1}$ and $218\,\mathrm{cm}^{-1}$ in literature. The two lines were observed separately with an individual FWHM of $3.2\,\mathrm{cm}^{-1}$.

The polarized macro Raman measurements shown in section 4.4 were measured at the University of Barcelona by Xavier Fontané, Victor Izquierdo-Roca and Alejandro Pérez-Rodríguez on a T64000 Horiba Jobin-Yvon spectrometer with an excitation wavelength of 514.5 nm. A spot size of 100 μm was chosen to ensure the excitation of a high number of randomly orientated micro-crystalline grains. In order to minimize the presence of thermal effects in the spectra, the excitation power on the sample surface was kept below 10 mW.

The P/O-Raman measurements were performed on epitaxial samples by Levent Gütay and Christiane Stroth at the University of Oldenburg on a Horiba Jobin Yvon Labram Aramis confocal Raman microscope. The spot diameter of the Nd:YAG laser excitation (532 nm) was estimated to be around 2 μm. The spectra were taken at an excitation power of 8 mW which is below the critical power threshold which would have an impact on the probed sample. The sample was mounted on a rotating table which allows the measurement of the same sample position at various azimuth angles. A narrow laser beam (D = 1-2 mm) was focused on the sample ensuring that the angular aperture is as small as possible i. e. that the laser beam is as parallel as possible. The angular aperture a is given by (see figure 2.2):

$$a = 2 \arctan\left(\frac{D}{2f}\right)$$

which results in an angular aperture a of around 16° for an estimated laser beam diameter $D \approx 1\,mm$ focused by a microscope lens of focal length $f = 3.6\,mm$.

2.2 Sample growth methods

This section discusses the methods used to grow the CZTSe samples. The samples were prepared by other members of the group therefore the discussion of the sample preparation will be limited to the information needed for further discussion.

2.2.1 Electrodeposition and annealing

The 'electro-deposited' samples are made by electro-depositing metallic precursor layers which are then annealed in Se and SnSe atmosphere. The samples discussed here were made by Alexandre Crossay. The precursors were prepared by sequential potentiostatic electro-deposition of zinc on tin on copper onto $2.5 \times 2.5\,cm^2$ molybdenum coated glass substrates (Zn/Sn/Cu/Mo)[82]. The deposition is done using a three electrode setup with a platinum counter electrode, a reference electrode (saturated $Hg|Hg_2Cl_2$ for Cu deposition and Ag|AgCl for Sn and Zn) and a rotating disk electrode with a Mo substrate as a working electrode. The setup is schematized in figure 2.3.

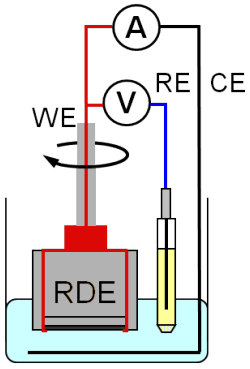

Figure 2.3: Schematic representation of the three electrode electrodeposition setup.
RE: reference electrode,
CE: counter electrode,
WE: working electrode,
RDE: rotating disc electrode.
Courtesy of:
Monika Arasimowicz

The potentials used for the deposition are measured relatively to different reference electrodes. The potentials measured were -1.07 V for copper (vs saturated $Hg|Hg_2Cl_2$), -0.75 V for tin (vs Ag|AgCl) and -1.15 V for zinc (vs Ag|AgCl). The aqueous electroplating solutions contained 0.1 M $CuSO_4$ for the deposition of copper, 50 mM Sn(II) methanesulfonate for the deposition of tin and 50 mM $ZnCl_2$ for the deposition of zinc.

The finished absorber of the sample discussed in the section 3.3 has a conversion efficiency of 2.1%. The method has so far led to conversion efficiencies of up to 5.6 %.

The electro-deposited metal stack precursors are annealed in a tube furnace with Se and SnSe as detailed in section 2.2.3.

2.2.2 Epitaxy on GaAs (100)

The samples are grown by the simultaneous evaporation of all elements onto single crystalline GaAs wafers as substrates. These samples were produced by Alex Redinger in a Molecular Beam Epitaxy (MBE) machine. The MBE is schematized in figure 2.4. It is equipped with Cu, Zn, Sn, SnSe and a Se sources. The Se is further equipped with a valved cracker. The base pressure is about $1.3{\cdot}10^{-8}$ mbar and the growth pressure does not exceed $4{\cdot}10^{-8}$ mbar. The substrates used are p-doped GaAs substrate in the (100) orientation. The doping is a Zn doping in the order of $10^{19}\,\mathrm{cm}^{-3}$ which ensures a high thermal and electric conductivity of the substrate. A pyrometer is used to measure the temperature.

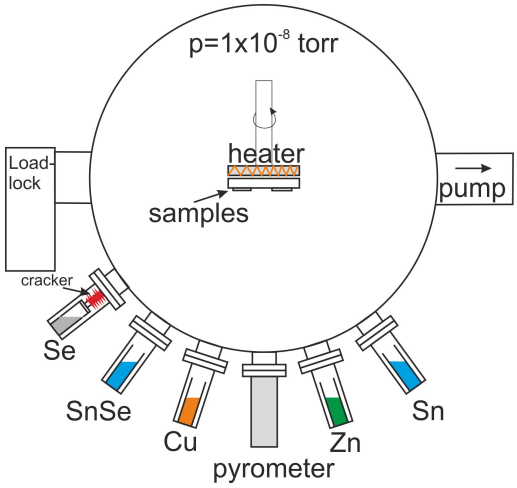

Figure 2.4: Schematic drawing of MBE system. Courtesy of Alex Redinger.

To prevent the decomposition of CZTSe at high temperatures shown in [83], not only a Sn source but also an additional SnSe source is used in order to increase the Sn and Se supersaturation at the sample. SnSe and Se are materials with a high vapor pressure preventing the decomposition reaction as shown by [84]. To increase the chalcogen reactivity, the Se cracker nozzle is heated to 1000 °C so that the Se vapor almost entirely consists of Se_2 instead of Se_n rings (n=2-8). The growth temperature, i. e. heater temperature, is about 450 °C. The process used is schematically shown in figure 2.5. It is a three stage process: the first stage is the growth stage with all sources open. The second stage is an annealing stage where the Sn, Se and SnSe sources are left open to prevent the CZTSe decomposition and during the last stage the sample is cooled down in a Se environment.

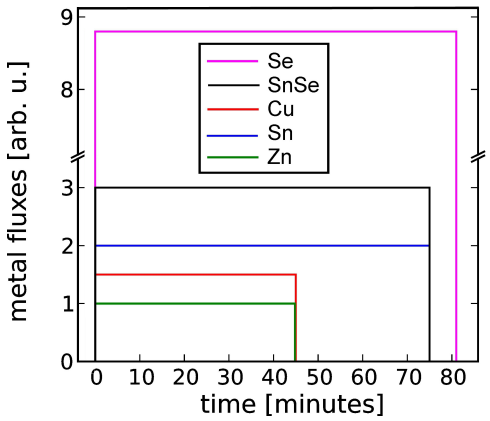

Figure 2.5: Schematic growth sequence representing the times where the sources are open. Courtesy of Alex Redinger.

2.2.3 Physical vapour deposition on Mo/glass

The sample growth here is very similar to the one discussed in the previous section. The same MBE machine is used as described in the previous section to grow poly-crystalline CZTSe. The main differences to the CZTSe growth described in the previous section are that the absorber is annealed after deposition in an oven and that the CZTSe is grown on Mo coated glass. The samples were prepared by Alex Redinger and Marina Mousel. The CZTSe is made by the simultaneous deposition of all elements (Cu, Zn, Sn and Se) at 320 °C. The Se valve is kept open during the cool-down to prevent Se losses. The precursors are then annealed in a graphite box at 500 °C for 30 min in the presence of 1 mbar H_2/N_2. To prevent the CZTSe decomposition [83] mentioned in the previous section, SnSe and Se are added in the annealing box.

For the samples discussed in the next sections, two different methods are used to provide the Se and SnSe supersaturation needed at the CZTSe surface to prevent decomposition [84]. These two preparation methods are schematized in figure 2.6. The first method adds a capping layer of $SnSe_2$ on the precursor by leaving both the Sn and Se sources open during the precursor cool-down. Only 20 mg of Se powder is introduced into the annealing box. The advantage of this preparation method is that the absorber growth is simplified since it eliminates the need to control the SnSe partial pressure during the heat treatment. The SnSe capping layer evaporated on the precursor protects the absorber during the transfer from the vacuum chamber to the annealing chamber and acts as a source of SnSe during the annealing. This CZTSe preparation method is used to produce the sample discussed in

section 3.2.

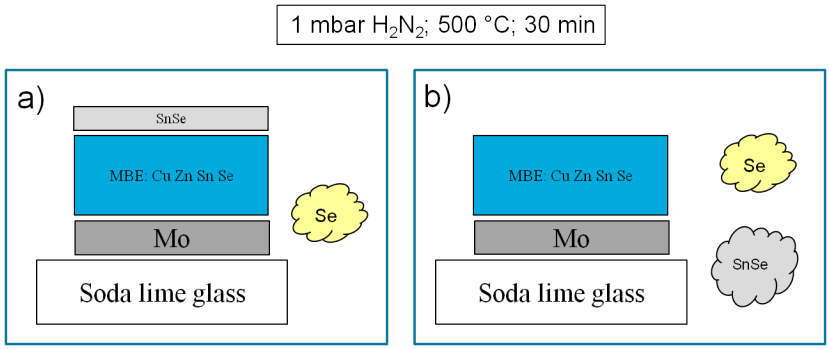

Figure 2.6: Scheme comparing CZTSe precursor annealing, with two different methods for the delivery of SnSe in the graphite box. Sub-figure a) shows the preparation method with the SnSe/$SnSe_2$ capping layer. Sub-figure b) shows the preparation method using the addition of SnSe powder.

The second possibility to provide the necessary Se and SnSe vapor pressures is to add both elements in powder form into the annealing box. The sample discussed in section 3.3 is made this way. The precursor is grown copper rich ($Cu/(Zn + Sn) > 1$) as opposed to the commonly used copper poor precursors.This precursor is etched in potassium cyanide (KCN) prior to annealing to eliminate a copper selenide layer that forms during the precursor deposition process. The Cu_xSe_y is removed to prevent the formation of a detrimental Cu-Sn-Se phase during the annealing. The final absorber is then copper poor and zinc rich. This process produced CZTSe solar cells with efficiencies of up to 7.5 %. Further details of this process can be found in the publication by Mousel et. al. [85].

2.3 SIMS calibration

Secondary ion mass spectrometry (SIMS) is a useful characterization method to gain the non-quantitative elemental composition as a function of depth. Calibrating this data results in the depth dependent composition. The calibration can be done with a known elemental composition. In this thesis the composition given by energy-dispersive X-ray spectroscopy (EDX) is used. However, the composition from EDX assumes a homogeneous distribution of the elements in the sampled volume. An in-homogeneous elemental distribution would lead to preferential absorption of the electron beam and would therefore lead to a wrong composition. This has to be borne in mind when

using EDX to calibrate SIMS measurements i. e. ideally the SIMS signal of all elements should be constant within the depth where the EDX composition is measured.

The depth at which the X-rays used for EDX composition originate depends on the atomic elements investigated and the experimental conditions used. The electron beam acceleration energy is diminished by the investigated material until it cannot be absorbed by the characteristic core shell energy level investigated for each of the elements considered. For the calibration, the SIMS signal is normalized to 1 at a chosen depth. The composition is then multiplied into the normalized SIMS signal to calculate the metal ratios (Zn/Sn) and Cu/(Zn+Sn)). These compositions can then be plotted in a ternary diagram.

The dependence of the transmitted X-ray intensity as a function of the depth can be simulated using Monte Carlo simulation for example [86]. An example of a normalized X-ray profile generated by 20 kV accelerated electrons from K-lines of Cu, Zn and Se, and the L-line of Sn is shown in figure 2.7. This can be used to calibrate SIMS signals that vary strongly in the depths from which the X-rays(used for composition measurements) are generated. It is then used as a weight function for the SIMS signal prior to normalization.

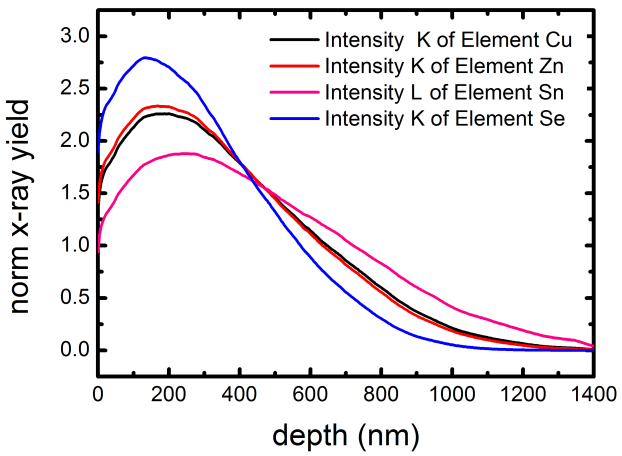

Figure 2.7: Normalized generated X-ray intensity as a function of the EDX measurements generation depth i. e. for 20 keV electron-energy generated from the K-lines Cu, zn and Se and the L-line of Sn.

2.4 Sample preparation for depth dependent measurements

Raman and photoluminescence (PL) were measured at different depths in the solar cell absorber. For these measurements the samples were prepared by two different methods. This is important since one wants to correlate the Raman and PL fingerprints to sample parameters like the elemental composition and/or the parameters of the resulting solar cell. This correlation was impossible to achieve by comparing different samples due to two main problems. First, the sampling depth of Raman, PL and the used composition measurements differ considerably. Second, the surface of the samples is quite random for the same composition and preparation conditions.

The first preparation technique for different depths is the sequential etching of the sample. The destructive aspect of this technique is diminished by cutting the sample into different pieces etched for the different lengths of time.

The second preparation method is the sequential thinning of the layer by sputtering craters of different depths. The sputter damaged layer is then removed by a short etching (15 s). All etchings were done in 0.02 M Br_2 methanol solutions (as can be seen in figure 2.8).

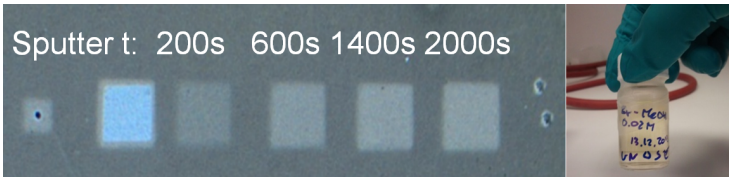

Figure 2.8: Microscope image of sputtered pits and photograph of the etch solution.

Chapter 3

Secondary phases discrimination

Ideally one would want single phase $Cu_2ZnSnSe_4$(CZTSe) samples for material characterization and solar cell optimization. Due to a small existence region (i. e. a small compositional range resulting in single phase CZTSe), it is likely one would obtain one or more secondary phases as a by-product of the material growth [10]. It is therefore important to have characterization techniques able to discriminate the secondary phases ideally even when they are present in low amounts.

The growth conditions of the samples discussed in the following sections, are optimized for the highest solar cell efficiency, which means that the characteristic fingerprints of the secondary phases can be small compared to those of CZTSe. The analysis of these samples therefore provides a test if the other phase's signals can be accessed with the available techniques.

This chapter deals with the detection of the secondary phases that are likely to grow during $Cu_2ZnSnSe_4$ (CZTSe) solar cell absorber preparation. The possible secondary phases that are found during this thesis are discussed. The phases are Cu_2SnSe_3, SnSe, $SnSe_2$ and ZnSe. The discrimination of the different secondary phases by the experimental methods available in our lab (mainly Raman spectroscopy and photoluminescence) is discussed. Copper selenides, another possible secondary phase, was never detected during this project. It is therefore not discussed.

Adapted phase diagram

The quasi-ternary phase diagram proposed by Dudschak and Piskach [10] shows the experimentally determined phase relations between $SnSe_2$, Cu_2Se and ZnSe. This traditional representation expresses the composition as the relative percentages of the latter phase in the samples before heat treatment

However, under equilibrium conditions, the full conversion of all elements in the deposited layer occurs by formation of the most thermodynamically stable phases. These three compounds never coexist since they react to form CZTSe and/or CTSe depending on the original elemental composition. Therefore, in order to rationalize the percentages of the original phases at equilibrium for a sample of known elemental composition, the lever rule [87] is explicitly applied to all the phases in the diagram. The result of this process is plotted in figure 3.1. Each sub-triangle is treated as an independent pseudo-ternary phase diagram, where the lever rule is applied to the compounds at each corner giving the relative phases content present in the sample (*phase composition*) for a given elemental composition. The lever rule assumes that all original phases on the pseudo ternary phase diagram react to form the most complex phase (in this case CZTSe) in a triphasic region only limited by the original phase of lowest content.

The figure 3.1 pictures thick lines for the tie lines and thin lines for lines of constant phase content for the phase represented in the according color (different colors are chosen for the different phases).

The example of the composition described by a purple circle in figure 3.1 is discussed in the following. This composition is in the triphasic region $SnSe_2$-CZTSe-ZnSe therefore these three phases are expected to be present in such a sample. This composition lies on the intersection of the lines of constant 0.25 ZnSe, 0.25 $SnSe_2$ and 0.5 CZTSe phase content.

It should be noted that this plot of the phase diagram with phase composition proposed in figure 3.1 neglects both the size of the single phase CZTSe region and the width of the two phase regions connecting the quaternary phase to the binaries and ternary according to [10].

This proposed alternative plot is used throughout the rest of the thesis.

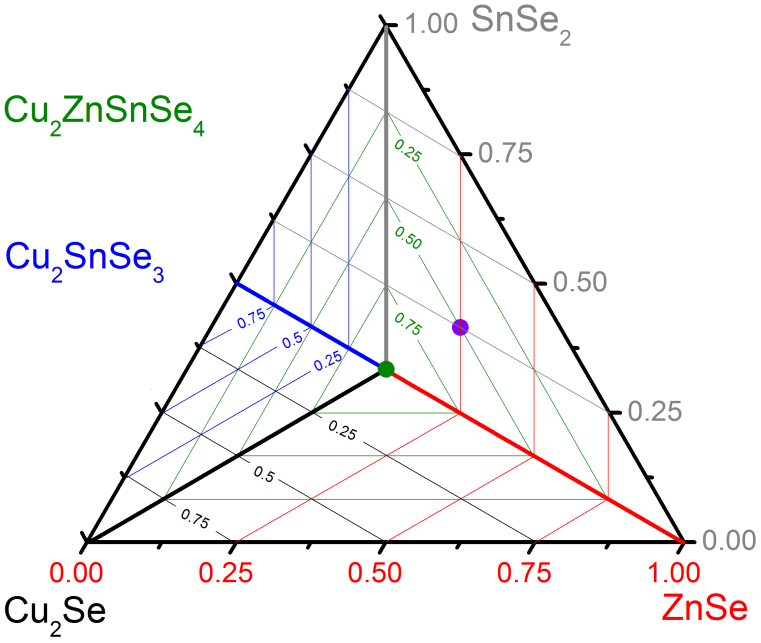

Figure 3.1: Phase diagram adapted from Dudschak [10] showing possible secondary phases in pseudo ternary phase diagram of CZTSe color coded: green for CZTSe, gray for $SnSe_2$, blue for Cu_2SnSe_3, red for ZnSe and black for Cu_2Se. By applying the lever rule [87] the relative atomic content of the phases in each three-phase region can be determined. The lines of constant phase content are plotted in the above defined color code for the phases proposed by Dudchak. The purple dot shows an exemplary Zn-rich Cu-poor sample composition. The green dot marks the composition of stoichiometric $Cu_2ZnSnSe_4$.

3.1 Copper-tin-selenides

The discrimination of a copper-tin-selenide (CTSe[1]) phase in a CTSe-CZTSe mix is described in this section. This is studied on Cu-rich and Sn-rich samples grown in the MBE on GaAs wafers. Raman spectra are compared with the relative content of the phases at different depths in order to assign the contributions in the spectra to CTSe and CZTSe.

As already mentioned in the background chapter 1.4.2 several CTSe polymorphs are possible but only one characteristic Raman spectrum is available therefore the last part of the section discusses which of these CTSe phases presence is probable in the sample.

The sample preparation is described in section 2.2.2 and was conducted by Alex Redinger. The SIMS measurements were done by Natalie Vallé. The data shown is partly published in [88].

Figure 3.2 depicts the cross section SEM micrograph of the sample under consideration. The graph shows a smooth, densely-grown deposit on the GaAs substrate. This SEM image is typical for epitaxially-grown layers since it does not show well separated grains that could be observed in cross section views of polycrystalline grown films.

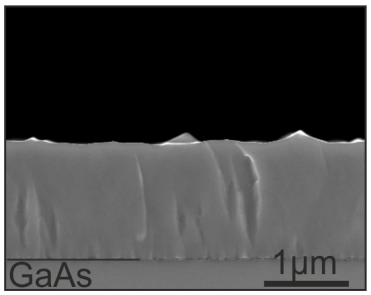

Figure 3.2: Cross section SEM micrograph of MBE deposited CZTSe on GaAs (001) surface. The black line marks the interface between deposit and GaAs.

The overall composition of the sample measured by 20 keV EDX is Sn-rich Cu-rich (Cu 24.7 at. %; Zn 7.8 at. %; Se 45 at. %; Sn 13.4 at. %, Ga 6.2 at. %; As 2.8 at. %). This composition plotted in the phase diagram puts the sample in the CZTSe-$SnSe_2$-CTSe triphase region. This is depicted as a black square in figure 3.4. The possible phases besides CZTSe are CTSe and $SnSe_2$. In order to gain a better idea a more detailed composition needs to be measured.

SIMS measurements on the discussed sample are calibrated to obtain the depth-dependent composition that can be plotted in the phase diagram (as introduced in 2.3).

The SIMS measurement results are depicted in figure 3.3 showing that, except for the first third of the sample sputter depth (0 s-2000 s), the ele-

[1] All copper-tin-selenide phases (discussed in section 1.4.2) are referred to as CTSe.

mental composition is nearly constant. The Cu signal is maximal at the top of the sample (surface) and the Zn content increases strongly with growing distance from the surface of the sample.

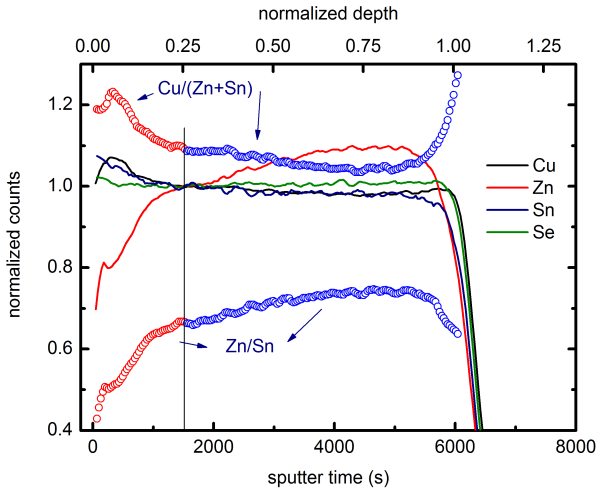

Figure 3.3: Evolution of the film composition as a function of sample depth determined by SIMS and normalized to one at 1500 s sputter time, i. e. 0.25 sample thickness, of sample depth. The metal ratios are calculated from the elemental composition calibrated by the EDX composition measured at 1500 s depth marked with a gray line.

The EDX composition measured at a depth equivalent to 1500 s of sputtering is used to calibrate the SIMS (Cu 22.5 at. %; Zn 8.2 at. %;Se 43.7 at. %; Sn 12.4 at. %, Ga 8.8 at. %; As 4.5 at. %. This composition results in a Zn/Sn ratio of 0.66 and Cu/(Zn+Sn) ratio of 1.09). The top of the sample was etched away for 150 s in a bromine solution (Br_2-MeOH 0.02 M) for this measurement. The equivalence between the depth scales, i. e. sputter time and etch time, is calculated, assuming constant etch and sputter rates. The etch rate is estimated by measuring the sample thickness change by SEM cross section imaging for a known etch time. The sputter rate is calculated knowing the thickness and the sputter time needed to sputter through the deposit.

Looking carefully at the SIMS, one would assume it is better to calibrate at deeper sample depths (for example 2000 s). This assumption cannot be made since at higher sample depths, due to the high probing depth with the used electron beam acceleration energy of 20 keV, the gallium and arsenic signals start to appear and thus significantly affect the analyzed composition.

The metal ratio [Cu/(Zn+Sn) and Zn/Sn] evolution from the SIMS analysis, calibrated by the composition measured by EDX at an equivalent depth

to 1500 s, are also shown in figure 3.3.

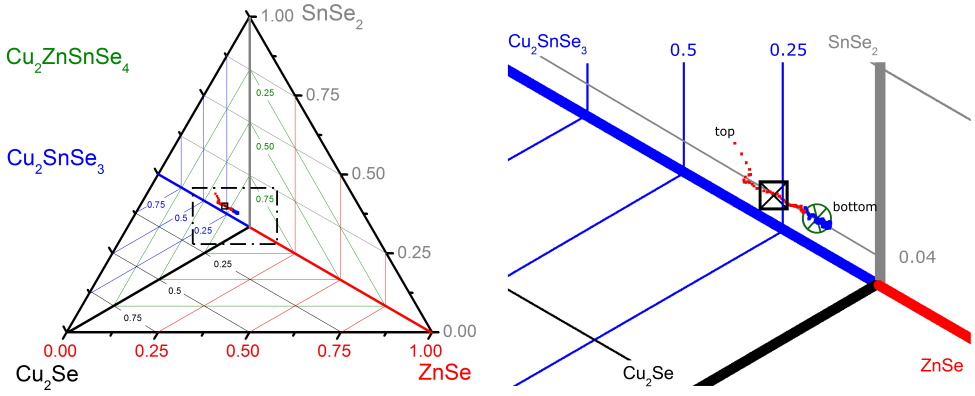

(a) (b)

Figure 3.4: Metal ratios from the calibrated SIMS plotted in the ternary phase diagram (figure a) and a zoom-in in the region of interest (figure b). The zoomed area of figure a is marked with a dashed black rectangle. 0-1500 s sputtering (red), 1500-5500 s (blue), the black square shows the composition of the as grown sample. In figure b an extra line of constant $SnSe_2$ is added (at 0.04 $SnSe_2$) while the CZTSe lines are deleted for clarity. The bottom and top of the sample are indicated. The green circle in figure b represents the composition at the depth where the spectrum from figure 3.6b is measured.

The depth at which the data is calibrated is indicated in figure 3.3 by a change in the metal ratios color from red to blue. These metal ratios are plotted in the ternary phase diagram depicted in figure 3.4 where the same color code is used. One can see that all the points of the depth dependent composition are still in the CZTSe-$SnSe_2$-CTSe triphase region. The figure also shows that the CTSe content decreases with the depth of the sample since the depth dependent composition evolves mainly parallel and close to the CTSe/CZTSe tie line. This means that the phases contained in the film are mainly CZTSe and CTSe and that the $SnSe_2$ content is constantly low. It should be noted that the $SnSe_2$ content is lower than estimated. It could even be 0 since the width of the two phase region (CZTSe-$SnSe_2$) is neglected.

This wide spread range of composition hints towards the fact that this sample does not consist of a single phase. The possible multi-phase behavior can be traced in the Raman measurements; the green excitation Raman spectrum measured on the surface of the sample shows a broad peak in the energy range of the main modes of CZTSe (i. e. 160-200 cm^{-1}) and two further broad peaks at 215 cm^{-1} and 240 cm^{-1}, as shown in figure 3.5.

The fitting of the energy range of the main Raman mode is also shown in the figure. Three Raman modes can be discerned; the CZTSe Raman spectra are fitted with a broadened Lorentzian (detailed in section 4.1) peak shape for the main Raman mode and a pure Lorentzian peak shape for the lower intensity mode at 170 cm^{-1} and the extra mode at 181 cm^{-1}. In addition to CZTSe a further material with a Raman mode at 181 cm^{-1} is present in the sample which is preliminarily attributed to Cu_2SnSe_3 (CTSe) in accordance with literature [53].

The energy range 200-260 cm^{-1} is not fitted since both possible phases CTSe and CZTSe have minor Raman modes in this energy range making a clear fit impossible. Further depths, realized by etching away the top

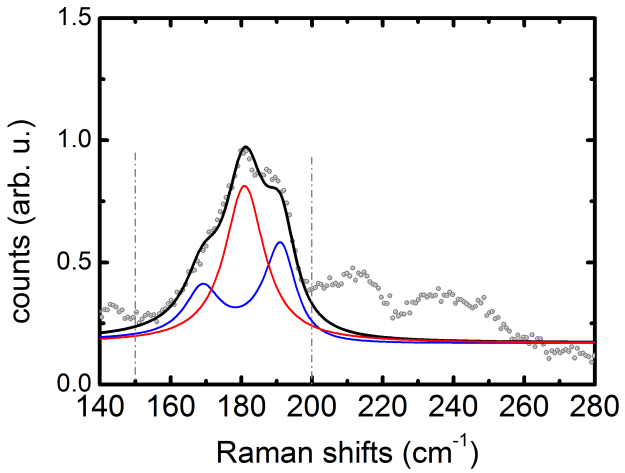

Figure 3.5: Green excitation Raman spectrum (514.5 nm) of an as grown CZTSe sample on GaAs substrate, fitted with the main peaks of CZTSe and CTS in the energy range 150 cm^{-1} to 200 cm^{-1} (marked in gray). The measured data is shown in grey circles. The main CZTSe modes are fitted by a blue line, the CTSe mode is depicted in red. The black line shows the sum of the single peaks used for fitting.

of the sample, were analyzed by Raman spectroscopy with a diminishing contribution of the extra mode with growing sample depth, as shown in figure 3.6. The two depths shown in figure 3.6 are also fitted with the same peak positions and shapes used for fitting the Raman spectra of the un-etched sample (figure 3.5). The first sample depth (figure 3.6a) presents a low contribution of the 181 cm^{-1} mode, which is undetectable at the deeper sample depth shown in figure 3.6b.

This extra mode could have been attributed to $SnSe_2$ which has a main A mode at 185 cm^{-1} [89], although it is shifted by around 4 cm^{-1}. The extra

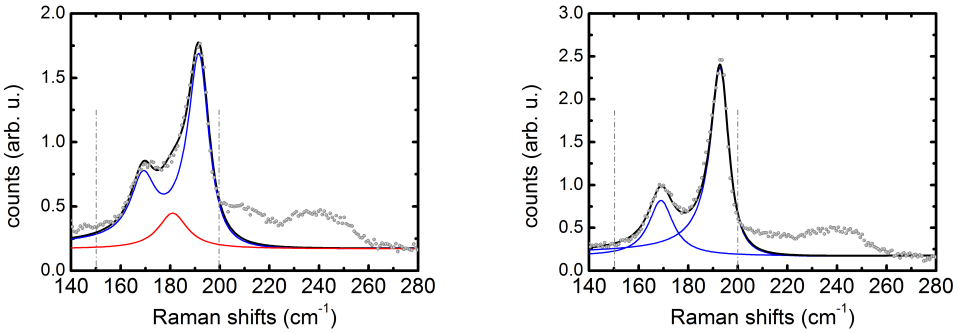

(a) 150 s etched (b) 250 s etched

Figure 3.6: Raman spectra (514 nm) of CZTSe on GaAs measured at different depths realized by Br_2-MeOH 0.02M etching for different times fitted in the energy range 150 cm^{-1} to 200 cm^{-1}(marked in gray). The measured data is shown in gray circles. The main CZTSe mode fits are depicted by a blue line, the extra mode is depicted in red (figure a). The black line shows the sum of the single peaks used for fitting.

mode at 181 cm^{-1} is however attributed to the CTSe main mode in agreement with the literature values tabularized in section 1.4.2. The strongest argument for this assignment is that $SnSe_2$ does not grow epitaxially on CZTSe since the crystal parameters are too different. Assuming we have some $SnSe_2$ in the layer, this would lead to polycrystalline growth of the film which is contradictory to the epitaxial growth suggested by the cross section SEM image shown in figure 3.2.

The assignment of the 181 cm^{-1} mode to CTSe and not to $SnSe_2$ is strengthened by the fact that the depth dependent phase composition follows the same tendency as the content of the extra mode at 181 cm^{-1} (figure 3.4). In fact, the depth-dependent phase composition extracted from the phase diagram (see figure 3.4) suggests a decreasing CTSe content with a rather constant $SnSe_2$ content. This behavior fits the evolution of the Raman signal of the extra mode at 181 cm^{-1}.

The detection limit by green excitation Raman spectroscopy of the CTSe can be estimated to 20%. This is the relative CTSe content in the phase composition given by the phase diagram at the depth at which the CTSe Raman mode is not seen anymore in the Raman spectrum i. e. 250 s etch time which corresponds to 500 nm depth, 2800 s sputter-time and 0.42 normalized depth. This is the case for the composition marked with the green circle in figure 3.4b and corresponds to the spectrum shown in figure 3.6b. It should

be noted that this estimation of the detection limit is based on the adapted phase diagram which neglects the size of the single phase CZTSe. A larger single phase region would lower this estimation accordingly.

The depth dependent composition simultaneously assumes and points to the fact that CTSe and CZTSe are present with different relative contents in different depths. Playing the devils advocate one could assume that the CTSe grows as a layer on CZTSe, that the Raman signal of mixed phases is seen due to a much higher Raman efficiency for the underlying CZTSe and that the expected step in the SIMS (for a layered material) is smoothed out due to some other artifact. However there is no indication for a layered structure in the cross section SEM micrograph (see figure 3.2). Further, the Raman signal of the ternary only becomes undetectable at a depth of about 500 nm which is higher than the probing depth of Raman measurements. This leads to the conclusion that the surface of the sample is composed of a CTSe/CZTSe mix. Since there is no indication in the SEM micrographs in both top view and cross-section for a phase separation (see figures 3.2 and 3.7), one can assume that the mix of CZTSe/CTSe is a syntactic growth (a three dimensional epitactic mix) [90]. The crystal structures need to match in all three directions for such a growth.

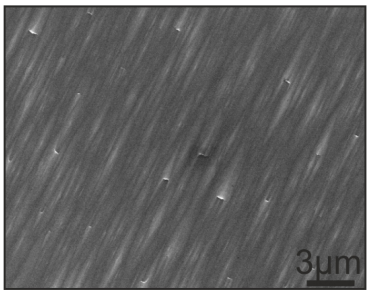

Figure 3.7: Top view SEM micrograph of MBE deposited CZTSe on GaAs (001) surface. Same sample as in figure 3.2.

The lattice mismatches, assuming CZTSe as a substrate, are calculated for the CTSe phases known in literature. These are summarized in table 3.1. The lattice parameters of the cubic Cu_2SnSe_4 defective compound and the sphalerite Cu_2SnSe_3 fit those of CZTSe since they have lattice mismatches of the order of 0.2 % and -0.6 %, respectively. Thus these two latter cubic compounds would grow epitaxially on CZTSe since they fit the lattice parameters while having the same underlying zincblende structure. They are therefore considered possible origins of the 181 cm^{-1} Raman mode. The monoclinic Cu_2SnSe_3 phase can grow epitaxially on the CZTSe since both structures are commensurate. The monoclinic CTSe, doubly elongated along its b axis, fits diagonally on three by three CZTSe unit cells. The CTSe has to be further rotated around its c axis so that Cu-Sn planes of both materials align. This orientation is discussed in detail by Amiri et. al. in [91] and shown in

figure 3.8. The lattice mismatches noted in table 3.1 show that the monoclinic CZTSe can grow epitaxially on the CZTSe in a layered manner while a syntactic growth is improbable since the (001) direction is incommensurate i. e. the Cu-Sn distance (defined in figure 3.8) is considerably different from the inter-layer distances of CZTSe in the (001) direction.

The latter considerations lead to the conclusion that the cubic phases (the cubic and the sphalerite CTSe[2]) are more probable than the monoclinic CTSe in the above examined sample and therefore to the assignment of the 181 cm^{-1} Raman mode to one of these cubic phases.

The discussion above shows that reference spectra are missing in the CTSe Raman literature and that the spectrum assigned to the monoclinic phase might be originating from a cubic phase since it is probable that two CTSe phases have different Raman spectra.

[92]CZTSe a	5.695	mismatch in %
[68] cubic Cu_2SnSe_4 a	5.685	0.2
[66] sphalerite Cu_2SnSe_3 a	5.73	-0.6
[63] monoclinic Cu_2SnSe_3 $2 \times b$	24.16†	-0.3
[63] monoclinic Cu_2SnSe_3 Cu-Cu	5.67	-0.4
[63] monoclinic Cu_2SnSe_3 Cu-Sn	3.96*	-30.4*

Table 3.1: Calculated lattice mismatches for CTSe phases assuming CZTSe as a substrate. The lattice parameters (in Å) are given for CZTSe and CTSe. The monoclinic Cu_2SnSe_3 is arranged on the CZTSe as proposed by [91] and defined in figure 3.8. The distances Cu-Cu, Cu-Sn, and $2 \times b$ are to be compared to the interlayer distances in CZTSe and are defined in figure 3.8. The value marked by † is to be compared to $\sqrt{2} \times 3a$ CZTSe since the doubly elongated b axis of CTSe is arranged diagonally in three by three CZTSe unit cells. The value marked by * gives the mismatch of the Cu-Sn distance to a which is the relevant distance in the (001) direction of the CZTSe unit cell.

A further result of this measurement series is that the contribution at 215 cm^{-1} is independent of the mode at 181 cm^{-1} and thus comes from a different material. This mode can be attributed to CZTSe as will be discussed in section 4.3. The modes in the energy range 230-250 cm^{-1} only correlate to the intensity of the mode at 215 cm^{-1} but since Raman modes of both

[2]The cubic and the sphalerite CTSe are both cubic structures. The designations used here are as used in CTSe literature.

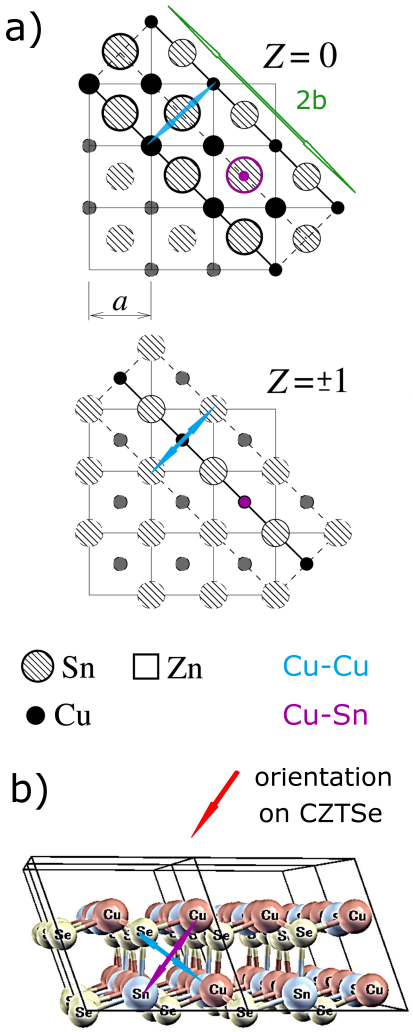

Figure 3.8: Doubly elongated monoclinic unit cell on 3×3 unit cells of CZTSe sliced in (001) direction at Z=0 and Z=1 (shown in figure a). Thick lines show the border of the unit cell while dashed ones show their projection on the considered layer. The unit cell of the monoclinic CTSe is shown in figure b. The distances Cu-Cu (blue), Cu-Sn (purple), $2b$ (green) are added along with the orientation direction of the CTSe on the CZTSe (red arrow). Adapted from [91].

CTSe and CZTSe are expected in this energy range no further insights can be extracted.

3.2 Tin-selenides (SnSe and $SnSe_2$)

During the growth of CZTSe samples tin-selenides (SnSe and $SnSe_2$) can also be formed. In this section, the detection of tin-selenides as a secondary phase of CZTSe by Raman spectroscopy is examined. The use of concentrated hydrochloric acid (HCl) to remove the tin-selenides phases is also demonstrated. The data shown here is published in [93].

Discrimination of tin-selenides by Raman spectroscopy

The sample discussed in this section is prepared by annealing a SnSe capped precursor. The precursor was made by the simultaneous low temperature (320 °C) evaporation of elements needed for CZTSe followed by the deposition of a SnSe capping layer in the MBE machine (as introduced in section 2.2.3). The purpose of this capping layer is the protection of the precursor from oxidization. It further provides SnSe where it is needed i. e. at the surface of the absorber. It therefore might prevent the absorber from decomposition in the early stages of annealing.

In the following, the 'as grown' state refers to the sample as it comes out of the MBE machine. The 'processed' state of the sample refers to the same sample after heat treatment. Raman spectra measured on this sample in both states are shown in figure 3.9.

The Raman spectrum depicted in the figure 3.9a is fitted with Lorentzian peaks. It presents a dominant Raman mode at 182 cm^{-1} and three lower intensity modes at around 114 cm^{-1}, 106 cm^{-1} and 250 cm^{-1}.

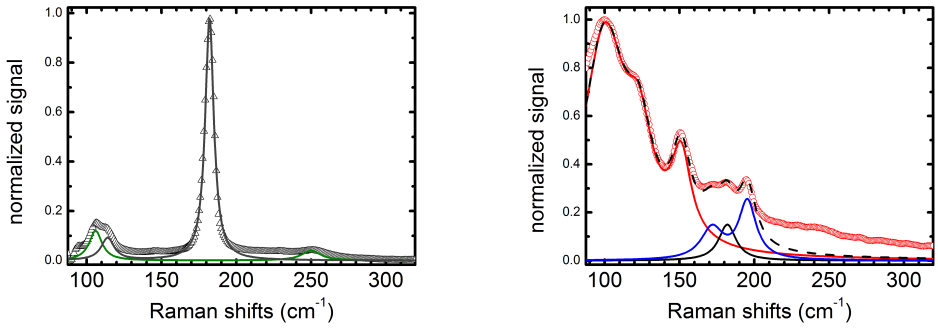

(a) as grown (b) as processed

Figure 3.9: Green excitation Raman spectra (514 nm). The main peaks are fitted with Lorentzian curves (except for the main CZTSe peak which is fitted with an asymmetric Lorentzian in figure b). The spectra in figure a is fitted with the typical peak positions for $SnSe_2$ (dark grey) and amorphous Se (green). The one in figure b is fitted with the typical peak positions for $SnSe_2$ (dark grey), SnSe (red), CZTSe (blue) and the sum of the fitting peaks is represented by the dashed black line.

The two modes at 182 cm^{-1} and 114 cm^{-1} are in reasonable agreement with the literature values for $SnSe_2$ [89]. There is a shift of around 2 cm^{-1} which can be due to differences in energy calibration or strain. The Raman

modes at 250 cm^{-1} and 106 cm^{-1} can be assigned to amorphous Se in the near-surface region [94].

After the heat treatment, the surface becomes a mixture of SnSe, $SnSe_2$ and CZTSe as indicated by the Raman analysis. The measured Raman spectrum is broad and shows a multitude of peaks (presented in figure 3.9b). It can be fitted with the characteristic peak positions of the mentioned material mix. Such a fit is shown in the figure 3.9b: the CZTSe peaks are fitted at 172 cm^{-1} and 195 cm^{-1} (shown in blue), the $SnSe_2$ peaks fitted at 182 cm^{-1} (plotted in black) and the SnSe peaks are fitted at 100 cm^{-1}, 123 cm^{-1} and 151 cm^{-1} (depicted in red). The peak identification was made by comparison with the literature values summarized in sections 1.4.2 and 1.4.2.

The surface composition changed from a mixture of $SnSe_2$ and amorphous selenium to a mixture of CZTSe, $SnSe_2$ and SnSe which, according to the Sn-Se phase diagram by Sharma et. al. [95], is the result of a decrease of the Se/Sn ratio during the annealing. This apparent Se loss is explained by the decomposition of the $SnSe_2$ capping layer following [96]:

$$\begin{aligned} SnSe_2(s) &= SnSe(s) + \frac{1}{x}\, Se_x(g); \quad (x = 2\text{-}8) \text{and:} \\ SnSe(s) &= SnSe(g) \end{aligned}$$

where the gaseous phases can leak out of the annealing box and condensate on the cooler walls of the furnace.

Selective etching of tin-selenides by HCl

This section discusses the selective removal of the tin-selenide(s) layer by HCl etching. The same sample as above is used and its Raman analysis is discussed.

The 'as processed' sample is etched for 10 min in concentrated HCl. This new state of the sample is referred to as the 'HCl etched'. Figure 3.10 depicts the Raman spectra of the sample discussed in the last section after the oven annealing (figure a) and in the 'HCl etched' state (figure b).

The spectrum of the etched sample (figure 3.10b) shows the characteristic CZTSe modes at 172 cm^{-1}, 195 cm^{-1}, 234 cm^{-1} and 244 cm^{-1}. The fit of the main two modes is also shown in figure 3.10b. This fit suggests that the $SnSe_2$ contribution in the Raman spectrum has completely disappeared after HCl etching since the main modes of CZTSe suffice to fit the spectra in the energy range where the main $SnSe_2$ mode is located (i. e. 150-220 cm^{-1}).

The removal of the $SnSe_2$ layer is confirmed by SEM microscopy. In fact, prior to etching, the surface of the absorber is almost covered by a smooth layer as seen in figure 3.11a. After etching the top view SEM micrograph

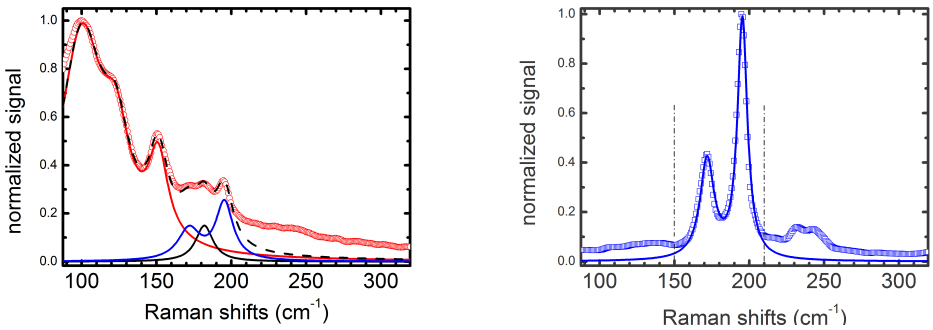

(a) as processed (b) HCl etched

Figure 3.10: Green excitation (514 nm) Raman spectra of the absorber in the 'as processed' (figure a) and 'HCl etched' state (figure b). Figure a is the same as figure 3.9b repeated for convenience. The measured data is shown as circles. The main CZTSe modes in figure b are fitted by a blue line in the energy range 150-210 cm^{-1} (the main mode is fitted with an asymmetric Lorentzian while the peak at 175 cm^{-1} if fitted with a Lorentzian peak shape).

of the 'HCl etched' state presents the expected rough surface known from poly-crystalline CZTSe samples (SEM shown in figure 3.11b).

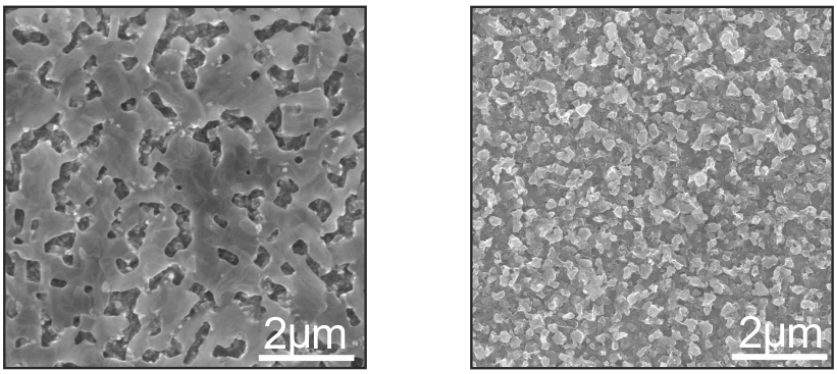

(a) as processed (b) HCl etched

Figure 3.11: Scanning electron micrographs of the surface of the 'as processed' state (a) and the 'HCl etched' state (b).

3.3 Zinc-selenide (ZnSe)

According to the phase diagram, Zinc-selenide (ZnSe) is, apart from $SnSe_2$ the secondary phase that forms when CZTSe films are prepared Cu-poor and Zn-rich. This Cu-poor Zn-rich composition is usually targeted because it results in the best solar cells [97] as proven by empirical observations, therefore the detection of this secondary phase is important.

The simplest way to detect the presence of ZnSe is to use blue excitation quasi-resonant Raman spectroscopy. However, green excitation photoluminescence is usually more available and samples a larger volume. It is therefore valuable to have a PL fingerprint of ZnSe. Actually, a PL signal peaking at 1.2-1.4 eV is seen on Cu-poor Zn-rich samples. The main result of this chapter is the assignment of this emission to ZnSe.

A spatial correlation assigns this PL signal to ZnSe: the laterally varying photoluminescence transition intensity is correlated to the variation of the characteristic ZnSe Raman spectrum. This identifies the transition as a luminescence of ZnSe. The main advantage of such a ZnSe discrimination tool is that due to a larger sampling volume, even small amounts that are barely seen in blue excitation Raman spectroscopy can be discerned. These results are published in [98], confirming the tentative assignment of the PL to ZnSe published in [99].

The detection of ZnSe is discussed in this section based on the measurements made on two samples, the first one is chosen since it is very Zn-rich (denoted A) and the second one (denoted B) is chosen since it resulted in a champion solar cell (6.2 % conversion efficiency). The compositions of both samples are plotted in the ternary phase diagram depicted in figure 3.12. The latter sample is also discussed in the publications [85, 100, 98].

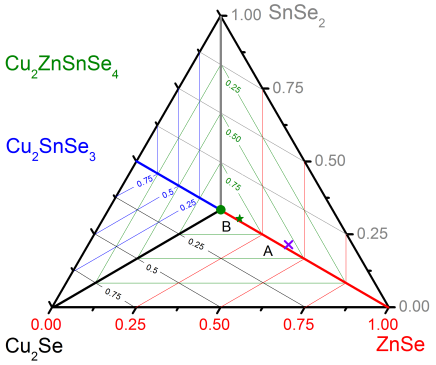

Figure 3.12: Composition of the samples discussed in this section plotted in the adapted phase diagram. The purple cross represents the composition of sample A discussed in the subsection: *Lateral correlation*, the green star represents the composition of the sample B discussed in the subsection: *Depth correlation*.

Photoluminescence at 1.2-1.4 eV

A broad PL signature peaking at 1.2-1.4 eV is seen on a large number of CZTSe samples. This luminescence is preliminary attributed to ZnSe.

The variation of the peak energy is demonstrated in figures 3.16a and 3.17, which show the green excitation (514 nm) photoluminescence measured on CZTSe samples. This variation can be attributed to different doping or impurity concentrations and/or to different doping materials, e.g. Cu and/or Sn. The presence of doped ZnSe in the absorber (expected for the composition) is proven by atom probe tomographies (APT) [100]. It should be noted that the APT measurements were also performed on sample *B*. The reconstructed 3D view of Cu, Sn and Zn is presented in figure 3.13. In addition, the iso-concentration surface of 32.5 at. % Zn is depicted. This representation indicates the presence of Zn-rich areas proving that the measured volume contains nm-sized networks of ZnSe inclusions in the CZTSe layer. Line-scans of the integrated elemental concentration [85, 100] showed that the sample is divided into highly Cu and Sn doped ZnSe (up to 3 %) and CZTSe like areas.

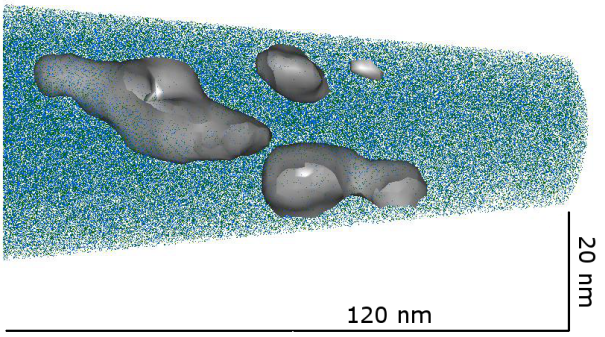

Figure 3.13: Atom probe tomography of sample *B*: three-dimensional elemental map of Cu, Zn and Sn shown in blue, gray and green, respectively. An iso-concentration surface of Zn at 32.5 at. % Zn is depicted in grey. Courtesy of Thorsten Schwarz.

The PL signal peaking at 1.2-1.4 eV is higher than the calculated (summarized in section 1.1) and measured [101, 102] band gaps of CZTSe. It is also higher than the absorption edge observed in the quantum efficiency spectrum measured in solar cells made from this absorber. It can be therefore attributed to a secondary phase of higher band gap.

The two samples discussed in the next two subsections are Cu-poor and Zn-rich so ZnSe and SnSe-$SnSe_2$ are the most probable secondary phases according to the ternary phase diagram (see figure 3.12). Nevertheless, SnSe

and $SnSe_2$ can be excluded since these phases were not detected in green excitation Raman spectroscopy. A thin layer of SnSe and $SnSe_2$ could be easily discerned in green excitation (514.5 nm) Raman spectroscopy as reported in [93] and detailed in the previous section (3.2). By exclusion, ZnSe is the only phase left to attribute this luminescence to assuming the phase diagram is complete and thermal equilibrium is reached.

A PL transition was presented in [99] which could be attributed to the band-to-band transition of ZnSe. figure 3.14 depicts UV(363.8 nm) excited photoluminescence of a CZTSe sample showing the same 1.3 eV transition (in green excitation) assigned to ZnSe. The UV excited spectrum shows a transition at 2.2 eV and another transition at 2.8 eV. The higher transition could be attributed to the band to band transition in ZnSe, while the lower one could be attributed to a further defect luminescence in ZnSe since it is higher than the band gaps of all possible secondary phases in CZTSe (except ZnSe).

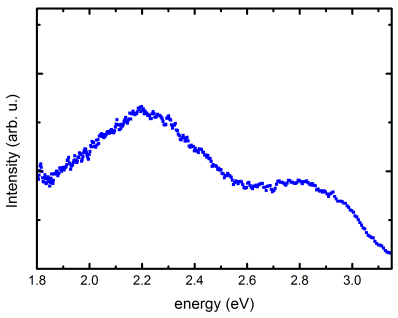

Figure 3.14: UV excited PL spectrum (363.8 nm) measured on a CZTSe absorber.

Nevertheless, a direct proof of the ZnSe phase by a phase selective method was missing. The fact that we observe luminescence in ZnSe with an excitation energy lower than its proper band gap (514 nm, excitation corresponds to 2.1 eV), is attributed to highly defective ZnSe, which contains a high concentration of Cu and Sn impurities [100]. Since the ZnSe in our samples is proven to have a high defect density and since the excitation energy is lower than the band gap of ZnSe it is expected that the excitation occurs via defect related energy levels.

Various impurity-related luminescences have already been observed far below the band gap in ZnSe [103, 73, 104] so it is possible that the PL at 1.2-1.4 eV is a further impurity-related luminescences. A proof for the definitive assignment of this PL to ZnSe is given in the next two subsections.

Lateral correlation

In this section, a zinc rich electro-deposited and annealed sample is used to demonstrate the lateral spatial correlation between the PL and the Raman signals. The sample preparation is detailed in section 2.2.1. The sample chosen for this correlation is Zn-rich and therefore ZnSe rich (see sample *A* in figure 3.12). In addition to being abundant, the ZnSe is mostly on the surface of the sample as resulting from its preparation[3]. The same area of the sample is spatially resolved with both techniques (Raman and PL) to compute the correlation coefficients between the known Raman spectra and the PL signal of CZTSe and ZnSe. The correlation is then used to assign the PL to ZnSe.

Figures 3.15 show representative PL spectra taken at green (514 nm) excitation. The photoluminescence spectrum shows a broad dominant transition at 1.3 eV and a second transition of lower intensity seen as a shoulder at about 0.9 eV.

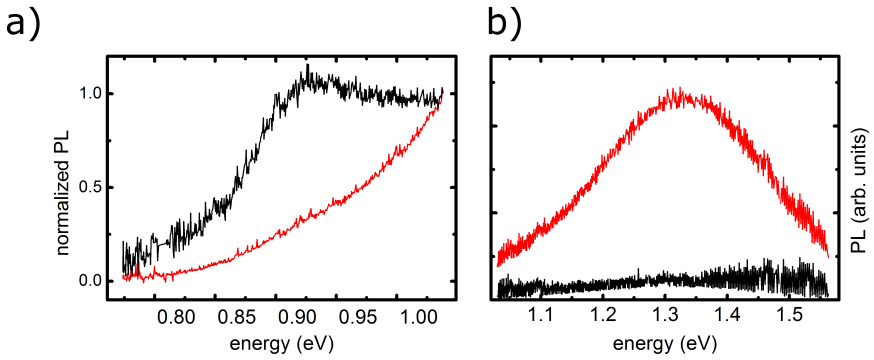

Figure 3.15: PL measured on sample *A* depicted in two energy ranges 0.77-1.05 eV (figure a) and 1-1.6 eV (figure b) for two representative points for high (plotted in red) and low 1.3 eV (plotted in black) PL. In figure a the spectra are normalized to 1 at 1.05 eV and to 0 at 0.77 eV.

These two transitions occur at different relative intensities across the sample surface. The low energy transition is usually attributed to CZTSe [105] and will be discussed in detail in the next chapter.

The proof that this luminescence is in fact a radiative transition in ZnSe is provided by the spatial correlation between the RT-PL and the blue excitation Raman spectroscopy signals. The spectra shown in figure 3.16 are from

[3]The sample is prepared by the selenization of an electro-deposited metal stack where zinc is in the top layer.

two points of the same $80\times80\,\mu m^2$ scanned by green excitation PL and blue excitation Raman spectroscopy. The spectra shown in the same color are from the same points representative for areas with high (plotted in red) and low (plotted in black) 1.3 eV PL signal. The ZnSe contribution is dominating both the Raman and the PL spectra, therefore it is in some cases necessary to normalize the PL and Raman data for each point of the mappings in order to deconvolute the small CZTSe-related signal from the ZnSe signal, as discussed below.

Figure 3.16a shows the broad PL transition at 1.3 eV. For the related mappings the as-measured intensity is integrated. The normalized PL in the energy range 0.77-1.07 eV is depicted in figure 3.16b.

However, the signal height is strongly influenced by the peak tail of the emission at 1.3 eV. To take this background into account, the intensity at 0.77 eV is set to zero and the intensity at 1.07 eV is set to 1. Thus, the contributions from the 1.3 eV peak are subtracted to highlight the CZTSe contribution. This is a valid correction under the assumptions that the CZTSe related PL is negligible at the limits of this energy range and neglecting spectral shape changes in the 1.3 eV PL. The normalization makes the CZTSe PL contribution almost independent of the 1.3 eV PL.

The mapping shows the integrated intensity of the normalized spectra. The Raman spectra from the same areas are shown in figures 3.16c and 3.16d with different normalizations. For both figures the backgrounds are corrected by setting the high energy end of the spectrum to zero (700-800 nm). The rest of the reflected laser at 50 cm^{-1} is normalized to 1 in 3.16c to correct for different reflectivities at different points of the sample. The reflected laser is seen as a measurement artifact at 50 cm^{-1}. This is the incompletely removed part of the Rayleigh scattered laser light that is not cut off by the long pass edge filter.

The mapping in figure 3.16c shows this normalized intensity integrated from 230-260 cm^{-1}, i. e. in the spectral range of the main ZnSe mode. In order to better highlight the signal from CZTSe, the Raman signal shown in figure 3.16d was normalized to the peak at 250 cm^{-1} which is almost exclusively due to a ZnSe mode. This normalization shows the relative contribution of CZTSe compared to ZnSe when the peak at 170 cm^{-1} is integrated, since this spectral range exclusively represents a CZTSe mode, with very little contribution from ZnSe. This is opposed to the main mode of CZTSe at 195 cm^{-1} which is very close in energy to the TO phonon of ZnSe measured here at ≈200 nm.

The insets in 3.16 show the $80\times80\,\mu m^2$ maps of the RT-PL (figures 3.16a and b) and Raman (figures 3.16c and d) signals integrated in the energy ranges where the signal is dominated by either CZTSe or ZnSe. In order to

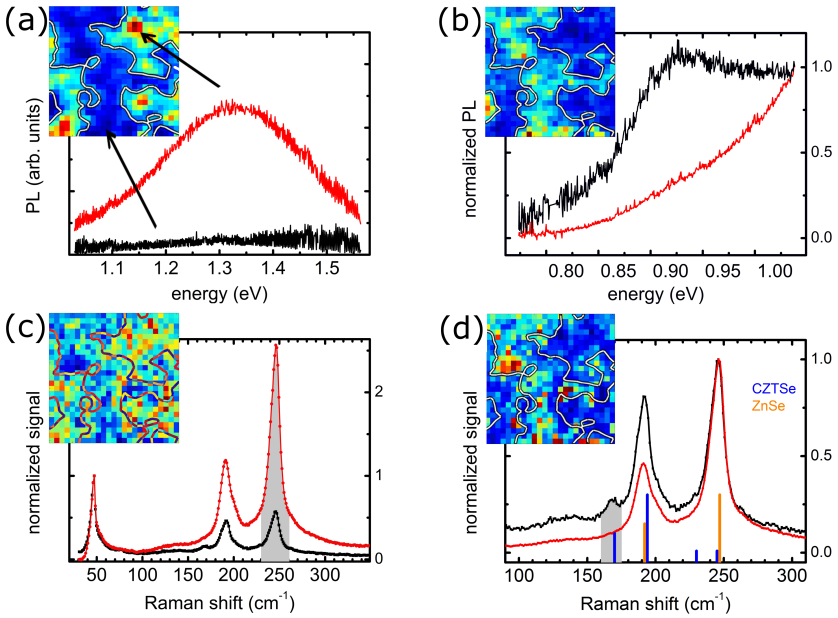

Figure 3.16: Representative room temperature PL (514.5 nm excitation) and Raman (457.9 nm excitation) spectra from the same $80 \times 80\,\mu m^2$ mappings from areas of high (red) and low (black) 1.3 eV PL signal. Figures a and b are the same as figure 3.15 and depict different spectral ranges of the PL. Figure c and d are normalized to the reflected laser beam and to the main peak, respectively. The insets show maps of spectrally integrated signals of the following energy ranges: a) 1.0-1.6 eV (ZnSe), b) 0.77-1.05 eV (CZTSe), c) 230-260 cm^{-1}(ZnSe, marked gray), d) 160-175 cm^{-1} (CZTSe, marked gray). The intensities are given in arbitrary units with increasing intensity from blue over yellow to red. The contour from the inset of figure a is plotted in the insets of figures b to d as a guide to the eye.

highlight the correlation, one contour line from the RT-PL map (figure 3.16a) is plotted in the other maps (figures 3.16b, c and d) as a guide to the eye. Comparison of the patterns in the maps indicates that the respective maps of ZnSe and CZTSe are anti-correlated, while the maps of ZnSe in PL (figure 3.16a) and in Raman (figure 3.16c) are correlated as well as the maps of CZTSe in PL (figure 3.16b) and Raman (figure 3.16d). To further corroborate the anti-correlation of these signals, the Pearson product-moment correlation coefficient (PCC)[4] [106] was computed.

[4]The PCC of two variables X and Y is given by their covariance (cov) divided by the product of their standard derivations σ_i:

$$\rho_{X,Y} = \frac{\mathrm{cov}(X,Y)}{\sigma_X \sigma_Y}$$

The PCCs are given in table 3.2. There is a strong anti-correlation of -0.8 between the two PL maps (representing the ZnSe and the CZTSe signal) as well as between the two Raman maps (representing the ZnSe and the CZTSe signal). This anti-correlation indicates that the areas with ZnSe and with CZTSe signal can be clearly separated in both maps. The (anti-) correlations between PL maps and Raman maps are considerably weaker, as is expected taking the different necessary normalizations into account. Still, there is significant correlation between the ZnSe PL map and the Raman map. This clearly shows that the PL signal at 1.3 eV is in fact due to a luminescent transition in ZnSe.

	PCC	CZTSe PL 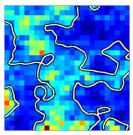	CZTSe Raman 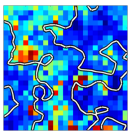	ZnSe Raman 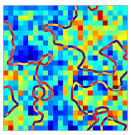
ZnSe PL 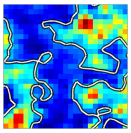		-0.76	-0.41	0.45
ZnSe Raman 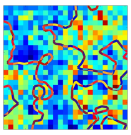		-0.46	-0.79	
CZTSe Raman 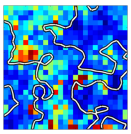		0.34		

Table 3.2: Pearson product-moment correlation coefficient (PCC) for the integrated PL and Raman signals for CZTSe and ZnSe. The insets of figure 3.16 are repeated for convenience.

The comparably low PCC of the Raman and PL signal of CZTSe of 0.34 is due to the fact that there is no energy range in either spectrum which is purely due to a CZTSe signal. The background of the pure CZTSe Raman peak at 170 cm^{-1} is given by the peak at 190 cm^{-1} which has ZnSe and CZTSe components and the PL signal around 0.9 eV has a strong background from the broad 1.3 eV ZnSe peak.

The PCC values range from -1 to 1 for fully anti-correlated to fully correlated samples.

Depth correlation

This section shows that ZnSe defect luminescence also correlates with the Raman signal of ZnSe as a function of the depth of the film. This RT-PL ZnSe discrimination enables us to discern ZnSe secondary phases in CZTSe that are not easily discernable by blue excitation Raman spectroscopy. The different depths of the sample become accessible in this experiment by sputtering craters of different depth into the sample. The sputter damaged layer is removed by a 10 s etch in a 0.02 M Br_2Me-OH solution. Exemplary PL and Raman signals from the depth resolved study are shown in figures 3.17 and 3.18 measured at the normalized depths of 0.25 and 0.6, respectively.

An exemplary RT PL spectrum is plotted (black), showing the expected PL peak from CZTSe at around 0.95 eV with a high energy shoulder that is attributed to ZnSe. The fit of this ZnSe emission is depicted in red, with a maximum at 1.2 eV. The blue graph in figure 3.17 is a corrected 'CZTSe only' spectrum obtained by subtracting the ZnSe peak from the measured spectrum which demonstrates that the ZnSe PL is still accessible.

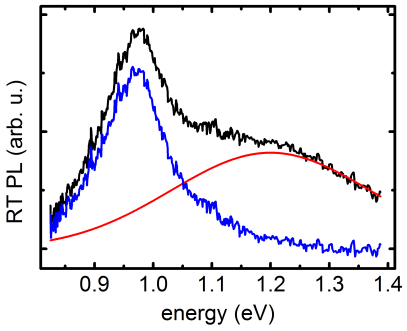

Figure 3.17: RT-PL spectrum taken on CZTSe (black). A fit of the luminescence attributed to ZnSe is shown in red. The remaining part of the spectrum i. e. the signal related to CZTSe is depicted in blue.

Figure 3.18 shows two Raman spectra taken at green and blue excitation wavelengths measured at the same sputtered depth. The ZnSe Raman signal is very low and never dominates the spectrum. Only the main mode at 250 cm^{-1} is seen when blue excitation is used. This peak probably has contributions from CZTSe. To distinguish ZnSe, the intensity ratio of the peaks at 250 cm^{-1} and 235 cm^{-1} (pure CZTSe peak) is chosen to quantify the ZnSe content, assuming a comparable peak height of the two CZTSe modes at 235 cm^{-1} and 250 cm^{-1}. The intensity ratio I_{ratio} is given by:

$$I_{ratio} = \frac{I_{250} - I_{235}}{I_{250}}$$

where the intensities of the peaks at 250 cm^{-1} (I_{250}) and 235 cm^{-1} (I_{235}) are given in arbitrary units.

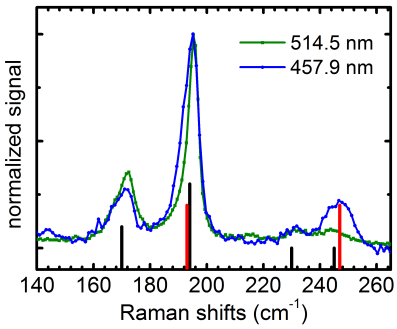

Figure 3.18: Normalized Raman measurements taken at the same depth of the sample at different excitation wavelengths (green for 514.5 nm excitation, blue for 457.9 nm excitation). ZnSe (red) and CZTSe (black) peak positions are marked.

The depth dependent ZnSe signal derived from PL and Raman is depicted in figure 3.19. The ZnSe PL intensity and the ZnSe content acquired from the Raman peak ratio are plotted as a function of the depth of the film. The observed correlation between the two measurements further strengthens the attribution of the PL signal at ≈1.25 eV to the ZnSe phase.

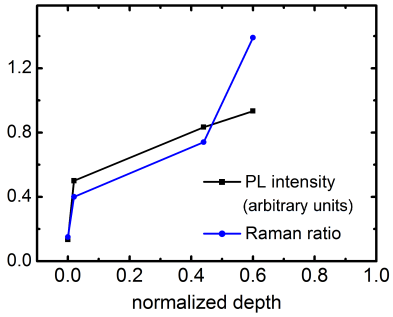

Figure 3.19: PL intensities and Raman peak intensity ratio as a function of normalized depth.

The blue excitation ZnSe contribution in the Raman spectrum is only seen in comparison with the green excitation Raman spectrum. This shows the power of the RT-PL ZnSe discrimination. The reasons for the lower Raman response are multiple: the sample discussed in this section (sample B in figure 3.12) is Zn-poorer than sample A which means the sample contains less ZnSe which lowers the ZnSe Raman signal. The ZnSe is differently distributed in the samples due to different growth procedures. Sample B is grown by the simultaneous deposition of all elements followed by an annealing (as detailed in section 2.2.3) which leads to a more homogeneous distribution of ZnSe compared to sample A which is made by the annealing/selenization of metal layers where Zn is the top layer. This difference in ZnSe distribution leads to less ZnSe in the probing volume of sample B than in sample A. The homogeneous distribution of the ZnSe in the sample is confirmed by the atom

probe measurements shown in the beginning of the section made on the same sample.

The ZnSe PL signal is a convenient detection tool for ZnSe inclusions in CZTSe. This is due to the lower surface sensitivity (of PL compared to Raman), enabling the detection of the ZnSe secondary phase even when it is present in low and homogeneously distributed amounts in the sample.

3.4 Conclusion

This chapter treated the detection of some secondary phases on CZTSe samples by Raman and PL. In the first section, the intermixed growth of CTSe and CZTSe on Cu-rich Sn-rich samples was discussed. The contribution of the main Raman modes of these two phases was correlated to their relative content in the sample confirming the assignment of the mode at $181\,\mathrm{cm}^{-1}$ to CTSe. The CTSe literature attributes this main CTSe mode to the monoclinic phase which does not agree with the syntaxy of these two phases (i. e. mixed and oriented growth (to each other) of the crystals of CTSe and CZTSe). The cubic phases are more suitable candidates for this intermixed epitaxial-like growth since they have lower lattice mismatches to the CZTSe and GaAs lattices. These cubic phases might therefore be the origin of the Raman mode.

The second section discussed the phase composition of a $SnSe_x$ capping layer on CZTSe samples before and after annealing of the samples as detected by Raman spectroscopy. The presence of the phases $SnSe_2$ and amorphous selenium was detected in this capping layer. The measurements further confirmed that concentrated hydrochloric acid (HCl) can be used to remove the tin-selenides phases remaining on the capped CZTSe sample after heat treatment (i. e. SnSe and $SnSe_2$).

The last section discussed the ZnSe secondary phase. It is confirmed that green excitation standard Raman spectroscopy is not sufficient to detect the co-existing ZnSe secondary phase in CZTSe, blue excitation is necessary to detect the ZnSe contributions by Raman spectroscopy. A RT-PL emission at 1.2-1.4 eV was found: it could be clearly correlated to a sub-band gap excited defect luminescence of ZnSe by spatially correlating the PL emission to the known Raman signal of ZnSe. It is shown that room temperature PL is a technique sensitive to comparatively small amounts of the ZnSe secondary phase.

Chapter 4

Raman spectroscopy of CZTSe

This chapter discusses the Raman shifts measured on CZTSe. The Raman modes are summarized and the Raman spectrum is fitted showing that the main mode is asymmetrically broadened and that the energy range 170 cm^{-1} to 180 cm^{-1} is composed of two Raman modes. In a second part the nature of the main mode's broadening is explored. In the last part of the chapter, polarization dependent Raman measurements on both polycrystalline and epitaxial samples are discussed, with which the dominant polymorph in the probing volume and the growth direction of the CZTSe on the GaAs substrate can be determined. The P/O-Raman measurements were performed on epitaxial samples by Levent Gütay and Christiane Stroth at the University of Oldenburg. The modes were fitted in collaboration with Levent Gütay. The polarization dependent measurements on polycrystalline samples shown in figure 4.22 were measured at the University of Barcelona by Xavier Fontané, Victor Izquierdo-Roca, Alejandro Pérez-Rodríguez.

4.1 The Raman active modes in CZTSe

In this section the Raman modes that are attributed to CZTSe are discussed. Figure 4.1 shows an overview of the Raman modes related to CZTSe. A typical Raman spectrum measured with green excitation (514 nm) is shown in figure 4.1a and is composed of 8 modes. The three main modes are at 168 cm^{-1}, 171 cm^{-1} and 195 cm^{-1} and weaker modes are found at 51 cm^{-1}, 77 cm^{-1}, 130 cm^{-1}, 231 cm^{-1} and 244 cm^{-1}.

It should be noted that there is a variation of the mode energies between samples which is in the order of $\pm 2\,cm^{-1}$ depending on parameters such as strain, temperature and sample composition.

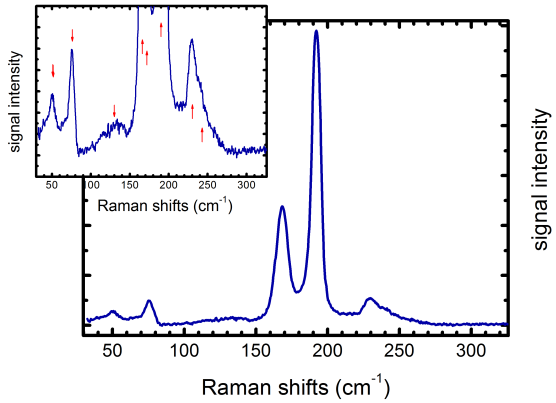

Figure 4.1: CZTSe Raman spectrum taken at an excitation wavelength of 514.5 nm. A closeup of the lower signal intensities is shown in the inset. Arrows are used to mark the peak positions. Measured at the university of Barcelona on samples produced at our laboratory. [107] .

The modes at 51 cm^{-1} and 77 cm^{-1} lie beyond the spectral cut-off of most spectrometers (including our setup described in section 2.1) therefore they are not discussed further. The mode at around 130 cm^{-1} is very broad and present in all CZTSe samples measured during this thesis. It is of comparably low signal intensity which makes it difficult to assign to the right phase.

The Raman signal in the energy range 170 cm^{-1} to 180 cm^{-1} is composed of two modes: it is often discussed in literature as one mode even though the signal seems to be composed of two overlapping peaks. This double peak behavior is discussed in the following.

Supporting the double peak notion is that the Full Width at Half Maximum (FWHM) of the peak (if considered as one peak) is about twice that of the main peak at 195 cm^{-1} (as can be seen in figure 4.2). A detailed fit also shows that this broad spectral area is composed of more than one peak: figure 4.2 shows a micro Raman measurement restricted to the energy range 145-220 cm^{-1} where a shoulder is clearly seen at 170 cm^{-1}. The fitting of the peak at 170 cm^{-1} with two Lorentzians shows that this broader Raman signal is composed of two Raman peaks at 168 cm^{-1} (5 cm^{-1} FWHM) and 172 cm^{-1} (6 cm^{-1} FWHM). The FWHM of these modes is comparable to the one of the main peak at 195 cm^{-1}(4 cm^{-1} FWHM). The quality of the fit is shown by the low and featureless residual plotted in red in the figure.

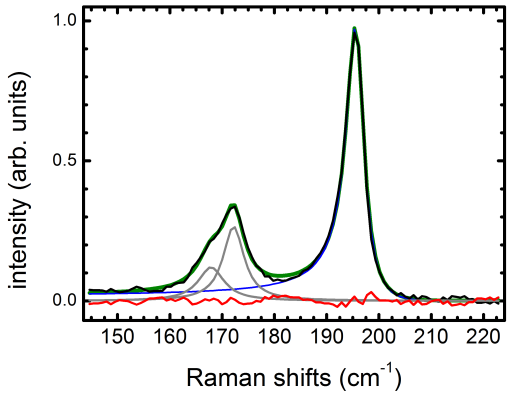

Figure 4.2: Micro Raman spectrum of CZTSe restricted to the spectral area of 145-220 cm^{-1}(black line). The main mode at 195 cm^{-1} is fitted with an asymmetrically broadened Lorentzian depicted in blue. The residual is plotted in red. The other modes at 168, 172 cm^{-1} are fitted with two Lorentzians depicted in gray. The green line shows the sum of the fits.

The main mode i. e. the mode of highest intensity which is usually at 195 cm^{-1} is discussed next. As mentioned in the background chapter (section 1.2.8) the literature values are between the extreme values of 192 cm^{-1} and 198 cm^{-1}. So far, no clear correlation was found between the peak position and the sample parameters both in literature and during this thesis. This is due to the fact that the peak position depends on sample parameters such as the elemental composition, crystal structure and strain. A major problem even if one assumes that the different samples have the same crystal structure, is that the composition and Raman measurements probe quite different parts of the sample. While Raman measurements are quite surface sensitive, the common composition measurement tools like EDX average over almost the whole depth of the films. This difference in probing volume can impede a possible correlation between peak position and elemental composition.

Looking closely at the Raman spectra, one can observe that the main Raman peak is asymmetrically broadened towards lower energies. The influence of a further low intensity mode is the first explanation for this broadening that comes to mind. But, as discussed in the following, through fitting many different spectra the best fit was achieved using a broadened Lorentzian. It should be noted that two different broadened lorentzian shapes are used in this work. Both fit the main mode better than the pure Lorentizan in the main part of the peak. They differ in the tail part which does not affect the following argumentation, which would still stand with the peak shape

used in section 4.3. On the other side of the broadening, after decaying to 0 the fit curve used here goes up again leading to some background at around 250 cm^{-1} which is outside the energy range fitted in this section.

The following function for the broadened lorentzian is used here as it is simpler. It is of the form [108, 109]:

$$I(\omega) = \frac{I_0}{1 + 4 \cdot \left(\frac{\omega_x}{F}\right)^2} \tag{4.1}$$

$$\omega_x = \frac{\omega - \omega_0}{1 - \alpha \left(\frac{\omega - \omega_0}{F}\right)} \tag{4.2}$$

where ω_0 is the peak position, I_0 is the peak intensity, F is the FWHM and α is the broadening parameter responsible for the asymmetry. The best fit of the spectra shown in figures 4.2 and 4.3a was achieved with ω_o= 195.5 cm^{-1}; $\alpha = 0.26 \pm 0.02$ and F=4.3±0.02cm^{-1}.

The fit quality does not improve using two Lorentzians. The two Lorentzian fit depicted in figure 4.3b results in a positive residual on the low energy side of the main mode and a negative one on the other side. The fits of the lower intensity modes are also of lower quality compared to the fit shown in figure 4.3a. The fitted mode at 170 cm^{-1} has to be broader to fit the energy range 180 cm^{-1} to 185 cm^{-1}.

This shows that adding a second Lorentzian is not sufficient to fit the asymmetry of the peak as opposed to the asymmetric peak shape that fits the measured data very well. The asymmetric peak shape not only has less fit parameters than two Lorentzians but also shows better fit results. Therefore asymmetric is the favored shape for fitting this mode. The origin of this asymmetry is discussed in the next section.

In some of the samples prepared in a similar way (see figures 4.5 and 4.6) we do see a contribution of a further mode at 190 cm^{-1} albeit a low contribution. This mode is always around 190 cm^{-1} and does not explain the broadening of the main mode. Because the occurrence of the peak at 190 cm^{-1} can be clearly discerned, as discussed in the following, the peak shape in those samples where the extra mode does not occur (like the one in figure 4.3) is clearly due to broadening and not due to a second line.

The main mode shape and whether the contributions of the extra mode is always present is discussed in the next part, where the main mode is fitted with either one asymmetric or two Lorentzian peaks. Figure 4.4 shows the best fit of the main Raman mode of CZTSe with only the asymmetrically broadened Lorentzian (equation 4.1). For this fit only those parts of the spectrum are used where the contribution of the main CZTSe mode is dominant:

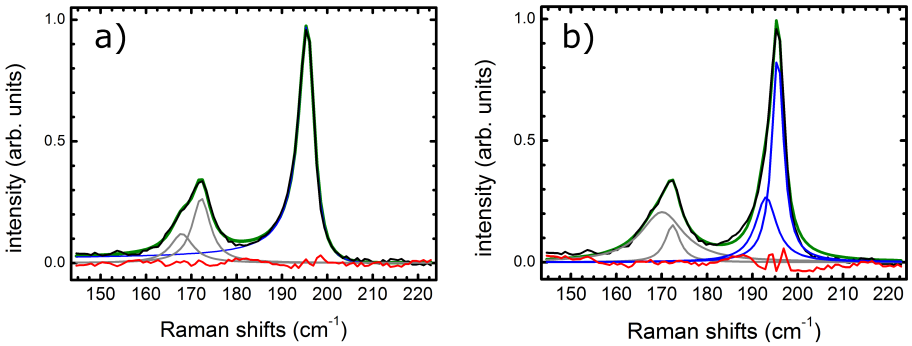

Figure 4.3: Micro Raman spectrum of CZTSe restricted to the spectral area of 145-220 cm^{-1} (black). The main mode at 195 cm^{-1} is fitted with an asymmetrically broadened Lorentzian (a) (blue) or two Lorentzians (b) (blue). The residual is plotted red. The other modes at 168, 172 cm^{-1} are fitted with two Lorentzians (grey line).The green line shows the sum of the fits.

the spectral range where the CZTSe Raman modes of lower intensity are situated is disregarded (marked in gray in figure 4.4) and the spectral range between peaks is used to describe the background. The energy range of the lower intensity Raman modes (208-260 cm^{-1}) is also excluded as they do not contribute to the signal of the main mode (see figure 4.3). The fit process is thereby simplified and only the main mode considered.

As opposed to the fit shown in figure 4.3a, fitting the main Raman mode shown in figure 4.4 does not lead to a satisfactory fit. In fact, the fit shown in thin lines in figure 4.4 shows strong negative and positive residuals. The fit is significantly enhanced when the low energy shoulder of the main mode (marked in blue in figure 4.4) is disregarded when fitting. This is shown in figure 4.4 where this fit and the residuals are shown in thick lines. The fit in the central part of the peak is improved, as seen by the considerably smaller residual. The positive residual that peaks at around 190 cm^{-1} in this case is in fact a further Raman signal which is attributed to a separate phase. This way of fitting the main mode compared to the classical way of adding a further mode has the advantage of having less fit parameters which leads to a more reliable fit.

Only a few different samples were fitted in the manner described above where no correlation with the composition could be found. This lack of correlation of the 190 cm^{-1} contribution with the composition was also seen in the depth dependent measurements. This extra contribution was generally found in half the samples. For the depth dependent study it was found in absorber samples that gave 2 % and 4 % conversion efficiency on the finished

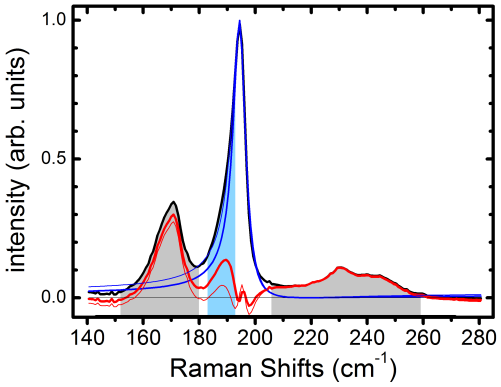

Figure 4.4: Raman spectrum of CZTSe restricted to the spectral area of 140-280 cm^{-1}. The main mode is fitted with an asymmetrically broadened Lorentzian peak shape. The thin lines show the fit (blue) and residuals (red) of the data excluding the low intensity CZTSe peaks marked in gray. The thick lines show the fits and residuals where the low energy shoulder of the main mode (marked in blue) is disregarded in addition to the energy ranges marked in gray.

solar cells though it was not observed on two other samples with 4 % and 6 % efficiencies.

This extra mode can not be clearly attributed to a phase when compared with the literature values of secondary phases. In literature it is tentatively attributed to a different polymorph or to the disordered phase [49, 110]) or a new phase like the phases seen by T. Schwarz et. al. in [100]. It could also be related to a secondary phase such as a so far not characterized polymorph of CTSe.

Some more Raman modes are attributed to CZTSe, which are only clearly seen on epitaxially grown samples in polarization dependent measurements. These modes at 158 cm^{-1} and 215 cm^{-1} will be discussed in detail in section 4.3.

4.2 Phonon confinement of the main mode

The observed asymmetric broadening of the main CZTSe Raman peak can be explained by effects that lead to a shift of the Raman mode energies that are asymmetrically distributed in the probing volume. These include an inhomogeneous laser heating, a distribution of defects, a strain distribution, composition gradients and small crystallites (nano). It can also be explained

by the confinement of the phonons to a smaller volume caused by lattice defects or small crystallites. This section deals with the possible explanations for this broadening of the main mode. More details can be found in section 1.2.7.

Since the main Raman mode shifts with temperature [111], a temperature gradient would be expected to lead to a broadened peak shape. The assumption of a temperature gradient in the probing volume of the laser spot means that we have a low heat dissipation i.e. the middle of the laser spot would be hotter.

The temperature related effects are studied in the following to be able to estimate the temperature difference due to different excitation laser powers. Differences in sample temperature result in peak shifting and asymmetric broadening of the main Raman mode [111]. This can be seen in figure 4.5 where the same spot on the absorber was measured at 10 K and at 300 K. Increasing the temperature of the sample results in an expected broadening and a red shifting of the Raman modes. This is in accordance with the findings on CZTS samples by Sarswat et. al. [111].

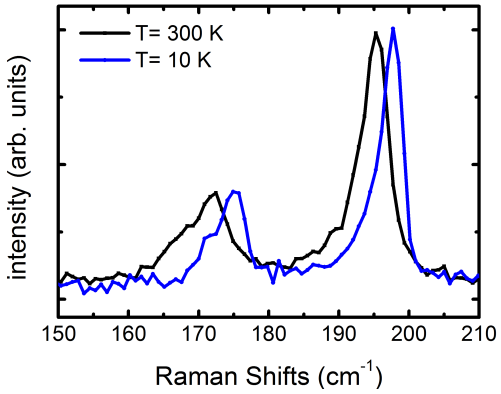

Figure 4.5: Two micro Raman spectra of CZTSe restricted to the spectral area of 150-210 cm^{-1}. Both measurements were taken at the same spot at different temperatures (black curve: 300 K; blue curve: 10 K).

Changing the laser power should lead to a different heat distribution in the laser spot which would lead to a difference in asymmetry of the Raman modes. This was experimentally tested: figure 4.6 shows μRaman spectra taken at the same spot on the CZTSe with laser powers of 0.5 mW and 2.5 mW. A lower laser power of 0.2 mW was also tested with the same result (but with a significantly lower signal to noise ratio) that no difference in

asymmetry, FWHM, or peak position can be observed.

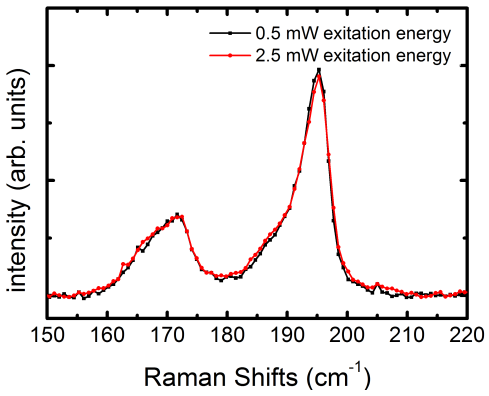

Figure 4.6: Normalized micro Raman spectra of CZTSe restricted to the spectral area of 150-220 cm^{-1}. Both measurements were taken at the same spot with different excitation laser powers (black curve: 0.5 mW/micro spot; red curve: 2.5 mW/micro spot).

The temperature related shifting can be used to estimate the temperature increase due to the excitation laser irradiation. Assuming a linear dependence of the energy of the main mode as a function of the temperature, an upper limit for the temperature increase of the probed volumes for the different laser powers (0.5 mW and 2.5 mW) can be estimated to be at most 30 K. This estimation is done by comparing the peak shift due to heating the sample when applying different excitation laser powers to the peak shift resulting from changing the sample temperature between two known temperatures. Since no peak shift and no broadening of the spectra is measured at room temperature for the different laser powers, the uncertainty of the fit of the peaks position (in figure 4.6) of 0.2 cm^{-1} is used as an estimation for the peak shift. This low estimated value for sample heating (when the excitation laser power is augmented from 0.2 mW to 2.5 mW) leads to the conclusion that the sample's thermal conductivity is high enough to dissipate the power deposited by the excitation laser. Therefore one can conclude that in-homogeneous laser heating effects do not play a role in the asymmetrical broadening of our spectra.

The effects discussed next are based on the properties of the crystal. These are asymmetric distributions of strain, defects and composition in the probing volume. These effects are discussed based on a depth dependent Raman study where three samples are measured in different depths (the preparation of the craters is introduced in section 2.4). The main modes of

CZTSe are fitted with an asymmetric Raman peak shape (the fitting was made as discussed in the previous section).

Strain can also lead to a shift of the Raman mode positions. A gradient in strain in the probed volume could lead to asymmetric peaks. To quantify the effect of strain, measurements of both the bulk of the absorber and its back are compared. The backside of the absorber (i. e. the interface Mo/CZTSe) is revealed by removing it from the substrate. This is done by glueing the absorber to a glass slide which is then mechanically removed exposing the back-side of the absorber. A red shifting in the energy of the modes is observed when the film is mechanically removed compared to all other depths. This can be seen in figure 4.7a where the main mode energies are shown as a function of the normalized depth. The back of the mechanically removed sample is set to the normalized depth of 1 (marked with a gray box). This shifting of the main mode energies is attributed to a strain release. Strain is built up during growth due to mismatches between lattice constants and expansion coefficients of the substrate and the deposited layers. The removal of the layer from the substrate could release strain by removing the constraint given by the substrate, therefore the observed shift could be tentatively attributed to strain release. To know if the asymmetry of the main mode can be attributed to a strain distribution one can compare the asymmetry of the top of the absorber with the removed back. Less asymmetry is expected if strain is released and if strain would play a significant role in the broadening of Raman modes. The fitted asymmetry value is comparable (within the errors of the fitting) for both measurements with slightly higher values for the back of the sample (see figure 4.7b). Thus, in-homogeneous strain can be disregarded as a reason for the asymmetric broadening in our samples.

An asymmetric distribution of defects in the scattering volume is possible and cannot be excluded. However, the similar asymmetry values observed from spectra measured at different depths strongly suggest that this is not the origin of the observed asymmetry of the main Raman peak (see figure 4.7b).

Changes in composition lead to a shifting of the modes while a gradient of composition within the probing volume could also lead to an asymmetric broadening. Composition dependent shifting in peak position was only seen in the pentanary system with varying S/Se content [112]. This does not apply here since the presented samples are pure CZTSe. Additionally, as discussed earlier, no clear correlation was seen between the composition and the main modes peak positions for different samples of different compositions. Another indication that the composition does not play the main role in the asymmetry of the main mode is that no correlation between the composition and the asymmetry of the main mode is seen in the depth dependent study. This is discussed in the following.

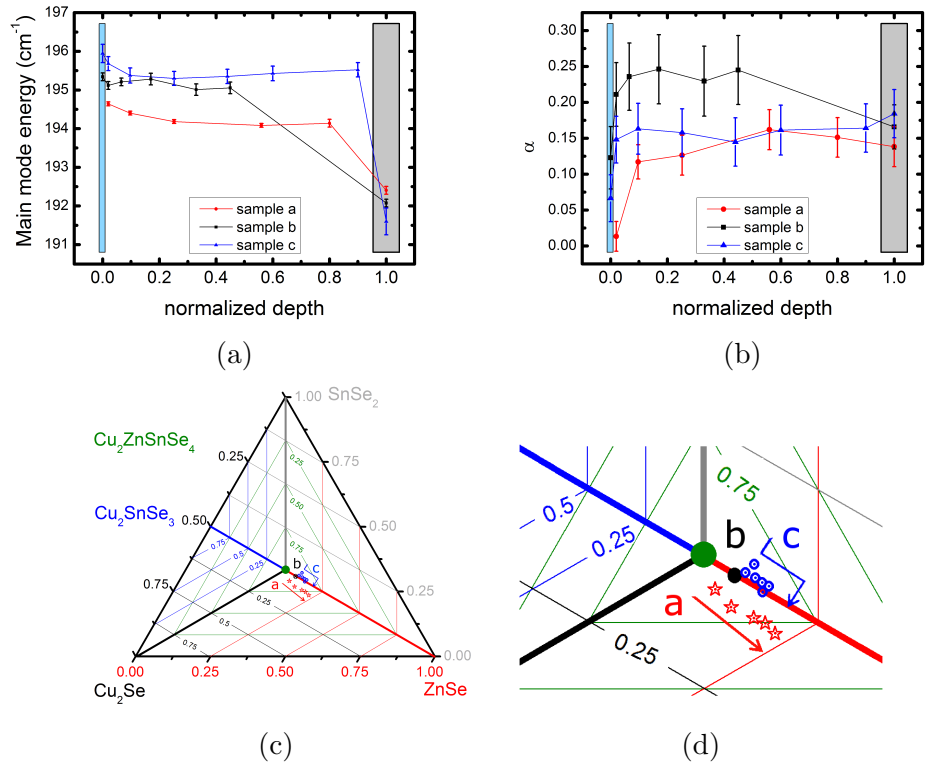

Figure 4.7: Depth dependent study correlating the fitted energy of the main Raman mode (figure a) and its asymmetric broadening (figure b) to the compositions plotted in the ternary phase diagram (figures c and d). The top of the absorber and its mechanically removed back are marked blue and gray in figures a and b. The composition of the latter depths are not shown in figures c and d. Figure d shows a zoom of the central part of the phase diagram. The arrows in figure c and d indicate growing depth in the absorber.

Figures 4.7c and d show the composition at the depths where the Raman spectra were measured. This depth dependent composition is deduced by SIMS measurements that are calibrated by the elemental composition and by the depth dependent X-ray generation (the SIMS calibration is discussed in section 2.3). It should be noted that in figure 4.7c and d the compositions corresponding to the top and back of the sample are not plotted (marked in blue and gray, respectively, in figures 4.7a and b) since these are where the SIMS measurement showed the strongest artifacts.

The changes in composition can be disregarded as origin of the asymmetric broadening of the main mode since the asymmetry anti-correlates with the homogeneity of the composition within the samples. The asymmetries

are decreasing within the samples in the order: sample b, then sample c, then a while the composition of the samples spreads over increasingly bigger areas in the phase diagram reflecting stronger changes in the composition.

Applying the phonon confinement model (PCM) (as introduced in section 1.2.7) to the calculated phonon dispersion by Gürel et. al. [41] shown in figure 4.8, one can predict an asymmetry of the main Raman mode towards lower energies which is in accordance with our experimental findings. In fact, the calculated density of states around the Γ point for the highest energy A modes for both kesterite and stannite show an asymmetry towards low energies [41]. The description of the phonon dispersion relations is repeated from section 1.2.7. For the stannite, the phonon dispersion relation of the A_1 mode has a local maximum at the Γ point. For the kesterite the dispersion relation of the A mode of the highest energy is a bit more complicated: it has a maximum at the Γ point going from Γ to X, P and N, with a minimum at the Γ point going to Z. At first glance, a saddle point seems contradictory to prior statements; this is not the case since the slope of the decreasing phonon energies (Γ to X or P) is higher than the slope of the increasing phonon energies (from Γ to Z). In addition, the maxima of the phonon dispersion of the higher energy A_1 CZTSe mode count double due to the symmetry of the Brilloin zone (see figure 4.8c).

The A modes of lower energy for kesterite (two A modes) and stannite (the A1 mode) exhibit the opposite phonon dispersion behavior around the Γ point i. e. a minimum at the Γ point. This would lead to an asymmetry towards higher energies. However, the overlap between the two peaks in the $170\,\mathrm{cm}^{-1}$ region make a fit with the broadened Lorentzian unreliable: the errors of the fitting parameters like FWHM, position and broadening of the 2 Lorentzian fits are high. Especially the broadening parameter varies from large positive to large negative values making the fitted values unreliable. This means that a further confirmation for the phonon confinement model is not seen in the lower energy A modes. Nevertheless, the asymmetry of the main mode agrees perfectly with the asymmetry of the phonon density around the zone center and is thus a strong support for the assignment of this asymmetry to phonon confinement.

In summary, the main Raman peak is asymmetrically broadened to lower energies. This is attributed to the confinement of the phonons because of the presence of lattice defects in the scattering volume. Other effects that could lead to such broadening can be excluded from playing a major role.

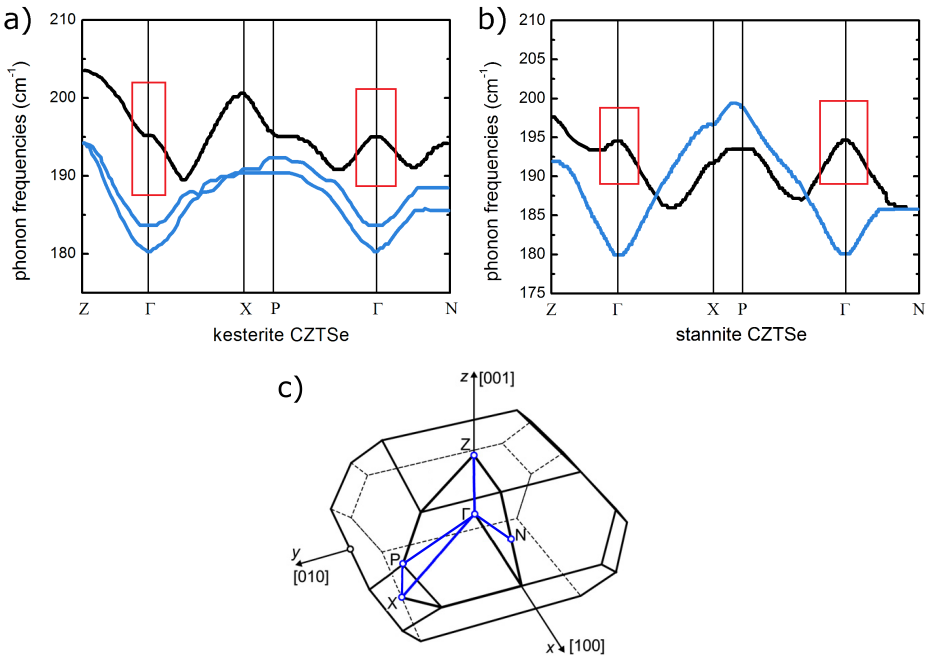

Figure 4.8: Phonon dispersion of the Raman active A modes of kesterite (figure a) and stannite (figure b) CZTSe calculated by DFT by Gürel et. al. and digitized from [41]. The main mode is plotted in black. The red rectangles highlight the phonon dispersion of the main modes around the Γ point. Figure c depicts the first Brillouin zone of a body centered tetragonal lattice, the high symmetry points discussed in figures a and b are marked along with the direction in real space. The phonon is depicted for the blue paths. Figure c is adapted from [42].

4.3 Symmetry of the Raman modes

The attribution of the modes to their symmetry can help in assigning the Raman spectrum to a specific CZTSe polymorph. This is possible since the polymorphs have different space groups leading to a varying number of Raman active phonon modes for the different symmetries. These differences in the irreducible representations of the lattice vibrations of the different polymorphs are discussed in section 1.2.4. Polarization orientation (P/O-Raman) dependent measurements on epitaxial thin films are used to elucidate the symmetries of the Raman modes of CZTSe.

4.3.1 The polarization orientation experiment

The epitaxial CZTSe samples are grown on GaAs (001) wafers and are therefore oriented with respect to the GaAs substrates, where three orientations are technically possible as is schematized in figure 4.9.

These three arrangements of the CZTSe unit cell are discussed depending on the orientation of the main symmetry axis relative to the phonon wavevector $\vec{q}$ (i. e. the orientation of the c axis relative to the excitation direction (z axis)).

The CZTSe lattice can fit on the substrate lattice either with its c axis pointing out-of-plane and its a axes aligned with the GaAs a axis (in the following referred to as 'out-of-plane'), or with the c axis oriented along one a axis of the substrate (in the following referred to as 'in-plane'). For the in-plane configuration the c axis can be oriented parallel to the x or y axis.

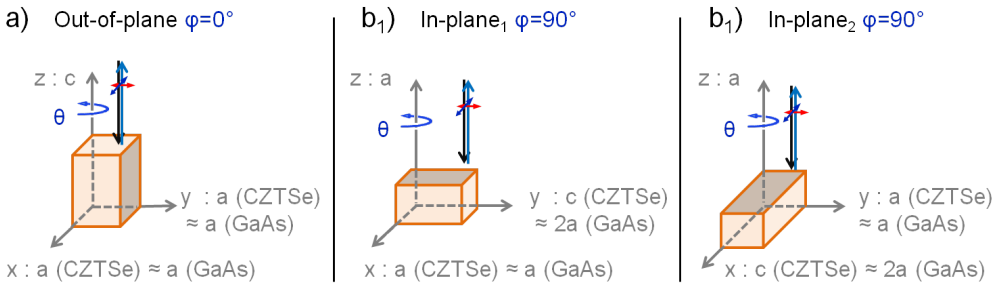

Figure 4.9: The possible orientations of the c axis of CZTSe on the GaAs substrate: a) $c \parallel z$: out-of-plane, and b) $c \perp z$: in-plane. Both in-plane orientations $c \parallel y$ and $c \parallel x$ are shown in figures b_1 and b_2, respectively.

Both configurations are possible as the lattice parameter coefficient of CZTSe (kesterite or stannite) c/a is close to two and $c/2$ and a are compa-

rable to the lattice parameters of the GaAs substrate. The lattice-mismatch between CZTSe ($a = 5.695\,\text{Å}$; $c/2 = 5.673\,\text{Å}$ [92] and GaAs (5.653 Å; ICDD 00-014-0450), is about $\approx 0.8\,\%$ for the 'out-of-plane' and around $\approx 0.3\,\%$ for the 'in-plane' orientation of CZTSe on GaAs. These two configurations can be differentiated using P/O-Raman measurements, see following section.

The P/O-Raman experiment, introduced in section 1.2.5, is simulated for the parallel [$\bar{z}$(x,x)z] and the perpendicular [$\bar{z}$(x,y)z] polarization configurations for our epitaxial layers rotated around the z axis by the azimuth angle θ.

The intensity of the Raman signal for the parallel ($\parallel$) and perpendicular ($\perp$) polarization configurations is given by:

$$I(\theta,\phi)_{\parallel\,/\,\perp} \propto \left|\hat{e}_x \cdot Q^T_{(\theta)} \cdot Q^T_{(\phi)} \cdot R \cdot Q_{(\phi)} \cdot Q_{(\theta)} \cdot \hat{e}_{x/y}\right|^2. \tag{4.3}$$

where R is the Raman tensor, $\hat{e}_x$ and $\hat{e}_{x/y}$ are the incident and scattered light with polarizations in direction of the axes x or y. Q is the rotation matrix. ϕ is set $= 0°$ to simulate the out-of-plane configuration, the in-plane configuration is simulated with $\phi = 90°$ (which is a rotation around the x axis revolving the z axis onto the y axis: in-plane$_1$).

An example of the simulation result is shown in figure 4.10. The signal intensities of the A modes in the out-of-plane configuration is expected to be independent of the rotation around the azimuth angle θ. It is also expected to vanish for the perpendicular polarization configuration.

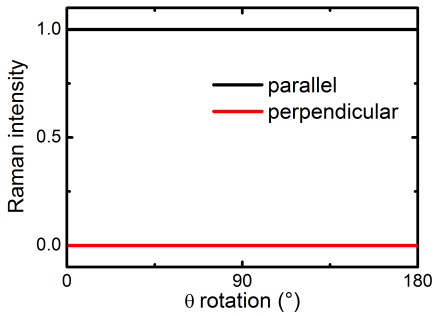

Figure 4.10: Simulated rotation dependent Raman signal intensity evolution for an A symmetry mode (kesterite or stannite) growing in the out-of-plane configuration for both polarization configurations: parallel is depicted in black, perpendicular in red.

Since the GaAs substrate cleaves along two straight edges that are perfectly perpendicular to each other [along two high symmetry directions (110)

and $(\bar{1}10)$], the cleavage edges are therefore at known angles i. e. 45° and 135° in the P/O experiment[1].

4.3.2 Simulating the P/O experiment

Some preliminary considerations follow from the Raman tensors of the different possible polymorphs. They are therefore recapitulated before being discussed.

The Raman tensors for the kesterite structure from space group $I\bar{4}$ (S_4^2; No. 82) are [27, 28, 29]:

$$A = \begin{pmatrix} a & 0 & 0 \\ 0 & a & 0 \\ 0 & 0 & b \end{pmatrix};\ B_z = \begin{pmatrix} c & d & 0 \\ d & -c & 0 \\ 0 & 0 & 0 \end{pmatrix};$$
$$E_x = \begin{pmatrix} 0 & 0 & e \\ 0 & 0 & f \\ e & f & 0 \end{pmatrix};\ E_y = \begin{pmatrix} 0 & 0 & f \\ 0 & 0 & -e \\ f & -e & 0 \end{pmatrix}. \tag{4.4}$$

The stannite structure and the disordered kesterite structure are both from space group $I\bar{4}2m$ (D_{2d}^{11}; No. 121) and their Raman tensors have the same Raman tensors as the polymorphs from space groups $P\bar{4}2_1m$ (D_{2d}^{3}; No. 113), and $P\bar{4}2c$ (D_{2d}^{6}; No. 116)which are given by [27, 28, 29]:

$$A_1 = \begin{pmatrix} a & 0 & 0 \\ 0 & a & 0 \\ 0 & 0 & b \end{pmatrix};\ B_1 = \begin{pmatrix} c & 0 & 0 \\ 0 & -c & 0 \\ 0 & 0 & 0 \end{pmatrix};\ B_{2z} = \begin{pmatrix} 0 & d & 0 \\ d & 0 & 0 \\ 0 & 0 & 0 \end{pmatrix};$$
$$E_x = \begin{pmatrix} 0 & 0 & 0 \\ 0 & 0 & e \\ 0 & e & 0 \end{pmatrix};\ E_y = \begin{pmatrix} 0 & 0 & e \\ 0 & 0 & 0 \\ e & 0 & 0 \end{pmatrix}. \tag{4.5}$$

In the following when the stannite structure is discussed, it is implied that the modes from structures of equivalent symmetry behave in the same way in the P/O experiment while their zone center representation might be different.

The zone center phonon representation for kesterite is:

$$\Gamma_{Raman} = 3A \oplus 6B \oplus 6E$$

and for stannite is:

$$\Gamma_{Raman} = 2A_1 \oplus 2B_1 \oplus 4B_2 \oplus 6E.$$

[1] The reasons for the preferred cleavage directions lie in the presence of surface polarities and the distribution of the electron densities. [113]

The first consideration that can be made is how and whether the energetic positions of the polar modes are affected by the P/O experiment for the possible orientations of the CZTSe.

As a result of the momentum conservation, the wavevector $\vec{q}$ is parallel to the direction of incident light since the incident and scattered light directions are parallel in a confocal setup (see figure 4.11). For this experiment the lab coordinate z is chosen parallel to the direction of the incident light. The polarization directions of the modes are indicated for an oriented crystal ($c \parallel$ to z) as indices in the Raman tensor labels (see Raman tensors of kesterite 4.3.2 and stannite 4.3.2). When the crystal is oriented differently, the polarization directions are rotated and therefore need to be expressed in the lab coordinates.

As introduced in section 1.2.6, the interaction of the polar Raman modes with the incident light depends on the orientation of the crystal. The frequencies of the polar modes are dependent on the orientation with respect to the wavevector $\vec{q}$. The effect is largest when the polarization direction is parallel to the wavevector $\vec{q}$ and zero when the latter directions are perpendicular. Since the polarization direction results from a vibration of atoms parallel to this direction and since the wavevector $\vec{q}$ is parallel to the propagation direction of the light, phonon modes in the extreme cases discussed above have the character of a longitudinal optical (LO), or transversal optical (TO) vibration, respectively.

Figure 4.11 shows the possible orientation of the CZTSe unit cell with respect to the lab coordinates and summarizes the character of the vibrations (LO or TO). It shows the expected effect of the different orientations on the B and E symmetry modes. For the B modes in the out-of-plane orientation the polarization and vibration directions are parallel to the wavevector $\vec{q}$. The B modes are therefore LO vibrations as opposed to the B modes in the in-plane configurations where the vibrations are of TO character and therefore have different frequencies. The degeneracy of the E modes is conserved in the out-of-plane configuration (both are TO modes) while it is lifted in both in-plane configurations (either E_x or E_y is a LO mode).

As the A modes all have the same Raman tensor, it is impossible to distinguish kesterite from any other polymorphs by considering the symmetry of the A modes but their total count differs between the space groups and is therefore a tool to differentiate them.

Comparing the Raman tensors of kesterite and stannite, one can see that: depending on the ratio of the Raman tensor parameters c/d, the B mode of kesterite can behave like the B_1 (for $c \gg d$) or B_2 (for $c \ll d$) mode of stannite or as a mixture of the latter cases.

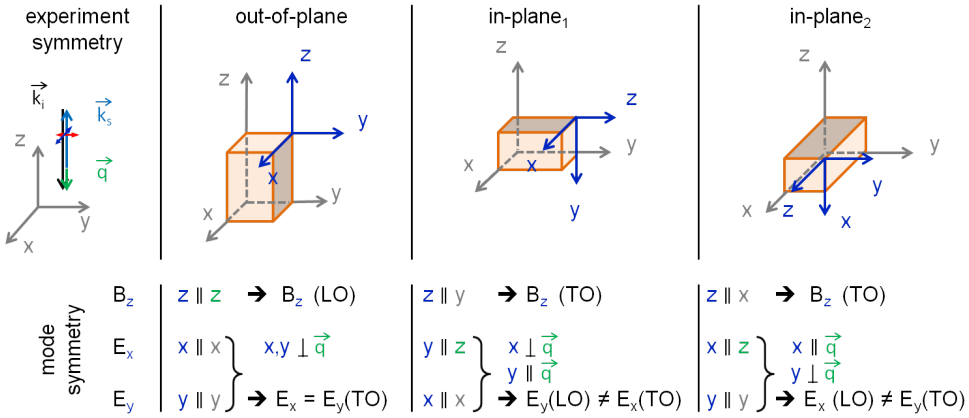

Figure 4.11: Schematic representation of the orientation of the CZTSe unit cell (on the GaAs substrate) with respect to the lab coordinates (shown in gray). The propagation directions of incident ($\vec{k_i}$) and scattered ($\vec{k_s}$) light are shown in black and blue, respectively. The blue and red double arrows show the possible polarization directions of $\vec{k_i}$ and $\vec{k_s}$. The local coordinate system (and its axis) of the unit cell is shown in blue. The wavevector $\vec{q}$ is shown in green. The z axis is shown in green in the lower part of the scheme to show that it is parallel to $\vec{q}$.

The results of the simulation of the P/O experiment i. e. the Raman intensity dependence on the rotation angle for both polarization configurations $I(\theta)_{\parallel/\perp}$ for the different mode symmetries and polymorphs are calculated using equation 4.3.1 and are summarized in table 4.1. The table also shows the Raman tensors of the mode symmetries in both orientations (in-plane and out-of-plane). These results are discussed in the following subsections.

		$\boldsymbol{A_1}=\begin{pmatrix} a & 0 & 0 \\ 0 & a & 0 \\ 0 & 0 & b \end{pmatrix}$	$\boldsymbol{B_1}=\begin{pmatrix} c & 0 & 0 \\ 0 & -c & 0 \\ 0 & 0 & 0 \end{pmatrix}$	$\boldsymbol{B_{2z}}=\begin{pmatrix} 0 & d & 0 \\ d & 0 & 0 \\ 0 & 0 & 0 \end{pmatrix}$	$\boldsymbol{E_x}=\begin{pmatrix} 0 & 0 & 0 \\ 0 & 0 & e \\ 0 & e & 0 \end{pmatrix}$	$\boldsymbol{E_y}=\begin{pmatrix} 0 & 0 & e \\ 0 & 0 & 0 \\ e & 0 & 0 \end{pmatrix}$
out-of-plane	**stan.**					
	$\parallel$ pol.	constant: $\propto a^2$	$c^2\cos^2(2\theta)$	$d^2\sin^2(2\theta)$	0	0
	$\perp$ pol.	0	$c^2\sin^2(2\theta)$	$d^2\cos^2(2\theta)$	0	0
	kest.	$\boldsymbol{A}=\begin{pmatrix} a & 0 & 0 \\ 0 & a & 0 \\ 0 & 0 & b \end{pmatrix}$	$\boldsymbol{B_z}\begin{pmatrix} c & d & 0 \\ d & -c & 0 \\ 0 & 0 & 0 \end{pmatrix}$		$\boldsymbol{E_x}=\begin{pmatrix} 0 & 0 & e \\ 0 & 0 & f \\ e & f & 0 \end{pmatrix}$	$\boldsymbol{E_y}=\begin{pmatrix} 0 & 0 & f \\ 0 & 0 & -e \\ f & -e & 0 \end{pmatrix}$
	$\parallel$ pol.	constant: $\propto a^2$	$(c\cos(2\theta)+d\sin(2\theta))^2$		0	0
	$\perp$ pol.	0	$(d\cos(2\theta)-c\sin(2\theta))^2$		0	0
		$\boldsymbol{A_1}=\begin{pmatrix} a & 0 & 0 \\ 0 & b & 0 \\ 0 & 0 & a \end{pmatrix}$	$\boldsymbol{B_1}=\begin{pmatrix} c & 0 & 0 \\ 0 & 0 & 0 \\ 0 & 0 & -c \end{pmatrix}$	$\boldsymbol{B_{2z}}=\begin{pmatrix} 0 & 0 & -d \\ 0 & 0 & 0 \\ -d & 0 & 0 \end{pmatrix}$	$\boldsymbol{E_x}=\begin{pmatrix} 0 & 0 & 0 \\ 0 & 0 & -e \\ 0 & -e & 0 \end{pmatrix}$	$\boldsymbol{E_y}=\begin{pmatrix} 0 & e & 0 \\ e & 0 & 0 \\ 0 & 0 & 0 \end{pmatrix}$
in-plane$_1$	**stan.**					
	$\parallel$ pol.	$(a\cos^2(\theta)+b\sin^2(\theta))^2$	$c^2cos^4(\theta)$	0	0	$e^2\sin^2(2\theta)$
	$\perp$ pol.	$(a-b)^2\sin^2(2\theta)$	$c^2sin^2(2\theta)$	0	0	$e^2\cos^2(2\theta)$
	kest.	$\boldsymbol{A}=\begin{pmatrix} a & 0 & 0 \\ 0 & b & 0 \\ 0 & 0 & a \end{pmatrix}$	$\boldsymbol{B_z}=\begin{pmatrix} c & 0 & -d \\ 0 & 0 & 0 \\ -d & 0 & -c \end{pmatrix}$		$\boldsymbol{E_x}=\begin{pmatrix} 0 & e & 0 \\ e & 0 & -f \\ 0 & -f & 0 \end{pmatrix}$	$\boldsymbol{E_y}=\begin{pmatrix} 0 & f & 0 \\ f & 0 & e \\ 0 & e & 0 \end{pmatrix}$
	$\parallel$ pol.	$(a\cos^2(\theta)+b\sin^2(\theta))^2$	$c^2cos^4(\theta)$		$e^2\sin^2(2\theta)$	$f^2\sin^2(2\theta)$
	$\perp$ pol.	$(a-b)^2\sin^2(2\theta)$	$c^2sin^2(2\theta)$		$e^2\cos^2(2\theta)$	$f^2\cos^2(2\theta)$

Table 4.1: Simulated P/O experiment: Raman signal intensity dependence on the polarization configuration and orientation of the CZTSe unit cell as a function of the rotation angle θ for the Raman mode symmetries of stannite and kesterite. The Raman tensors are given for all modes in both orientations. The *in-plane*$_1$ orientation is shown (c axis of CZTSe $\parallel$ to the y lab coordinate (as defined in figure 4.11)). Some signal intensity dependencies with multiple occurrences are color coded for a better overview.

The out-of-plane configuration

For a CZTSe crystal oriented out-of-plane, the result of the P/O experiment for the A mode is that it is constant for the parallel polarization while it is zero for the perpendicular polarization configuration (as shown in figure 4.10). The E symmetry modes (E_x and E_y) are zero for both polarization configurations for both the kesterite and stannite structures. The signal intensity of the B modes varies sinusoidally with a period of 90° as a function of the rotation around the azimuth angle θ, see figure 4.12. The calculated θ dependencies of the Raman signal intensities of the B modes for both kesterite and stannite are repeated in table 4.2 from table 4.1.

out-of-plane		B_1	B_2
stannite	$\parallel$ pol. Conf.	$c^2\cos^2(2\theta)$	$d^2\sin^2(2\theta)$
	$\perp$ pol. Conf.	$c^2\sin^2(2\theta)$	$d^2\cos^2(2\theta)$

out-of-plane		B_z
kesterite	$\parallel$ pol. Conf.	$[c\cos(2\theta) + d\sin(2\theta)]^2$
	$\perp$ pol. Conf.	$[-c\sin(2\theta) + d\cos(2\theta)]^2$

Table 4.2: Raman signal intensity evolution $I(\theta)$ for the parallel and perpendicular polarization configurations, for the B modes of the kesterite and stannite structures calculated using equation 4.3.1.

The calculated signal intensities of the B_1 and B_2 modes are phase shifted by half a period so that their signal intensity evolution is *inverted*. The phase shift is observed between the parallel and perpendicular polarization configurations. This means that the symmetry of the B modes (i. e. B_1 or B_2) is identifiable in the considered rotation polarization dependent Raman measurement.

It is convenient to define the results of this PO experiment (i. e. the intensity dependencies $I(\theta)_{\parallel \text{ and } \perp}$)of the B_1 and B_2 modes of stannite as B_1-like and B_2-like (depicted in figures 4.12a and b), respectively, as the same dependencies are seen for other mode symmetries and unit cell orientations.

For the case of kesterite, the signal intensities also have phase shifted intensity dependencies depending on the polarization. However, these shift with the c/d Raman tensor entry ratio as shown in figure 4.12c where $I(\theta)_{\parallel\,/\,\perp}$ is plotted for different c/d ratios. One can see that the intensity dependencies for the modes of the kesterite and stannite structures is the same, only shifted between the extreme cases given by the B_1 and B_2 modes of stannite. Figure 4.12d shows the maximum of the rotation dependent Raman signal intensity ϵ as a function of the c/d ratio. It also confirms that for extreme

values of c/d the B modes of kesterite behave like either B_1-like or B_2-like. This dependency of the angle of maximum intensity on the c/d ratio can be used to determine this ratio from an actual measurement.

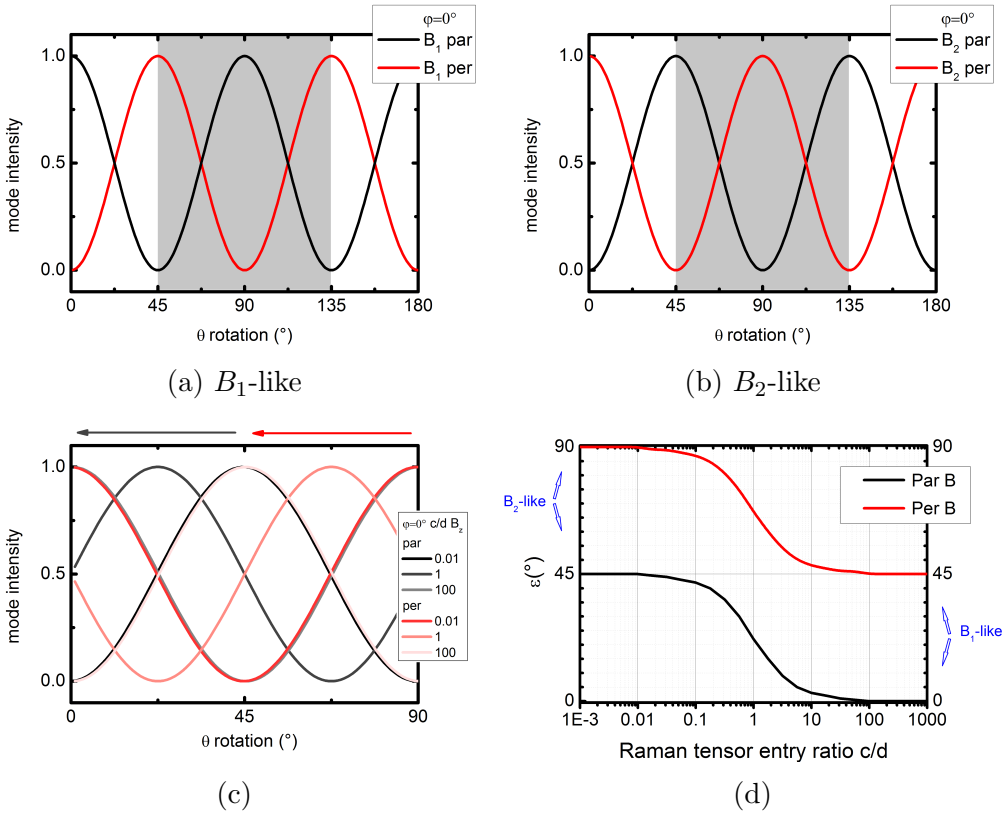

Figure 4.12: Simulation of the rotation dependent Raman signal intensity evolutions for a crystal in the out-of-plane configuration ($\phi = 0°$), for B_1 (figure a), B_2 (figure b), in the parallel (black) and perpendicular (red) polarization configurations, respectively. The rotation range between 45° and 135° is marked in gray. Figure c shows the intensity evolution for the kesterite structure for different c/d ratios; the arrows indicate the shifting of the maximum of signal intensity with growing c/d ratio; black marks the parallel polarization configuration and red the perpendicular one. Figure d depicts ϵ which is the calculated position of the maximum of the rotated Raman signal intensity as a function of the c/d Raman tensor ratio, for the parallel and perpendicular polarization configuration for a kesterite B_z mode in the in-plane configuration (in the 0-90° range).

The in-plane$_1$ configuration

The intensity dependencies are first discussed for the in-plane$_1$ (figure 4.9) orientation of the CZTSe and the other orientation is discussed at the end of the section. The Raman signal intensities as a function of the rotation around the azimuth angle are the same for the A modes of kesterite and stannite. These follow:

$$\begin{aligned} A/A_1 : I(\theta)_{\parallel} &\propto (a\cos^2(\theta) + b\sin^2(\theta))^2 \text{ and} \\ A/A_1 : I(\theta)_{\perp} &\propto (a-b)^2\sin^2(2\theta) \end{aligned} \tag{4.6}$$

The signal intensity is dependent of the a/b ratio for parallel polarization configuration while independent of the Raman tensor entry ratio in the perpendicular configuration. Figure 4.13a shows the Raman signal intensities for both polarization configurations. The parallel polarization configuration is plotted for a ratio $a/b = 0.05$. This a/b ratio is varied over several orders of magnitude in figure 4.13b: one can see that for $a/b < 1$ the maxima of intensity are at 0° and 180° while they are at 90° and 270° (not shown, its is a result of the periodicity) for $a/b > 1$. Figure 4.13b shows that inverting the a/b ratio only leads to a shift of the signal intensity dependencies of θ by half a period. This dependency of a/b can be used to fit this ratio in an actual measurement.

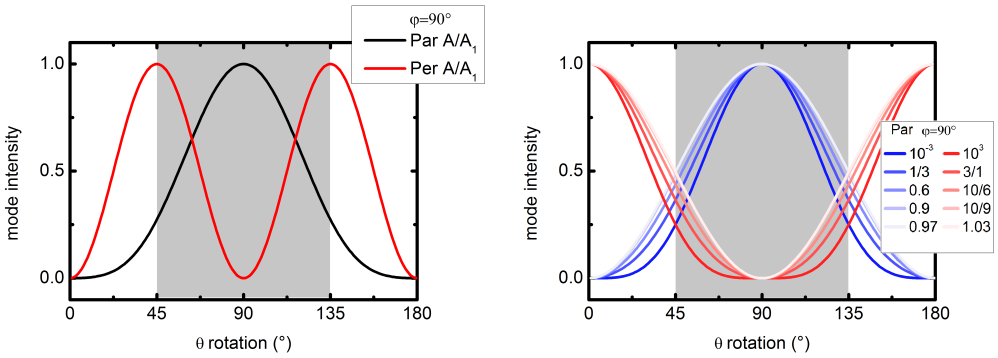

(a) (b)

Figure 4.13: Simulation of the rotation dependent Raman signal intensity evolutions for the in-plane configuration ($\phi = 90°$) for the A modes of CZTSe. Figure a shows the perpendicular polarization configuration (plotted in red, a/b independent) and the parallel polarization configuration (plotted in black) for $a/b = 0.05$. Figure b only shows the parallel polarization configuration for different a/b ratios. The rotation range between 45° and 135° is marked in gray.

The result of the simulation for the B_{2z} mode of the stannite structure is constant at 0 intensity (independent of the θ rotation and polarization configuration). The non zero modes follow:

$$B_1/B_z : I(\theta)_{\parallel} \propto c^2 \cos^4(\theta) \text{ and}$$
$$B_1/B_z : I(\theta)_{\perp} \propto c^2 \sin^2(2\theta)$$

for the parallel and the perpendicular polarization configuration of both the B_1 modes of stannite and B_z modes of kesterite, respectively. The non zero intensity dependencies of the B symmetry modes are plotted in figure 4.14.

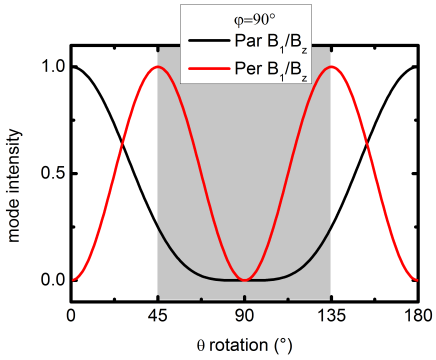

Figure 4.14: Simulation of the rotation dependent Raman signal intensity evolutions for the in-plane configuration ($\phi = 90°$) for the B_1 mode of stannite and the B_z mode of kesterite CZTSe. The rotation range between 45° and 135° is marked in gray.

For the E symmetry modes of stannite structure, the Raman signal intensity dependency (on θ) is zero for the E_x modes (for both polarization configurations) while it is B_2-like for the E_y modes. For the kesterite structure both E_x and E_y symmetry modes are B_2-like. In fact, $I(\theta)_{\parallel}$ for both the E_y mode of the stannite structure and the E_x and E_y modes of the kesterite structure is given by: $I(\theta)_{\parallel} \propto \sin^2(2\theta)$ for the parallel polarization configuration and by: $I(\theta)_{\perp} \propto \cos^2(2\theta)$ for the perpendicular polarization configuration(see figure 4.15).

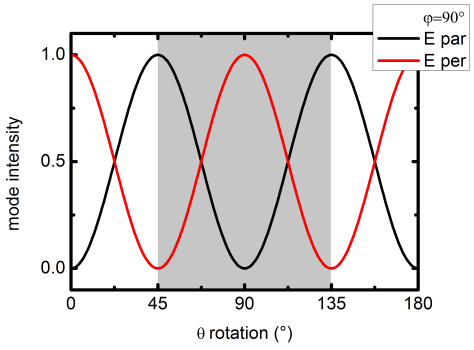

Figure 4.15: Simulation of the rotation dependent Raman signal intensity evolutions for the in-plane configuration ($\phi = 90°$) for the stannite E_y mode and the kesterite E_x and E_y modes of CZTSe. The rotation range between 45° and 135° is marked in gray.

The in-plane$_2$ configuration

The other possible in-plane configuration (*in-plane*$_2$) that can be achieved by rotating the CZTSe around the lab coordinate y axis gives the same result as for the simulation shown above only shifted by 90°. This affects the 180° periodic Raman signal intensity dependencies on the rotation around θ i. e. $I(\theta)_{\parallel}$ of the: A mode (of kesterite and stannite, see figure 4.13) and the B_1 mode of stannite and the B_z of kesterite (see figure 4.14). All other non zero modes of the *in-plane*$_1$ configuration summarized in table 4.1 have 90° periodicity and thus have an unchanged behavior.

That the two in-plane orientations are almost identical and only differ by a 90° shift in θ, reflects the fact that the orientation of the lab coordinate x axis can be chosen parallel to one of the two cleavage edges of the substrate having a 90° angle between them (defining the origin of rotation).

Domains of mixed orientations

Mixed domains of the possible in-plane orientations as well as mixed domains of in-plane/out-of-plane orientations are considered in the following. A mixture of the two possible in-plane orientations does not change the behavior of the E symmetry modes since their rotation dependent Raman intensities only differ by a shift of $\theta = 90°$ which is also their periodicity. The same assessment can be made for the intensity dependencies of the perpendicular polarization configurations of the A and B symmetry modes.

Since the A and B modes have a 180° periodicity when measured in the parallel polarization configuration, the relative content of the two orientations matters.

Figure 4.16 shows the calculated signal intensity dependencies of the non zero B modes (B_z and B_1 for the kesterite and stannite structures, respectively) for different mixes of the in-plane orientations. These dependencies are given by the normalizations of :

$$B_{1/z\ \mathrm{mix}} : I(\theta)_{\parallel} = (100 - x)\cos^4(\theta) + x\ \sin^4(\theta). \tag{4.7}$$

where x is the percentage of the in-plane$_2$ orientation.

This $I(\theta)$ shows two maxima. Depending on which orientation is dominant, the absolute maximum is at 90° or 0° (with a period of 180°) for dominating in-plane$_1$ or in-plane$_2$, respectively. The relative intensity of the local maximum and the position of the minimum also depends on the mixture of orientations. When the relative content of both phases is the same,

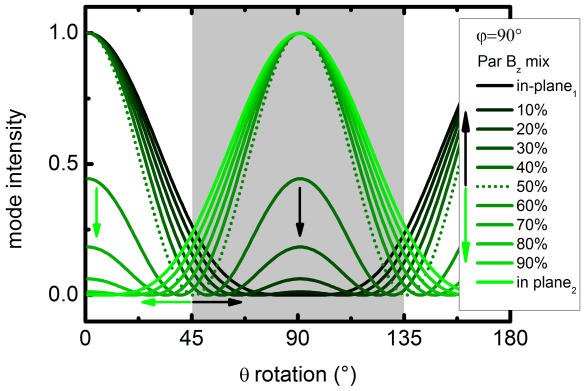

Figure 4.16: Simulation of the effect of domains of mixed in-plane orientation on the rotation dependent Raman signal intensity evolutions for the B symmetry modes of CZTSe. Different mixtures from 100 % in-plane$_1$ to 100 % in-plane$_2$ are depicted. A shift in positions of the absolute minima and change in the intensity of the local maxima are marked by black and green arrows representing growing in-plane$_1$ and in-plane$_2$ contents, respectively. The rotation range between 45° and 135° is marked in gray.

the signal intensity dependence is given by:

$$B_1/B_{z\ (50\%\ mix)} : I(\theta)_{\parallel} \propto \cos^2(2\theta) \quad \text{and,}$$
$$B_1/B_{z\ (50\%\ mix)} : I(\theta)_{\perp} \propto \sin^2(2\theta)$$

which is B_{1-like} making it difficult to differentiate between the B modes of the in-plane and out-of-plane configurations.

As opposed to the above B modes, the A mode behavior in the case of mixed orientations not only depends on the relative content of the two orientations but also on the ratio of the Raman tensor entries (a/b). The extreme cases of $a \ll b$ or $a \gg b$ can be easily considered since they allow the neglect of either the first or the second term in equation 4.6 leading to the same dependency as the parallel polarization configuration of the B modes in the in-plane$_1$ or in-plane$_2$ orientations. Adding the fact that changing the orientation has the same effect as inverting the a/b ratio (i. e. shifting the signal intensity dependency by half a period (see figure 4.13b)), leads to the result that both extreme cases lead to the same result when mixing in-plane orientations (same as in figure 4.16 discussed above).

Figure 4.13b shows that the dependency of $I(\theta)_{A\parallel}$ on the a/b ratio is quite low except in a small range around $a/b = 1$, therefore the above approximation is valid for a large range of a/b.

Mixing the in-plane and out-of-plane orientations for the A modes results in an offset in the parallel polarization configuration of the in-plane orientation by a constant value. This offset is the contribution from the out-of-plane orientation.

For the perpendicular polarization configuration only the contribution of the in-plane orientation is seen: the same behavior as the in-plane orientation is expected for the E modes since their intensity is expected to be zero in the out-of-plane orientation.

Conclusion

The main conclusion of this section is that most configurations i. e. combination of structures and orientation, can be differentiated, if present as a single phase in the probing volume, and if all the expected (non zero) dependencies are identified in the experiment:

- Comparing the in-plane and out-of-plane configurations shows that it is possible to distinguish these two orientations since the A and B modes have quite different Raman signals dependencies.
- A spectrum can be assigned to the kesterite structure oriented out-of-plane when the B modes present a clear shift from the expected maxima and minima of the B_1-like and B_2-like dependencies.
- A spectrum can be assigned to the stannite structure oriented out-of-plane when both B_1-like and B_2-like dependencies are measured.
- Only in the in-plane configuration can kesterite and stannite not be identified by the consideration of the symmetries present in the spectrum since no difference in the signal dependencies is expected (see table 4.1). However, the different polymorphs have different irreducible representations, so that the total count of modes of the different symmetries provides a way to identify the structure in the in-plane orientation.

Also mixed orientations, especially an in-plane / out-of-plane mixture should be easily confirmed in the PO experiment since it is detectable in the dependencies of the A modes which are the modes of highest intensity (in CZTSe).

4.3.3 Results of the P/O experiment

The fitting results

The results of the angle and polarization dependent Raman measurements on epitaxially grown samples are shown in figures 4.18 and 4.19 where the fitted peak intensities are plotted as a function of the polarization configuration and the rotation angle θ.

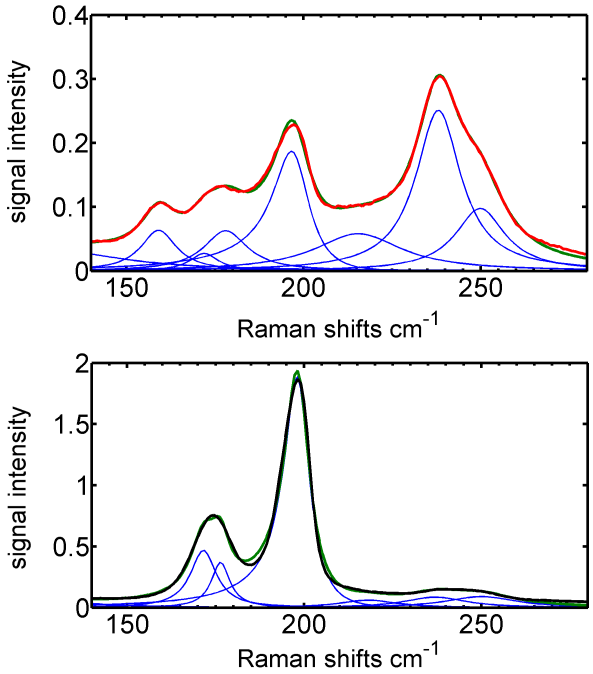

Figure 4.17: Raman spectra measured in perpendicular (figure a; plotted in red) and parallel polarization configurations (figure b; plotted in black) rotated around θ by 105°. All peaks are fitted with Lorentzian peak shapes (except for the main one at 196 cm^{-1} which is fitted with an asymmetrically broadened Lorentzian). The fitted peaks are depicted in blue and the sum of the fitting peaks is depicted in green.

All the modes are fitted with Lorentzian peaks except for the main mode (at 196 cm^{-1}) which is fitted with an asymmetrically broadened Lorentzian peak shape as discussed in section 4.1. A different formula for the asymmetric

Lorentz shape is used since it fits the full energy range [109]:

$$I = \frac{A}{\gamma} \cdot \frac{1}{1 + 4 \cdot ((x - x_0)/\gamma)^2}$$
$$\gamma = \frac{2 \cdot F}{1 + \exp(\alpha \cdot [x - x_o])}$$

where F is the unbroadened FWHM, A the amplitude, x_0 the peak position and α the broadening parameter.

All spectra were fitted with parameters that were allowed to vary in limited ranges, except for the broadening parameter α of the main mode which was varied manually to optimize the fit. The quality of the fit was judged by two criteria: that the fitting function does not reach higher values than the measured signal (i. e. lowest possible negative residual), and that the fit parameters do not reach the fixed limits. An example for a satisfactory fit for both polarization configurations is shown in figure 4.17 which was chosen since it has a high signal in the perpendicular polarization configuration and one can clearly see the contribution of the different modes in the spectrum.

The peak positions and FWHM are summarized along with their standard deviations in table 4.3. The best fit was achieved for peaks at (128, 159, 172, 177, 196, 217, 237 and 250) cm^{-1}.

position	σ	FWHM	σ	α
127.6	1.6	40.6	5.5	-
159.2	1.4	12.2	4*	-
171.8	0.6	10.0	1.5	-
176.9	0.9	10.3	4.2	-
196.4	0.9	11.6	2.4	0.09
217.2	1.2	23.1	3.6	-
237.4	0.4	18.9	2.9	-
249.6	0.5	22.9	2.8	-

Table 4.3: Average fitted peak energies and FWHM's, their standard deviation σ (in cm^{-1}) and the broadening parameter α of the main mode for the P/O Raman measurements on epitaxial CZTSe. The * marks values where two out-liners were neglected in the calculation.

The first result is that the peak positions fitted here differ slightly from the ones summarized in section 4.1. This can be due to differences in strain or composition but also to the fact that more peaks are used for the fit: the

peaks at 159 and 217 cm^{-1} influence the fitting result for the main modes (i. e. the A symmetry modes). These latter peaks (at 159 cm^{-1} and 217 cm^{-1}) were not fitted on the polycrystalline samples thereby changing the resulting peak positions.

As opposed to the theoretical prediction of an oriented material of one crystal structure, the peak intensities do not vanish for any polarization configuration or rotation angle θ (figures 4.19 and 4.18). This can be due to domains of different orientations or polymorphs. It can also be due to a background in the measurement ranging from scattering in the spectrograph over second order Raman modes to some luminescent recombination in the sample. The non-zero behavior of the modes can additionally be an artifact of the fit reflecting the difficulty to achieve a perfect fit while trying to leave the fit parameters as free as possible. Another explanation can be imperfections in the measurement (i. e the incident light beam is not perfectly parallel to the z axis since it is focused on the sample by a microscope lens [114]). This last effect is minimized by illuminating the microscope lens with a narrow laser beam minimizing the aperture.

The *A* symmetry modes

The P/O-Raman results for the modes fitted at (172, 177, 196) cm^{-1} are plotted in figure 4.18. These modes can be attributed to the A symmetry since they, on the one hand, are at frequencies that agree with the theoretical mode energy calculations (summarized in section 1.2.8), and on the other hand, their fitted intensities as a function of the rotation by θ (shown in figure 4.18) strongly resemble the expected behavior for A modes in the out-of-plane orientation (shown in figure 4.10).

Figure 4.18 shows that the signal intensity has a maximum in the parallel configuration at $\theta \approx 90°$.

This deviation from the ideal out-of-plane A symmetry peak intensity evolution can be explained by different effects such as a mixture of out-of-plane and in-plane orientations, the contribution of a further mode and fitting artifacts, as discussed in the following.

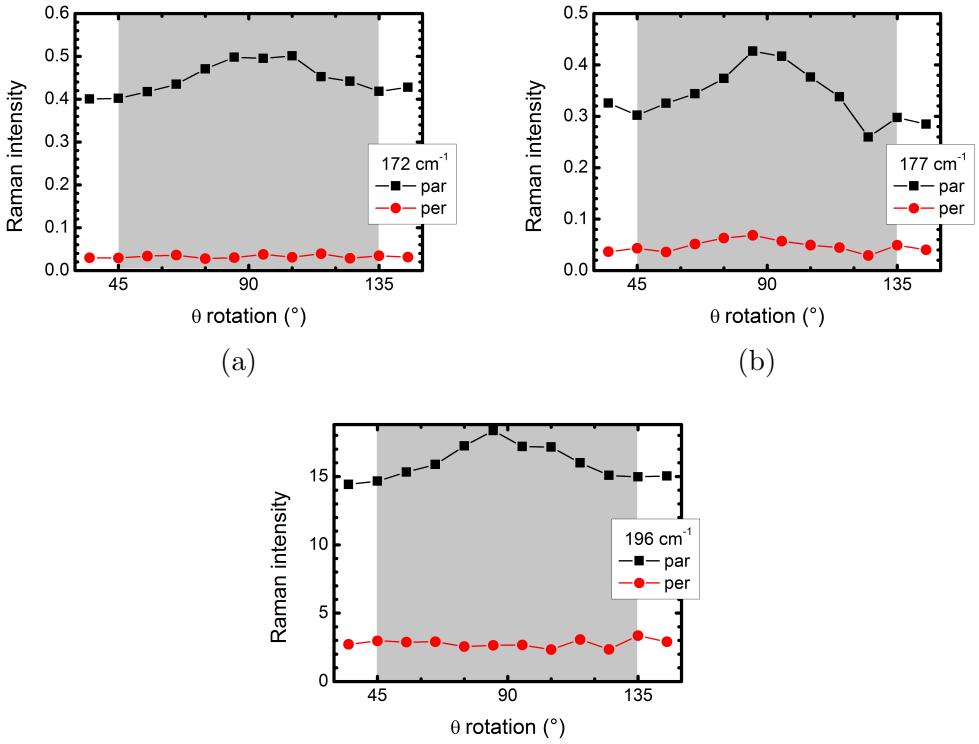

Figure 4.18: Intensity of the Raman modes depending on the polarization configuration (parallel plotted in black, perpendicular plotted in red) and on the rotation of the sample around the z axis by the angle θ (defined in figure 4.9). Figures a to c show the fitted intensity dependencies of the peaks at (172, 177, 196) cm^{-1}, respectively. The rotation range between 45° and 135° is marked in gray.

A mixture of in-plane and out-of-plane orientation is a possible explanation but the measured θ rotation range is not sufficient for a definitive attribution.

Assuming the spectrum is dominated by the out-of plane orientation, the contribution of a further mode can be considered as a reason for the maximum of intensity at $\theta = 90°$. An attempt was therefore made to fit the main mode with an extra contribution but the fit was unstable (i. e. not fulfilling the fit criteria discussed above). An alternative fitting method was tested to determine if a further contribution can be clearly seen. For this, only the main mode is fitted with a Lorentzian and the peak position is plotted as a function of θ. Assuming the ideal constant intensity evolution of out-of-plane A symmetry and the presence of an extra contribution with a mode

energy close to the latter mode, the energetic position of the sum of those modes would shift in the same way as the intensity evolution of the extra contribution would do as a function of θ. This was tested on the main mode but the fitted position of this mode does not follow a trend. Therefore an extra mode is not detected by this method. Assuming an extra mode would be present in the energy range of the main mode then it would be B_1-like (with a maximum at 90° in the parallel polarization configuration, assuming an out-of-plane orientation). According to theoretical calculations of Gürel et. al. [41] and Amiri et. al. [48], the B_1 symmetry modes of the stannite structure are either at energies lower than $100\,\mathrm{cm}^{-1}$ or higher than the main mode by 20-30 cm^{-1} , therefore this assumed extra B_1-like mode can only originate from a kesterite B_z mode with the corresponding c/d ratio (i.e. $c \gg d$) still assuming a dominating out-of-plane orientation.

One has to also take into account that for the main mode the difference between the lowest and highest signal intensities of the parallel polarization configuration is orders of magnitude higher than the signal intensities of the other modes later attributed to the B symmetry (shown in figure 4.19). Addiotionally another argument against the attribution of this maximum of intensity to an extra mode is that it occurs in the signal intensity dependencies of all the modes that are attributed to A symmetry which is improbable (figure 4.18).

Fitting artifacts cannot play a role in the main mode since it has a very high signal intensity compared to the other modes limiting their effect on the fitted intensity.

To summarize this last part: there is no clear indication that the deviation of the modes of A symmetry from the ideal case is due to an extra contribution.

The mode energy range 160-170 cm^{-1} is fitted with two Lorentzians. This energy range can also be fitted with only one Lorentzian just slightly lowering the fit quality. In other words fitting this measurement is not conclusive as to the number of A symmetry modes (two or three) which would have lead to an assignment to kesterite or stannite. It should also be noted that changing the number of modes in this range does not change the overall behavior of the other modes and consequently it does not change any other symmetry assignment.

Higher resolution measurements on the same sample show that the latter energy range is in fact composed of two A modes supporting the choice of fitting the spectra (in the 160-170 cm^{-1} energy range) as discussed above with two A modes.

The B symmetry modes

The measured P/O-Raman intensity evolutions of the modes at (159, 217, 237 and 250) cm^{-1} are fitted using $I(\theta) = x_1 + x_2 * \sin^2(2\theta + x_3)$ and plotted in figure 4.19. x_1 and x_3 are the parameters needed to shift the measured signals in intensity and in θ, respectively, while x_2 changes the amplitude of the signal. It should be noted that for this fit the periodicity is fixed to 90°.

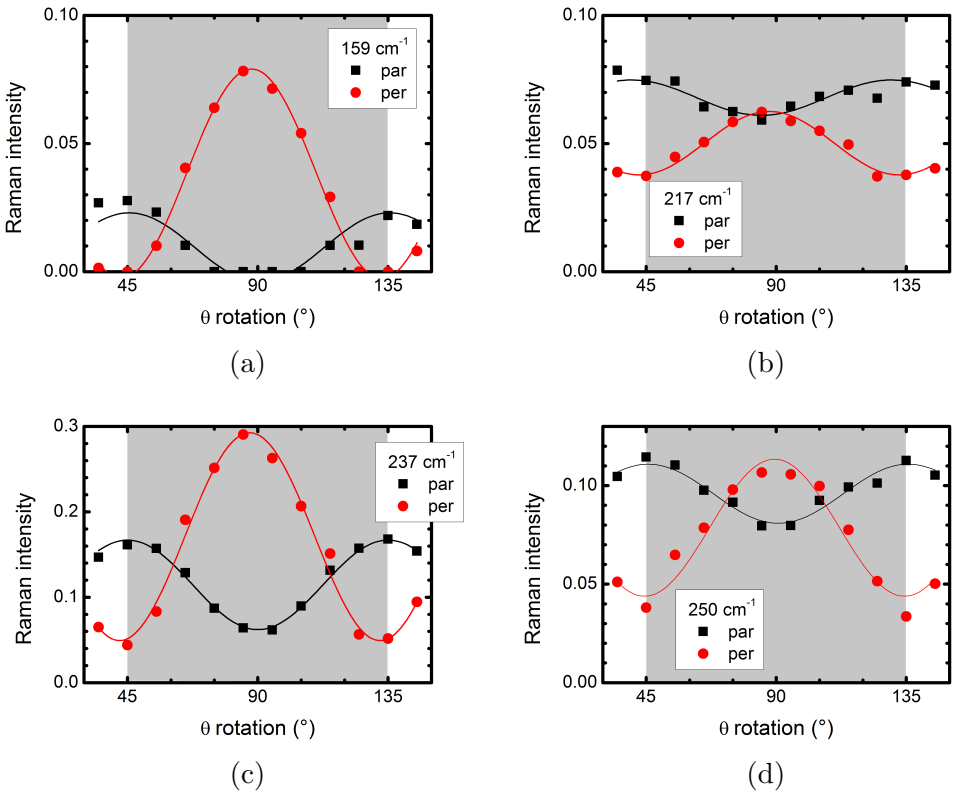

Figure 4.19: Fitted intensity of the Raman modes depending on the polarization configuration and rotation of the sample around the z axis as defined in figure 4.9 for the modes at (159, 217, 237 and 250) cm^{-1}, shown in figures a to d, respectively. The rotation range between 45° and 135° is marked in gray.

These modes at (159, 217, 237 and 250) cm^{-1} seem to follow a B_2-like behavior. However, the maxima of the Raman intensity in the perpendicular polarization (and minima of the parallel polarization) configuration are fitted at rotation angles lower than $\theta = 90°$. Since the fit does not consider any errors which were made in the initial fit of the Raman spectra used to get the intensity dependencies fitted in figure 4.19, one has to be careful with the

interpretation. The modes can therefore either be attributed to B_2 symmetry modes of the stannite structure or to B_z modes of the kesterite structure with Raman tensor entry-ratios of $c/d \ll 1$.

If one assumes that these modes are originating from a kesterite structure, one would estimate the c/d ratio (using the graph depicted in figure 4.12d) to be $c/d < 0.1$ since the maxima of the perpendicular configuration intensity are at rotation angles $\theta = 90° \pm^0_3$.

The mode at 250 cm^{-1} is quite close to the LO split T mode of ZnSe which is seen at 251 cm^{-1} by Irwin and LaCombe [74]. One can not exclude contributions from ZnSe in the mode measured at 250 cm^{-1} in the P/O-Raman measurement, since the LO split T mode from ZnSe has the symmetry[2] $T_{2,z}$, which is the same symmetry as the B_2 modes i. e. the same Raman tensor entries are non-zero.

One therefore needs to be careful when assigning a mode in this energy range to/or not to ZnSe. The literature review (summarized in figure 4.20) shows normalized Raman spectra from which the relative intensity of the peaks at around 250 cm^{-1} is extracted and correlated to the expected ZnSe content (as deduced from the composition given in the according publication). Figure 4.20 shows Raman spectra normalized with respect to the main mode intensity, along with the corresponding composition plotted in the phase diagram. When the main mode is normalized to 1 and the background signal at around 300 cm^{-1} is set to zero, one can clearly discern that the contribution of the 244-248 cm^{-1} mode is different compared to both the intensity of the main mode and of the one around 231 cm^{-1}. The elemental composition of the samples plotted in the phase diagram are aligned along the Cu_2SnSe_3-CZTSe-ZnSe tie line.

Since the compositions are close to the tie lines and the errors in the composition measurement are not defined, the only reliable conclusions that can be drawn are that a growing ZnSe content is expected the nearer the composition is to the ZnSe end of the CZTSe-ZnSe tie line (and no Cu_2SnSe_3) and no ZnSe is expected along the CZTSe-Cu_2SnSe_3 tie line. One observes a correlation of the 244-248 cm^{-1} peak intensity and the expected ZnSe content which leads to the conclusion that this mode could be ZnSe related since it

[2]The Raman tensors of ZnSe are given by:

$$T_{2,x} = \begin{pmatrix} 0 & 0 & 0 \\ 0 & 0 & d \\ 0 & d & 0 \end{pmatrix};\ T_{2,y} = \begin{pmatrix} 0 & 0 & d \\ 0 & 0 & 0 \\ d & 0 & 0 \end{pmatrix};\ T_{2,z} = \begin{pmatrix} 0 & d & 0 \\ d & 0 & 0 \\ 0 & 0 & 0 \end{pmatrix}; \tag{4.8}$$

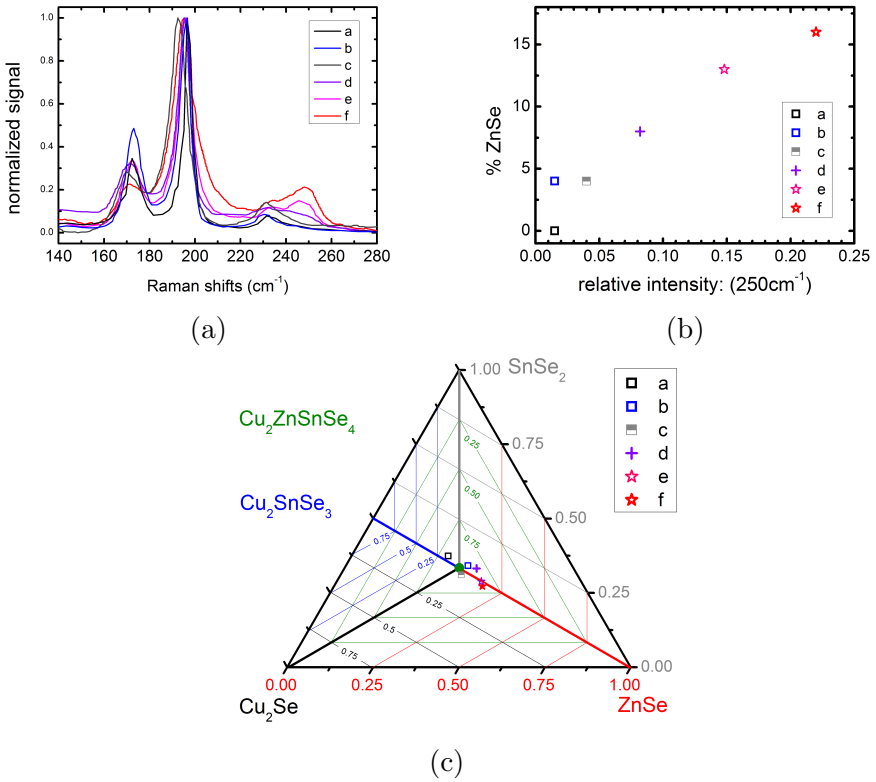

Figure 4.20: Raman spectra from literature normalized with respect to the main mode (figure a). The according compositions are plotted in the phase diagram (figure c). The 250 cm^{-1} relative intensities as a function of ZnSe content derived from figure c are plotted in figure b. The data is marked *a* to *f* and is taken from [52] (sample prepared at 673 K); [53]; [54]; [52] (sample prepared at 723 K); [55] (samples prepared at 450 °C and 550 °C respectively.

also coincides with the ZnSe LO mode.

The mode at 129 cm^{-1} has a very low signal with no clear evolution therefore no attribution.

4.4 Polarized Raman: polycrystalline CZTSe

The polarization dependency can also be measured on polycrystalline samples. Monitoring the change in Raman intensity of the modes when the polarization of the incident and scattered light are changed from perpendicular to parallel results in information on the symmetries of the modes. The Raman signal intensities of the perpendicular $I_\perp$ and parallel configurations $I_\parallel$ originating from randomly oriented crystals are calculated from the sum of the intensities originating from a rotated crystal. Equation 4.3 becomes:

$$I_{\perp/\parallel} \sim \sum_{\theta=0^\circ}^{360^\circ} \sum_{\psi=0^\circ}^{180^\circ} \sum_{\phi=0^\circ}^{360^\circ} |\hat{e}_\mathrm{x} \cdot T_{(\theta,\phi,\psi)} \cdot \hat{e}_\mathrm{y/x}|^2 \tag{4.9}$$

The depolarization ratio $I_\perp/I_\parallel$ is calculated for the Raman mode symmetries. The only parameter that can be varied in equation 4.9 is the Raman tensor entry ratio.

The simulation shows that the depolarization ratio is independent of the Raman tensor entry ratios for the E and B symmetry Raman modes of kesterite while it varies for the A(A1) symmetry mode[3]. The dependency of the depolarization ratio of the A symmetry modes on the a/b ratio is shown in figure 4.21 where the a/b ratio is varied over several orders of magnitude. When b dominates the Raman tensor, the depolarization ratio reaches 0.44 while it is 0.10 when a dominates. The cubic extreme where $a = b$ has a depolarization ratio of zero.

The depolarization ratio for the B symmetry modes is 0.49 for kesterite and stannite; it is independent of the Raman tensor entry ratio c/d and the same as for the stannite (or equivalent) B_1 and B_2 symmetry modes. The depolarization ratio is 1.43 for all E symmetry modes .

The simulation of the depolarization ratio demonstrates that for polycrystalline samples it is not possible to distinguish kesterite from stannite using the depolarization value of the mode symmetries since all B and E modes from kesterite and stannite (or equivalent polymorphs) are the same.

These calculated depolarization ratios permit to predict if the Raman signal intensities change when the polarization configuration is changed from a perpendicular to a parallel orientation for randomly oriented crystallites. The values calculated above mean that only the E symmetry modes can be distinguished by polarization dependent Raman measurements since they are the only ones growing in intensity while the A and B symmetry modes decrease.

[3] The Raman tensor is the same for A symmetry modes for both kesterite and stannite.

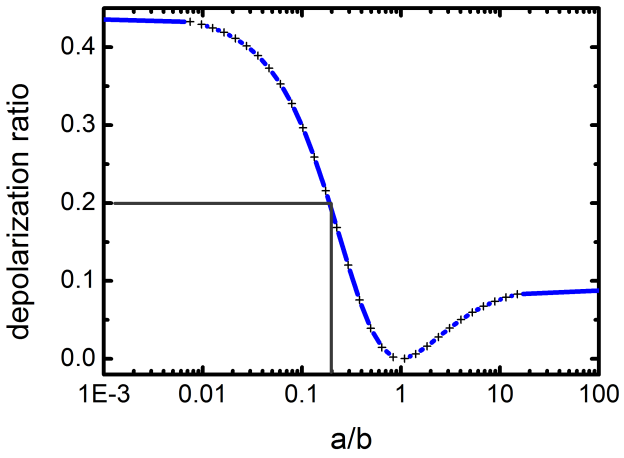

Figure 4.21: Calculated depolarization ratio of the A symmetry modes as a function of the a/b ratio.

However measuring the depolarization ratio is quite difficult as, in practice, the setup needs to be calibrated accounting for the polarization dependence of the optics. This need for normalization can be overcome by, for example, knowing the symmetry of the B modes. Since their depolarization ratio is known, they can be used for normalization.

The a/b ratio for the identified A modes can be estimated from the depolarization ratio of the A symmetry modes. Knowing the depolarization ratio of the B modes and normalizing the measurement to the known B symmetry modes, one can estimate this depolarization ratio of the A modes. Figure 4.21 can then be used to estimate the Raman tensor entry ratio a/b.

A polarization-dependent Raman measurement on polycrystalline samples is depicted in figure 4.22a where the spectra are normalized to the identified B symmetry modes (in the energy range 220-250 cm^{-1}). This leads to a depolarization ratio of the A symmetry modes of 0.4 which multiplied by the depolarization ratio of the B modes (0.49) gives an effective depolarization ratio of 0.2 so that $a/b = 0.2$. It should be noted that the different A symmetry modes can have different a/b ratios, but in this case no difference in the depolarization ratios and consequently on the a/b ratios was found. This is deduced from figure 4.22b showing the polarization dependent data as normalized on the main mode. All the A symmetry mode intensities change in the same way with polarization.

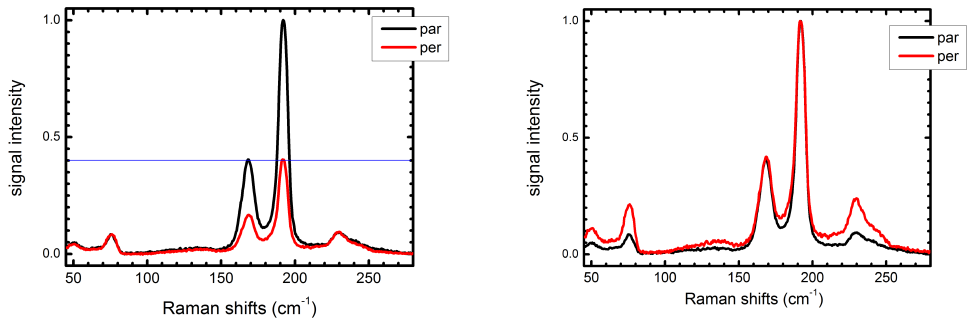

(a) (b)

Figure 4.22: Raman spectra from CZTSe absorber measured under parallel (black) and perpendicular (red) polarization configurations normalized to the B symmetry mode at $230\,\mathrm{cm}^{-1}$ (figure a) and to the A symmetry mode at $196\,\mathrm{cm}^{-1}$ (figure b).

One has to take into account that the simulation used for the above a/b ratio estimation assumes that the sample is composed of randomly oriented crystallites. This can explain the difference in Raman tensor entry ratio a/b between the values estimated here and calculated by Guc et. al. [50].

If the preferred orientation is known, the depolarization ratio dependencies of the ratio a/b can be recalculated accordingly leading to a more accurate value for a/b.

This implies that one could also go backwards from known a/b ratios to gain a possible map of the crystallite orientations present in the sample. One could calculate the depolarization ratio dependencies for different orientations. This can then be used to translate mappings of the depolarization ratio into orientations of crystallites. It should be noted that several orientations lead to the same depolarization limiting the information that can be extracted from this method. Of course there exist methods that are more appropriate to measure the orientations of crystallite like EBSD. But, the above method has the advantage that this further information is gained on top of the usual Raman strengths i.e. the ability to differentiate between CZTSe and ZnSe and to some extent the CTSe ternary.

4.5 Discussion and conclusion

An asymmetric broadening of the main mode to lower energies was attributed to the confinement of phonons because of the presence of lattice defects in the scattering volume. Other effects that could lead to such asymmetry like

a distribution of strain or composition or an inhomogeneous laser heating were excluded from playing a major role by looking at Raman measurements taken at different depths of samples and comparing these to the according composition.

In a second part, a polarization orientation experiment was performed on epitaxially grown samples. The result of the P/O Raman experiment is that four B_2-like modes and at least two A symmetry modes are confirmed while no B_1-like modes were found.

It was shown that the probed volume is most probably composed of a mixture of in-plane and out-of-plane oriented domains since the Raman signal intensity dependencies of modes attributed to the A mode show the expected behavior for a mix of in-plane and out-of-plane oriented domains dominated by the out-of-plane orientation. Therefore, one can assume that CZTSe is mostly oriented out-of-plane. As a result, the B_2-like modes are attributed to B symmetry and not to the E symmetry since the E modes have a constant zero intensity in the out-of-plane orientation.

Although the combination of modes does not lead to a definite attribution of our measured spectra to kesterite or stannite, an attribution to kesterite is favored by the absence of B_1-like symmetry modes (expected for the stannite structure).

The attribution of the spectrum to kesterite is backed by a higher resolution measurement showing a clear shoulder in the energy range 160-180 cm^{-1} proving that we might have three A symmetry modes and consequently that the measured spectrum can be attributed to kesterite. Unfortunately these higher resolution measurements were made on a different spot of the sample. The repetition of the full P/O measurement with higher spectral resolution is not yet finished.

The results are summarized in table 4.4 and compared to P/O Raman measurements on single crystals by Guc et. al. [50]. The main discrepancy is the energetic position of the B mode at 178 cm^{-1} which could be attributed by comparison with DFT calculations [50]. The P/O measurement discussed above puts a B symmetry mode at 216 cm^{-1} which was not found by Guc et. al. due to the way the spectra were fitted in two energy ranges, intersecting where the B mode is found in this work.

The presence of the out-of-plane configuration is opposed to what one might expect knowing the lattice mismatches for the two possible configurations (out-of-plane $\approx 0.8\,\%$; in-plane $\approx 0.3\,\%$). However, the lattice mismatches are calculated for lattice parameters measured at room temperature. The out-of-plane configuration might be favored when the samples are at elevated temperatures during growth due to different expansion coefficients of both materials. Assuming the reference lattice constants are correct, the lay-

ers would be strained which would explain the slightly higher mode energies in the epitaxial samples compared to the polycrystalline ones (196 cm^{-1} vs. 194-195 cm^{-1}).

In the last section the depolarization ratio $I_{\perp}/I_{\parallel}$ was calculated for randomly oriented crystals. This calculation shows that only the E modes are expected to have a higher intensity in the perpendicular polarization configuration while the A and B symmetry modes have a depolarization ratio lower than one. The simulation also shows that only the depolarization ration of the A modes is Raman entry ratio dependent. This allows a rough estimation of the Raman tensor entry ratios $a/b \approx 0.2$ assuming the crystallites are randomly oriented. Comparing this estimation with literature shows that crystallites in the polycrystalline samples have some preferred orientation.

Guc et. al. [50]		This work	
symmetry	peak pos. (cm^{-1})	symmetry	peak pos. (cm^{-1})
E	**138**	-	130
B	157	B_2-like	159
A	170	A	172
A	174	A	178
B	**178**	-	-
E	**189**	-	-
A	196	A	196*
-	-	B_2-like	216
E	224-231	-	-
B	235-239	B_2-like	237
B	245-250	B_2-like	250

Table 4.4: Symmetry of the CZTSe Raman modes measured by P/O Raman experiments as deduced by Guc et. al. [50] and during this thesis. The bold values represent peaks attributed only by comparison with theory. The * marks that the used fit shape was an asymmetrically broadened one.

Chapter 5

Room temperature photoluminescence

The photoluminescence (PL) spectra measured on CZTSe samples vary significantly, as will be shown in the first part of the chapter. The origin of theses different luminescent transitions is investigated by means of an excitation intensity dependent room temperature photoluminescence study. The luminescence peaks are assigned to different band to band transitions. The presence of materials of different band gaps explains the shift of the band gaps which are extrapolated from quantum efficiency (QE) measurements. A simple analytical model is presented which shows how different band gaps influence the quantum efficiency spectra. The chapter ends with a discussion of the effect that a mixture of materials (of different band gaps) in the absorber has on the solar cell efficiency. The maximal achievable solar cell parameters are simulated under the ideal Shockley-Queisser conditions (i. e. the solar cell behaves like an ideal diode, it has a QE of 0 below the band gap and 1 above the band gap and only luminescent recombinations are allowed).

5.1 Multiple materials by RT-PL

The PL spectra measured on CZTSe during this project show varying peak positions and shapes. These variations are seen in both the PL spectra shown in literature and measured in our lab. This effect is demonstrated in figure 5.1 which depicts a variety of PL spectra of a number of similar CZTSe films. The PL transitions depicted in figure 5.1a show the range of different PL spectra seen on CZTSe samples made in our lab that are grown in the Cu-poor Zn-rich composition, and which give decent solar cells with a conversion efficiency between 4 % and 7 % . The spectra depicted

in figure 5.1b are digitized room temperature PL spectra from literature. It should be noted that all PL measurements shown in this thesis are made on a micrometer sized spot. This leads to the fact that macro measurements, as usually shown in literature, present a broader, smeared out spectrum averaging the inhomogeneities that might be present in the sample.

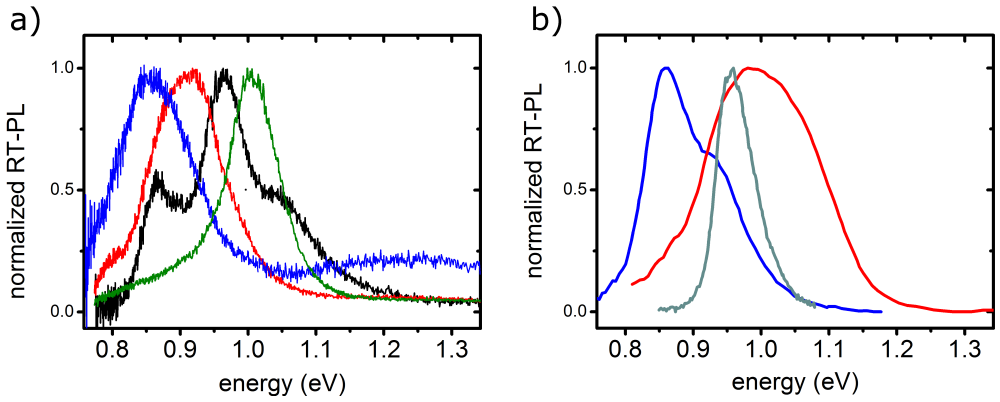

Figure 5.1: Room temperature green excitation PL spectra measured on CZTSe in our lab (figure a) and room temperature PL digitized from literature (figure b). The curves depicted in red and blue are from [115] and the green curve is from [7]. All spectra are normalized for a better overview.

All these samples have a very similar composition and show very similar Raman spectra. Based on the Raman analysis discussed in detail in the previous chapter, and the fact that the Raman spectra are very similar one can conclude that the main phase is kesterite $Cu_2ZnSnSe_4$. However, the absorbers can contain smaller amounts of other polymorphs with lower band gaps (as summarized in section 1.1). In addition secondary phases can exist, such as ZnSe, SnSe, $SnSe_2$, Cu_2SnSe_3 and other CuSn-selenides or various Cu-selenides. All these different phases and crystal modifications will have different band gaps and defect energies and will therefore show emissions at different energies. The intensity of each emission does not necessarily correlate with the amount of material present since the PL intensity strongly depends on the ratio of radiative to non-radiative recombinations in each material. Based on the assumption that the various absorbers are similar, the different spectra are fitted with the same number of peaks with fixed energetic positions. Examples for such fits are shown in figure 5.2. The spectrum in figure 5.2b could be fitted with only three peaks, with different energies than the emissions observed in figure 5.2a. But assuming that the materials in our absorbers are more or less the same, the PL emission should

show maxima at the same energies, allowing for small shifts due to strain or defects.

All the measured RT PL spectra have their transition maxima at energy positions similar to those shown in figure 5.2 or can be deconvoluted using the same distinct peak positions. Depending on the measured sample these peak positions usually are shifting within 0.02 eV: the distinct peak positions fitting the vast majority of our samples are (0.83±0.03) eV, (0.90±0.01) eV, (0.96±0.01) eV, and (1.02±0.01) eV. The errors are given by the extremal values of all fitted positions with only two outlier measurements discarded. The peak at higher energies shifts between 1.2 eV and 1.4 eV and is related to a ZnSe secondary phase as discussed in section 3.3. The full width at half maximum for the ZnSe PL is high (up to 0.4 eV) while for the lower energy peaks it is around 0.15 eV for the 1.02 eV peak and around 0.04 eV (up to 0.09 eV for some samples) for all other lower energy peaks. As an example for fitting other spectra the fit of the red curve from figure 5.1 is presented in figure 5.2b. It is shown as an example for samples that appear different but can still be deconvoluted with the same peaks.

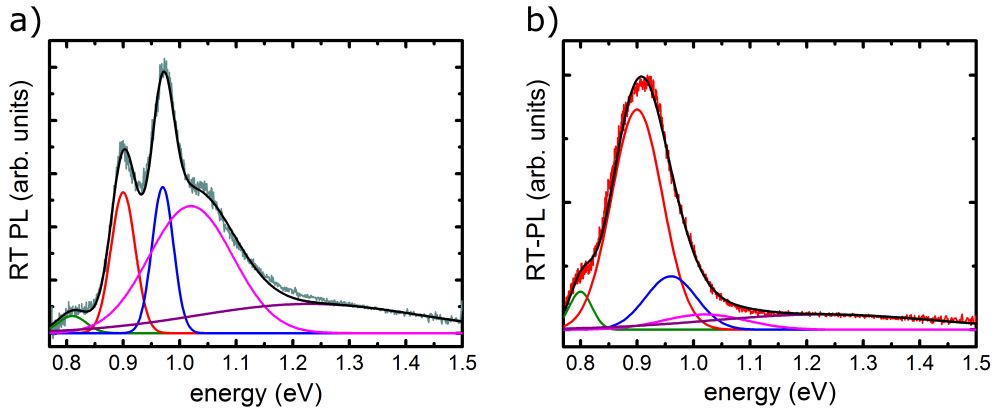

Figure 5.2: RT-PL spectra fitted using multiple Gaussians. Figure a) shows a fit from the intensity dependent study. Figure b) shows the fit of the red curve from figure 5.1.

It turns out that not only PL spectra measured on samples produced in our lab but also PL spectra from literature can be fitted with five peaks with fixed energies. A fit example of literature data is depicted in figure 5.3 showing digitized room temperature PL measurements from Shin et. al. [115] (figures a and b) and Repins et. al. [7](figure c), and fitted with the same peak positions and widths as in figure 5.2.

The intensity ratio of the various peaks cannot be correlated with the composition or the Raman spectra of the samples. Within one sample no

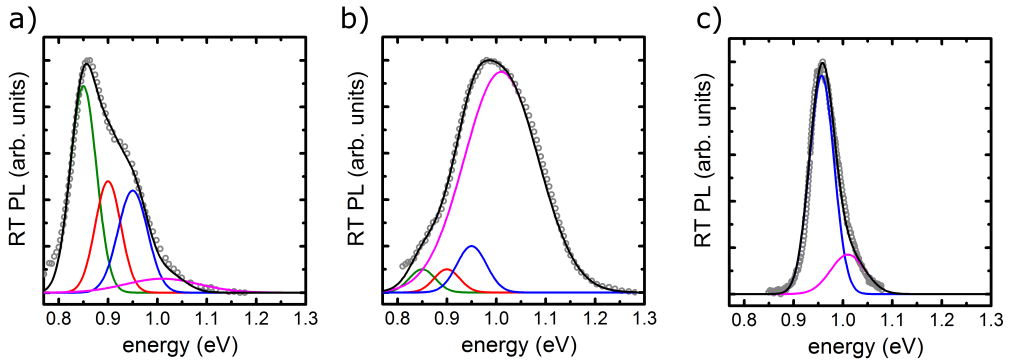

Figure 5.3: Room temperature PL from literature fitted with the same peaks as in figure 5.2. The spectra in figures a,b are from [115] and the spectrum of figure c is from [7].

correlation between the maps of the various PL peaks and any feature in the Raman spectra can be found. No correlation was found between the signal intensity maps calculated by integrating both the PL and Raman spectra for different energy ranges.

To study whether the observed emissions can be defect related or due to band-band transitions, the dependence of the emission intensities on the laser excitation intensity was checked. A power law as discussed in section 1.3 is expected. One sample shows all five transitions simultaneously in a particularly well resolved way, see figure 5.2a. One can therefore measure the power laws of all the transitions at once.

Figure 5.4 shows a double logarithmic plot of the evolution of the RT-PL peak intensity as a function of the excitation laser power for the sample shown in figure 5.2a, where a spectrum with 2 mW excitation power is shown as an example. The PL intensities are fitted using Gaussian peak shapes. The peak widths do not change with excitation intensity therefore they are kept constant in the fit. The change of the intensity can be taken from the maximum or the peak area. The k value is then given by the slope of the linear fit between the logarithm of the PL intensity and the logarithm of the excitation intensity. The luminescence at 1.2 eV is attributed to a ZnSe secondary phase in accordance with the findings discussed in section 3.3. This PL has a k value of 0.75 indicating a defect related transition which corroborates the attribution of this transition to a defect related transition in ZnSe in section 3.3.

The k values of the PL transitions at 0.82 eV, 0.9 eV, 0.97 eV, and 1.02 eV are higher than 1. In various samples where only one of these peaks is dominating the spectra, the same result is found: all four low energy emissions

have an exponent larger than one. Since defect related transitions always show an exponent smaller than one, the observation of $k > 1$ clearly indicates that these four observed transitions are band-band transitions. This suggests that different materials, i. e. different crystal polymorphs or secondary phases, are present in the sampled volume. It should be noted that this $k > 1$ power law is also measured on other samples where the PL shows fewer or only one of the above mentioned transitions confirming their band to band character.

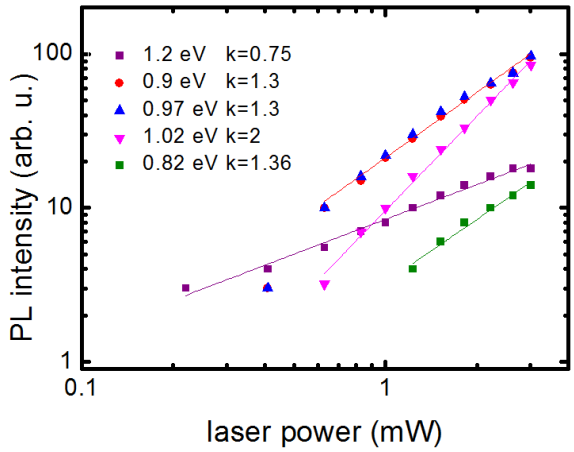

Figure 5.4: Evolution of the fitted PL intensities as a function of the excitation laser intensity. A fitted PL spectrum for one laser power is shown in figure 5.2a.

Although it is difficult to determine which polymorphs or secondary phases correspond to the different observed band gaps, some possible phases can be excluded to a certain extent. As for the exclusion of secondary phases: SnSe and $SnSe_2$ are unlikely since they are not seen in the green excitation Raman spectra, measured on the same spot where the PL of figure 5.2a is measured, and shown in figure 5.5. The expected Raman modes for SnSe and $SnSe_2$ are shown in this figure. SnSe and $SnSe_2$ can be measured with Raman spectroscopy on our CZTSe solar cell absorbers under the same measurement conditions as in figure 5.5 as discussed in section 3.2. Additionally, Sn-selenides are un-likely secondary phases in the composition range, which is Sn-poor. It also appears that Cu-selenides can be excluded as they have significantly higher band gaps [116] than the energies of the observed emissions.

Therefore it is considered that the most likely explanation for the different band gaps is the occurrence of various polymorphs of $Cu_2ZnSnSe_4$, the

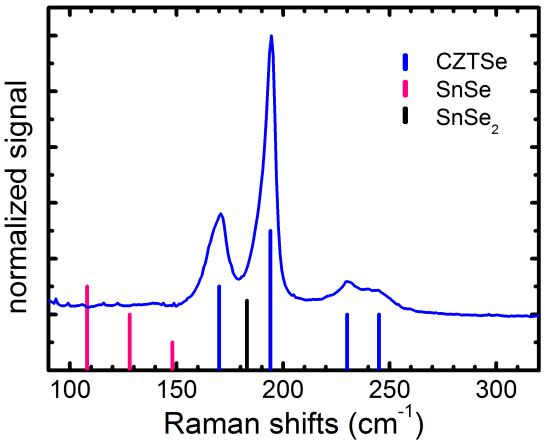

Figure 5.5: Green excitation (514.5 nm) Raman spectrum measured on the sample used for the intensity dependent PL study shown in figures 5.2a and 5.4. The expected Raman modes for CZTSe, SnSe, and $SnSe_2$ are indicated.

occurrence of CTSe secondary phases or areas with high defect concentrations. The cubic Cu_2SnSe_3 is a candidate to explain the emission at 0.82 eV. Since there is no correlation with Raman data proving the presence of CTSe, one can not conclude that this emission is due to this ternary phase.

The band gaps of various polymorphs of $Cu_2ZnSnSe_4$ have been calculated by different methods ranging from DFT to GW as summarized in section 1.1. Although there is no perfect agreement on the actual values of the band gaps, all calculations find a difference of around 150 meV between the band gaps of kesterite and stannite. The band gap of the Cu-Au ordered structure is calculated to be another 30 meV below the band gap of stannite. These differences in band gap energies are in the same range of the differences observed in the PL peak energies. Although no definite correlation of the four emissions to a concrete polymorph or secondary phase can be made, the important observation is that there are different materials present in the absorber, which have different band gaps. This is certainly detrimental to the solar cells made from these absorbers, as is discussed in detail in the following.

It is important to know how these materials are arranged within the film since different arrangements affect the solar cell efficiencies differently. The possible arrangements are: a columnar structure with different materials next to each other in the plane of the film, a layered structure with the different materials on top of each other or in a three dimensional intermixed

arrangement.

Comparing the spectra from a spatially resolved PL measurements on one sample shows that the same contributions are found in every measured spot with slightly varying intensity. This observation rules out that the materials are arranged in a columnar fashion. To check for the appearance of a layered structure, PL measurements are performed in different depths of the film which were made accessible by sputtering craters of different depth into the film. Additionally SIMS (secondary ion mass spectroscopy) measurements were made. Both methods don't give any indication of the presence of different layers in the films (that correlate to one of these transitions). In some films, the composition of the surface or near the back contact is different from the composition of the majority of the film, as was observed in [117] [118], but none of the films showed a layered composition. Therefore it is concluded that the different materials must be 3-dimensionally intermixed, as was shown for the case of ZnSe in some of our $Cu_2ZnSnSe_4$ films by atom probe tomography [100].

5.2 Effect of multiple materials on the solar cell

The presence of materials with different band gaps in the absorber can influence the resulting solar cells. The effect of multiple materials on both the quantum efficiency (QE) and the maximum achievable power conversion efficiency in the Shockley Queisser limit is discussed in this section.

5.2.1 Varying band gap in QE

A selection of QE curves measured on samples with conversion efficiencies higher than 4 % is shown in figure 5.6. The focus of the spectra is on the low energy edge of the QE. The full QE spectra are shown in the inset. The band gap can be approximated by a linear extrapolation of the low energy edge of the QE spectrum. For this extrapolation the approximately linear part of the QE spectrum in the range between about 10 % and 40 % QE is used (as an example see the blue lines in figure 5.6). The band gaps approximated this way vary between 0.9 eV and 0.96 eV, i. e. between the central two energies that are observed in the PL spectra of the same absorbers. Some samples show a strong tailing towards lower energies. This tailing can be attributed to Urbach tailing or to a second band gap material. Plotting the QE measurements in a logarithmic plot (depicted in figure 5.6b) shows that the low energy edge of the QE is linear which favors the attribution of the tailing to

a strong Urbach tailing and not to a second band gap material while it does not exclude the presence of a second material in the absorber.

A similar behavior is observed in the QE spectra reported in the literature: the QE spectra of nominally pure $Cu_2ZnSnSe_4$ extrapolate to a range of different band gaps: the QE' s from Brammertz et. al. [119] extrapolate to 0.88 eV and 0.94 eV, while the QE from Repins et. al. [7] for example extrapolates to 0.9 eV. The linear extrapolation of the QE is not the most ideal method to determine the band gap, but it certainly gives an idea of the absorption edge and its variation. For a solar cell absorber which exhibits only one band gap, different QE would extrapolate to the same band gap value, as is the case for example in $CuInSe_2$ [120]. In the following it will be shown that the presence of more than one fundamental band gap can lead to a continuous change in the apparent band gap as extrapolated from QE.

The quantum efficiency QE near the fundamental band gap is given by the following formula: $QE \approx 1 - e^{(-\alpha L)}$ where α denotes the absorption coefficient and L is equal to the effective collection length which is equal to the sum of the space charge region width and the minority carrier diffusion length [121]. The QE spectra are described assuming the same collection lengths of the different materials within the sample.

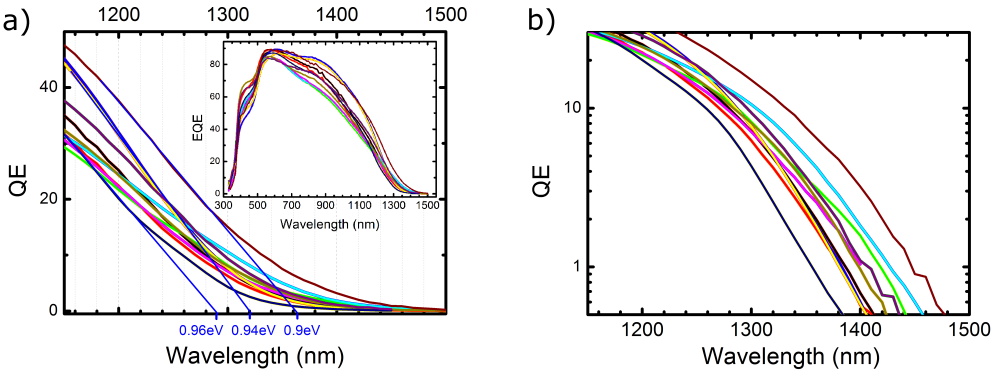

Figure 5.6: QE measurements of CZTSe solar cells with conversion efficiencies higher than 4 % in the energy range 1150 nm to 1500 nm. The blue lines show the linear extrapolations to the band gap for three QE' s (figure a). The inset shows the QEs in the full measured energy range (figure a). Figure b shows the same QE' s in a logarithmic plot.

In this model the presence of two different materials with different band gaps and absorption spectra is assumed. The aim of this simple modeling is to demonstrate the effect that the existence of several band gaps can have on the observed QE spectra. The absorption in the model is simulated using

the Beer–Lambert's law with the equation:

$$A = 1 - \exp^{(d.f.\alpha_1 + d.(1-f).\alpha_2)} \tag{5.1}$$

Here f is a parameter representing the fractions of the two simulated materials, d is the thickness of the whole layer (set to 2 μm in the simulation) and $\alpha_{1,2}$ are the absorption coefficients of the two materials. The result of this simulation is shown in figure 5.7. The absorption coefficients are simulated using an optical modeling toolkit in the program Diplot [122] introducing an additional band tailing at low energy (shown in the inset of figure 5.7).

The materials have been simulated with a direct band gap E_g at 0.9 eV and at 0.96 eV, the two extreme values observed for the band gap determined from the QE spectra. Both materials are simulated with the same absorption strength (α_0) of 18000 cm^{-1} and with an Urbach energy (E_U) in the range of 15 meV, which is typical for a polycrystalline material [123]. E_1 and α_1 are parameters whose only task is to make the Urbach tail and the band-band part of the absorption a differentiable function.

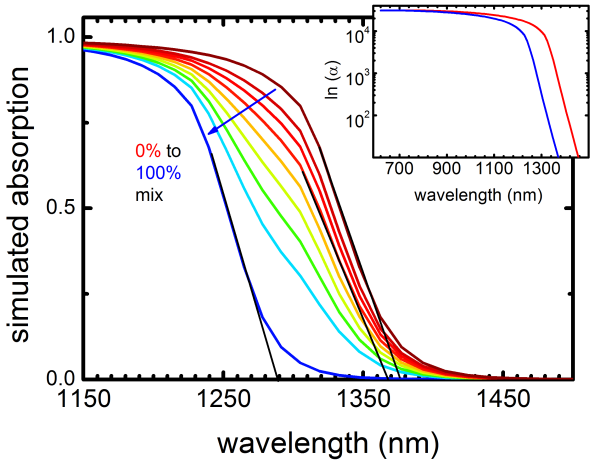

Figure 5.7: Simulated absorption of a mix of two materials of 0.9 eV band gap (red) and 0.96 eV (blue). The black lines show the linear extrapolation to the band gap of the mix for three absorption curves. The inset shows the logarithm of the two simulated absorption coefficients (using Diplot) for the two materials used for the simulation.

The absorption curves were not fitted to any QE or experimental absorption spectra. Reasonable parameters are used for the two spectra that represent typical absorption spectra in polycrystalline semiconductors with

some influence of defect tailing. The only difference between the two absorption coefficients is that they are shifted in band gap by 60 meV. The values for the band gaps are chosen based on the extrapolation of the QE which is in accordance with two of the band gaps deduced from the intensity dependent RT PL study. The result of this simulation is shown in figure 5.7. When extrapolating the absorption spectra linearly, as done for the QE spectra, an almost continuous transition from the high energy band gap to the low energy band gap is observed. Additionally, it is also seen that the slope becomes rather shallow for certain mixtures.

The spectrum shown in figure 5.7 is just the absorption spectrum and not a fit to QE. The QE spectra increase much more slowly with decreasing wavelength, since the slope of the QE spectrum also depends on the collection probability. But even the absorption alone without any reduction by non-ideal collection can become shallow with a small fraction of the lower band gap material. This simulation shows that the presence of two different materials with different band gaps can lead to an extrapolation of the absorption which results in a continuously changing effective band gap. Thus it is possible to explain the observed variation in band gaps by the presence of different materials with only two different band gaps. For this simulation the most conservative approximation is chosen (only two different band gaps in the absorber). A more complex simulation with more materials and a larger variety of resulting absorption spectra as implied by the PL measurements will likely lead to a better agreement with the experimental data.

5.2.2 Shockley Queisser limit of material mix

The different band gaps found by room temperature photoluminescence are detrimental to the performance of the resulting solar cell. In an attempt to quantify these losses, the impact of a mix of four semiconductors on the solar cell performance under Shockley-Queisser (SQ) conditions [5] is therefore investigated. This work is similar to the calculations by Rau et. al. who calculated the influence of band gap fluctuations [124]. Here, a fixed number of distinct band gaps is considered. The worst case, a maximal number of four band gaps simultaneously seen on one sample is simulated. The simulation is performed for otherwise ideal conditions, namely the conditions of the Shockley-Queisser model [5]: radiative recombination as determined by black body emission as the only recombination path, a diode ideality-factor of one, and a QE of one above the band gap. The efficiency of five different solar cells is calculated: four solar cells which consist of a single material each with the four different band gaps found in the PL investigations and a fifth cell, which consists of a mix of the four materials. It is assumed that

the materials are mixed in a three dimensional fashion since this describes our experimental findings better than a columnar structure, where the materials are arranged next to each other in the plane of the film, or a layered structure, where the materials are arranged on top of each other.

To calculate the efficiency of each solar cell the short circuit current J_{sc}, the open circuit voltage V_{oc} and the fill factor FF are needed. The J_{sc} is calculated by integrating the solar spectrum above the respective band gap, i. e. assuming a quantum efficiency of one for all energies higher than the band gap. For the cell with the material mix, the J_{sc} of the highest band gap material is used, since in a 3-dimensional intermixing of different materials the current has to pass all materials and is limited by the lowest J_{sc}. The open circuit voltage is obtained by rearranging the ideal diode J-V behavior:

$$V_{oc} = \frac{kT}{e} \cdot \ln\left(\frac{J_{sc}}{J_0} + 1\right) \tag{5.2}$$

Thus, to calculate V_{oc}, the reverse saturation current J_0 in addition to the short circuit current J_{sc} is needed. J_0 is calculated assuming radiative recombination as the only recombination path, by integrating the black body spectrum of a body at 300 K above the band gap of each cell [5]. The reverse saturation current of the solar cell with the material mix is calculated as the arithmetic average of saturation currents of the four cells with pure absorbers, since each material can emit its black body radiation in a mixed 3-dimensional arrangement. The V_{oc} of each cell was then calculated according to equation 5.2 with the short circuit current and the reverse saturation current of each cell.

To determine the fill factor of each cell the J(V) curve is calculated with the ideal diode equation using the respective J_0 and J_{sc} of each cell. The efficiency is calculated from the maximum power point of this calculated ideal diode, which also gives the fill factor. Figure 5.8 summarizes the results of single band gap solar cells in the SQ limit for the band gaps seen in the RT PL study as well as the results for a mixed band gap cell. The solar cell parameters J_0, J_{sc}, V_{oc}, and the efficiency are shown as columns normalized to the highest value and grouped for each of the band gaps 0.84 eV, 0.90 eV, 0.96 eV, 1.02 eV and the mixed band gap cell. A break in the vertical axis is introduced to visualize the exponentially decaying J_0.

The open circuit voltage of the mix $V_{oc\ mix}$ mainly depends on $J_{0\ mix}$ since J_0 varies over several orders of magnitude (see figure 5.8) as opposed to J_{sc} which varies only within 10 % for the considered solar cell. Using the J_{sc} of the lowest band gap would only increase $V_{oc\ mix}$ by 3 mV.

The main result is that the ideal efficiency of the mix (25.7 %) is lower than the lowest efficiency of a single band gap (26.1 % with a 0.84 eV band

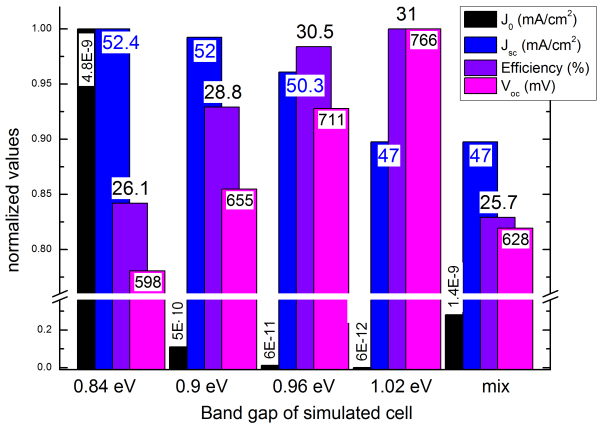

Figure 5.8: Solar cell parameters (j_0, J_{sc}, V_{oc}, efficiency) as a function of the band gap calculated in the Shockley-Queisser conditions. The simulation results for a device with the mix of the four band gaps is labeled *mix*. The highest values of each parameter are normalized to one for a better overview.

gap). The $V_{oc\ mix}$ (628 mV) is strongly influenced: it is 138 mV lower than the V_{oc} of the best single band gap cell and it is lower by 55 meV than the average V_{oc} of the single band gaps. The same simulation without the lowest band gap shows, as expected, a less dramatic decrease in the solar cell parameters (i. e. $V_{oc\ mix} = 681$ mV and an efficiency of 28.1 %, i. e. a 10 % drop in efficiency).

These losses of the mixed band gap cell compared to a single band gap cell, are already significant in the ideal case of only radiative recombinations. It is expected that the losses due to non-radiative recombination are amplified by the coexistence of multiple materials: for example the interface area between the 3-dimensionally mixed materials will be large and will likely contribute to enhanced recombination.

5.3 Conclusion

Room temperature PL of $Cu_2ZnSnSe_4$ often shows several peaks in one sample or varying peak energies for different samples. This is unexpected on a sample where no secondary phases are detected. By using intensity dependent PL measurements, it is found that the highest energy emission which was previously attributed to a ZnSe secondary phase (4.7d) is a defect re-

lated transition, in agreement to the previous ascription. In the energy range expected for the band gap of $Cu_2ZnSnSe_4$ up to four different emissions are observed, which were shown by intensity dependent measurements to be due to band-band transitions. Thus, up to four different materials with different band gaps are present in the absorber. One can only speculate that there are different polymorphs of $Cu_2ZnSnSe_4$ present, as well as additional secondary phases. This mixture of materials can explain the different observed band gap values obtained from extrapolating the QE spectra, as shown in a simple simulation of the absorption spectrum of a thin film containing two different materials with different band gaps. This presence of different band gaps within the absorber of a solar cell is detrimental for the efficiency of the solar cell. When the efficiency of a mixed solar cell is simulated under the ideal conditions of the SQ model one finds that the efficiency is lower than the lowest efficiency of a cell with a single band gap, where the band gap energies are taken from energies found in the PL study. It is mostly the open circuit voltage which is affected. For a further improvement of the efficiency of kesterite solar cells, a better control of the different materials will be essential.

Summary

This last chapter briefly summarizes the findings of this thesis and discusses them in the context of the ongoing research and on the subject matter. The main aim of this project was to provide the tools to identify secondary phases and polymorphs in CZTSe solar cell absorbers. The samples were therefore studied by Raman and Photoluminescence spectroscopy.

All the important setup improvements have been made (Raman implementation, blue excitation, accurate laser power determination, camera for laser spot determination) but still some improvements in the software are needed for a more convenient measurement such as enabling a more convenient (or automatic) energy calibration and laser focusing, and a higher flexibility in the measurement (e.g. giving the possibility for scripting).

Chapter three treated the detection of several secondary phases present in CZTSe. The Raman spectrum of a Cu-rich Sn-rich sample could be attributed to a CTSe and CZTSe mix by correlating the contribution of the main Raman modes of these two phases to their relative content in the sample. The assignment of the mode at $181\,\mathrm{cm}^{-1}$ to CTSe was thereby confirmed. The CTSe literature attributes this main CTSe mode to the monoclinic phase which is not consistent with the observed syntaxy of these two phases (i. e. mixed and oriented growth (to each other) of the crystals of CTSe and CZTSe). As shortly discussed, the cubic phases are more suitable candidates for this intermixed epitaxial-like growth since they have less lattice mismatch to the CZTSe and GaAs lattices. These cubic phases might therefore be the origin of the Raman mode assigned in literature to the monoclinic phase. This raises some questions about literature results as the crystal structure can influence the mode energies. A way forward should include growing phase pure CTSe ternaries and investigating these with experimental techniques permitting the clear identification of the crystal structure (for example single crystal X-ray diffraction) to confirm or correct the Raman fingerprints of the found ternary phase. The next step would be to grow the CTSe ternary on a CZTSe substrate in order to identify the CTSe form which is most likely to appear as a secondary phase during the growth of

CZTSe.

The second section discussed the phase composition of a $SnSe_x$ capping layer on CZTSe samples (before and after annealing) as detected by Raman spectroscopy. The presence of $SnSe_2$ and amorphous selenium phases were detected in this capping layer. Further measurements confirmed that concentrated hydrochloric acid (HCl) can be used to remove the tin-selenide phases remaining on the capped CZTSe sample after heat treatment (i. e. SnSe and $SnSe_2$). Though, by the time this thesis ended newer growth recipes made the annealing step unnecessary, one could still consider such a capping layer as it can be removed and since it protects the absorber layer whilst it is transferred to the cell finishing step. However, the effect of this layer and its removal would need some investigation.

The last section discussed the ZnSe secondary phase. A room temperature photoluminescence emission was found at 1.2-1.4 eV. This could be clearly correlated to a sub-band gap excited defect luminescence of ZnSe by spatially correlating the PL emission to the known Raman signal of ZnSe. This shows that room temperature PL is a technique sensitive to comparatively small amounts of the ZnSe secondary phase. Here one could consider studying the effect of the growth parameters on the formation of ZnSe inclusions, their doping, and distribution in the CZTSe absorber with atom probe measurements for example; thereby, studying the effect of ZnSe on the solar cell performance of CZTSe solar cells.

In the second experimental chapter (i.e. chapter 4), the Raman spectrum of CZTSe was studied. An asymmetric broadening of the main mode to lower energies was attributed to the confinement of phonons because of the presence of lattice defects in the scattering volume. Other effects that could lead to such asymmetry like a distribution of strain or composition or an inhomogeneous laser heating were excluded from playing a major role by looking at Raman measurements taken at different depths of samples and comparing these to the according composition. In a second part, polarization orientation dependent Raman measurements were made on epitaxial samples in order to assign the modes to their symmetry and identify the polymorph present in the sample. The advantage of the epitaxial growth is that the substrate provides a preferred orientation for the growth. However, different orientations of the CZTSe on the GaAs substrate are possible. By comparing a simulation and the measurement, it turned out that the considered sample is mostly in the kesterite structure and oriented predominantly with its c axis perpendicular to the plane defined by the surface of the substrate. This assessment is based on the identification of three A symmetry modes, favoring the kesterite structure, and of four modes that have a B_2-like symmetry while no B_1-like symmetry modes are found, thereby partially excluding the

stannite structure. These first results also lead to an estimation of the Raman tensor entry ratios. For future experiments, one could investigate the effect of the growth parameters on the crystal structure and orientation as elucidated by polarization orientation dependent Raman spectroscopy. Thinner samples could be analyzed in order to minimize the number of disparately oriented domains in the probing volume and therefore be able to obtain a fingerprint of a phase pure polymorph.

The last chapter focused on the room temperature photoluminescence of $Cu_2ZnSnSe_4$ which often shows several peaks in one sample or varying peak energies for different samples. This is an unexpected behavior on samples where no secondary phases are detected. In the energy range expected for the band gap of $Cu_2ZnSnSe_4$, up to four different emissions are observed, which intensity dependent measurements suggest to be associated to band-band transitions. Thus, up to four different band gaps are present in the absorber. Since no additional secondary phases were detected, one can only speculate that there are different polymorphs of $Cu_2ZnSnSe_4$ present in the sample or secondary phases that are present below the detection limit. This reflects the fact that the band gap of CZTSe is yet unclear, implying that some more fundamental work should be put into identifying the source of these different band gaps. The mixture of materials can explain the different observed band gap values obtained from extrapolating the QE spectra, as shown in a simple simulation of the absorption spectrum of a thin film containing two different materials with different band gaps. The presence of different band gaps within the absorber of a solar cell is detrimental for the efficiency of the solar cell. When the efficiency of a solar cell (whose absorber contains a mixture of phases) is simulated under the ideal conditions of the SQ model, one finds that the efficiency is lower than the lowest efficiency of a cell with a single band gap (the band gap energies are taken from the PL study). It is mainly the open circuit voltage which is affected.

For a further improvement of the efficiency of CZTSe solar cells, a better control of the different phases present in the absorber will be essential. The synthesis needs to be improved in terms of compositional uniformity hopefully leading to phase or even polymorph purity.

Bibliography

[1] J. Newton. *Uncommon Friends: Life with Thomas Edison, Henry Ford, Harvey Firestone, Alexis Carrel, and Charles Lindbergh*. Mariner Books, 1987. 5

[2] A. Feltrin and A. Freundlich. Material considerations for terawatt level deployment of photovoltaics. *Renewable Energy*, 33(2):180–185, 2008. 5

[3] European Commission, Critical Raw Materials for the EU. `http://ec.europa.eu/enterprise/policies/raw-materials/critical/index_en.htm`. 5

[4] C.P. Chan, H. Lam, and C. Surya. Preparation of Cu_2ZnSnS_4 films by electrodeposition using ionic liquids. *Solar Energy Materials and Solar Cells*, 94(2):207 – 211, 2010. 6

[5] W. Shockley and H.J. Queisser. Detailed balance limit of efficiency of p-n junction solar cells. *Journal of Applied Physics*, 32(3):510–519, 1961. 6, 124, 125

[6] W. Wang, M.T. Winkler, O. Gunawan, T. Gokmen, T.K. Todorov, Y. Zhu, and D.B. Mitzi. Device characteristics of CZTSSe thin-film solar cells with 12.6% efficiency. *Advanced Energy Materials*, 2013. 6

[7] I. Repins, C. Beall, N. Vora, C. DeHart, D. Kuciauskas, P. Dippo, B. To, J. Mann, W.C. Hsu, and A. Goodrich. Co-evaporated $Cu_2ZnSnSe_4$ films and devices. *Solar Energy Materials and Solar Cells*, 101:154–159, 2012. 6, 116, 117, 118, 122

[8] G. Brammertz, M. Buffière, S. Oueslati, H. Elanzeery, K. Ben Messaoud, S. Sahayaraj, C. Köble, M. Meuris, and J. Poortmans. Characterization of defects in 9.7 % efficient $Cu_2ZnSnSe_4$-CdS-ZnO solar cells. *Applied Physics Letters*, 103(16), 2013. 6

[9] I.D. Olekseyuk, I.V. Dudchak, and L.V. Piskach. Phase equilibria in the Cu_2S-ZnS-SnS_2 system. *Journal of Alloys and Compounds*, 368(1-2):135–143, 2004. 6

[10] I.V. Dudchak and L.V. Piskach. Phase equilibria in the $Cu_2SnSe_3SnSe_2$ ZnSe system. *Journal of Alloys and Compounds*, 351(1):145–150, 2003. 6, 35, 53, 54, 55

[11] G.N. Lewis. The atom and the molecule. *Journal of the American Chemical Society*, 38(4):762–785, 1916. 9

[12] L. Pauling. The nature of the chemical bond. *Cornell University Press, Ithaka*, 1939. 9

[13] C.H.L. Goodman. The prediction of semiconducting properties in inorganic compounds. *Journal of Physics and Chemistry of Solids*, 6(4):305 – 314, 1958. 9

[14] B.R. Pamplin. Super-cell structure of semiconductors. *Nature*, 188(4745), 1960. 9

[15] A. Walsh, S. Chen, S.-H. Wei, and X.-G. Gong. Kesterite thin-film solar cells: Advances in materials modelling of Cu_2ZnSnS_4. *Advanced Energy Materials*, 2(4):400–409, 2012. 10

[16] J. Paier, R. Asahi, A. Nagoya, and G. Kresse. Cu_2ZnSnS_4 as a potential photovoltaic material: A hybrid Hartree-Fock density functional theory study. *Physical Review B*, 79(11), 2009. 10, 11, 13, 23

[17] S. Schorr. The crystal structure of kesterite type compounds: A neutron and X-ray diffraction study. *Solar Energy Materials and Solar Cells*, 95(6):1482–1488, 2011. 10, 12, 23

[18] M. Ichimura and Y. Nakashima. Analysis of atomic and electronic structures of Cu_2ZnSnS_4 based on first-principle calculation. *Japanese Journal of Applied Physics*, 48(9):090202, 2009. 11, 12, 13

[19] S. Chen, X.G. Gong, A. Walsh, and S.-H. Wei. Crystal and electronic band structure of Cu_2ZnSnX_4 (X=S and Se) photovoltaic absorbers: First-principles insights. *Applied Physics Letters*, 94(4), 2009. 13, 14

[20] C. Persson. Electronic and optical properties of Cu_2ZnSnS_4 and $Cu_2ZnSnSe_4$. *Journal of Applied Physics*, 107(5):1–8, 2010. 14

[21] T. Maeda, S. Nakamura, and T. Wada. Phase stability and electronic structure of In-free photovoltaic semiconductors, $Cu_2ZnSnSe_4$ and Cu_2ZnSnS_4 by first-principles calculation. *MRS Proceedings*, 1165:137–143, 2010. 14

[22] S. Botti, D. Kammerlander, and M.A.L. Marques. Band structures of Cu_2ZnSnS_4 and $Cu_2ZnSnSe_4$ from many-body methods. *Applied Physics Letters*, 98(24), 2011. 14

[23] Sir Chandrasekhara Venkata Raman: Nobel prize 1930. `http://www.nobelprize.org/nobel_prizes/physics/laureates/1930`. 15

[24] I.R. Lewis and H. Edwards. *Handbook of Raman spectroscopy: from the research laboratory to the process line*. CRC Press, 2001. 15

[25] P.Y. Yu and M. Cardona. *Fundamentals of semiconductors: physics and materials properties*. Springer Berlin Heidelberg, 1999. 16, 33

[26] D.A. Long. *Quantum Mechanical Theory of Rayleigh and Raman Scattering*. Wiley Online Library, 2002. 17

[27] Bilbao crystallographic server. `http://www.cryst.ehu.es/`. 19, 91

[28] M.I. Aroyo, A. Kirov, C. Capillas, J.M. Perez-Mato, and H. Wondratschek. Bilbao crystallographic server. II. representations of crystallographic point groups and space groups. *Acta Crystallographica Section A*, 62:115–128, 2006. 19, 22, 23, 38, 91

[29] M.I. Aroyo, J.M. Perez-Mato, C. Capillas, E. Kroumova, S. Ivantchev, G. Madariaga, A. Kirov, and H. Wondratschek. Bilbao crystallographic server: I. databases and crystallographic computing programs. *Zeitschrift Fur Kristallographie*, 221(1):15–27, 2006. 19, 22, 23, 38, 91

[30] B. Schrader. *Infrared and Raman spectroscopy*. Wiley VCH, 2008. 20, 21

[31] D.L. Rousseau, R.P. Bauman, and S.P.S. Porto. Normal mode determination in crystals. *Journal of Raman Spectroscopy*, 10(1):253–290, 1981. 21

[32] Bilbao crystallographic server: Raman mode determination. `http://www.cryst.ehu.es/rep/sam.html`. 22, 38

[33] University of California, Davis chemwiki. `http://chemwiki.ucdavis.edu/Physical_Chemistry/Spectroscopy/Vibrational_Spectroscopy/Raman_Spectroscopy`. 22

[34] Bilbao crystallographic server: Wyckoff positions. `http://www.cryst.ehu.es/cgi-bin/cryst/programs/nph-wp-list`. 23

[35] T.C. Damen, S.P.S. Porto, and B. Tell. Raman effect in zinc oxide. *Physical Review*, 142(2):570–574, 1966. 24

[36] Vector algebra online tools. `http://vectoralgebra.info/eulerianglesvector.html`. 25

[37] W. Hayes and R. Loudon. *Scattering of light by crystals*. Dover Publications, 1978. 26

[38] H. Richter, Z.P. Wang, and L. Ley. The one phonon Raman spectrum in microcrystalline silicon. *Solid State Communications*, 39(5):625–629, 1981. 27

[39] I.H. Campbell and P.M. Fauchet. The effect of microcrystal size and shape on the one phonon Raman spectra of crystalline semiconductors. *Solid State Communications*, 58(10):739–741, 1986. 27

[40] S.C. Singh, H.B. Zeng, C. Guo, and W. Cai. *Nanomaterials*. Wiley, 2012. 27

[41] T. Gürel, C. Sevik, and T. Cagin. Characterization of vibrational and mechanical properties of quaternary compounds Cu_2ZnSnS_4 and $Cu_2ZnSnSe_4$ in kesterite and stannite structures. *Physical Review B*, 84(20), 2011. 29, 30, 31, 87, 88, 106

[42] I. Camps, J. Coutinho, M. Mir, A.F.D. Cunha, M.J. Rayson, and P.R. Briddon. Elastic and optical properties of $Cu_2ZnSn(Se_xS_{1-x})_4$ alloys: Density functional calculations. *Semiconductor Science and Technology*, 27(11), 2012. 29, 88

[43] K.W. Adu, Q. Xiong, H.R. Gutierrez, G. Chen, and P.C. Eklund. Raman scattering as a probe of phonon confinement and surface optical modes in semiconducting nanowires. *Applied Physics A-Materials Science & Processing*, 85(3):287, 2006. 28

[44] K.W. Adu, H.R. Gutierrez, U.J. Kim, and P.C. Eklund. Inhomogeneous laser heating and phonon confinement in silicon nanowires:

A micro-Raman scattering study. *Physical Review B*, 73(15):155333, 2006. 28

[45] S. Piscanec, M. Cantoro, A.C. Ferrari, J.A. Zapien, Y. Lifshitz, S. T. Lee, S. Hofmann, and J. Robertson. Raman spectroscopy of silicon nanowires. *Physical Review B*, 68(24), 2003. 28

[46] H. Munder, C. Andrzejak, M.G. Berger, U. Klemradt, H. Luth, R. Herino, and M. Ligeon. A detailed Raman study of porous silicon. *Thin Solid Films*, 221(1-2):27–33, 1992. 28

[47] M. Grossberg, J. Krustok, K. Timmo, and M. Altosaar. Radiative recombination in $Cu_2ZnSnSe_4$ monograins studied by photoluminescence spectroscopy. *Thin Solid Films*, 517(7):2489–2492, 2009. 28

[48] N.B.M. Amiri and A. Postnikov. Electronic structure and lattice dynamics in kesterite-type $Cu_2ZnSnSe_4$ from first-principles calculations. *Physical Review B*, 82(20), 2010. 29, 30, 106

[49] A. Khare, B. Himmetoglu, M. Johnson, D.J. Norris, M. Cococcioni, and E.S. Aydil. Calculation of the lattice dynamics and Raman spectra of copper zinc tin chalcogenides and comparison to experiments. *Journal of Applied Physics*, 111(12), 2012. 29, 30, 31, 82

[50] M. Guc, S. Levcenko, V. Izquierdo-Roca, X. Fontané, E. Arushanov, and A. Pérez-Rodríguez. Polarized Raman scattering analysis of $Cu_2ZnSnSe_4$ and $Cu_2ZnGeSe_4$ single crystals. *Journal of Applied Physics*, 114(19), 2013. 30, 31, 112, 113, 114

[51] A. Khare, B. Himmetoglu, M. Cococcioni, and E.S. Aydil. First principles calculation of the electronic properties and lattice dynamics of $Cu_2ZnSn(S_{1-x}Se_x)_4$. *Journal of Applied Physics*, 111(12), 2012. 31

[52] P.U. Bhaskar, G.S. Babu, Y.B.K. Kumar, and V.S. Raja. Growth and characterization of $Cu_2ZnSnSe_4$ thin films by a two-stage process. *Solar Energy Materials and Solar Cells*, 115:181–188, 2013. 32, 109

[53] M. Altosaar, J. Raudoja, K. Timmo, M. Danilson, M. Grossberg, J. Krustok, and E. Mellikov. $Cu_2Zn_{1-x}Cd_x$ $Sn(Se_{1-y}S_y)_4$ solid solutions as absorber materials for solar cells. *Physica Status Solidi A*, 205(1):167–170, 2008. 32, 37, 59, 109

[54] A. Nagaoka, K. Yoshino, H. Taniguchi, T. Taniyama, and H. Miyake. Preparation of $Cu_2ZnSnSe_4$ single crystals from Sn solutions. *Journal of Crystal Growth*, 354(1):147–151, 2012. 32, 109

[55] A. Fairbrother, E. Saucedo, X. Fontané, V. Izquierdo-Roca, D. Sylla, M. Espindola-Rodriguez, F.A. Pulgarin-Agudelo, O. Vigil-Galan, and A. Pérez-Rodríguez. Preparation of 4.8% efficiency $Cu_2ZnSnSe_4$ based solar cell by a two step process. *Photovoltaic Specialists Conference (PVSC), 2012 38th IEEE*, pages 2679–2684, 2012. 32, 109

[56] D. Abou-Ras, T. Kirchartz, and U. Rau. *Advanced characterization techniques for thin film solar cells*. Wiley-VCH, 2011. 33, 34

[57] M. Dvorak, S.-H. Wei, and Z. Wu. Origin of the Variation of Exciton Binding Energy in Semiconductors. *Phys. Rev. Lett.*, 110:016402, 2013. 33

[58] U. Rau and S. Siebentritt. *Wide-gap chalcopyrites*. Springer, 2006. 34

[59] T. Schmidt, K. Lischka, and W. Zulehner. Excitation-power dependence of the near-band-edge photoluminescence of semiconductors. *Physical Review B*, 45(16):8989, 1992. 34

[60] E.M. Kartzmark. Models for the representation of four-component systems. *Journal of Chemical Education*, 57(2):125–126, 1980. 35

[61] G. Marcano, C. Rincón, S.A. López, G. Sánchez Pérez, J.L. Herrera-Pérez, J.G. Mendoza-Alvarez, and P. Rodríguez. Raman spectrum of monoclinic semiconductor. *Solid State Communications*, 151(1):84–86, 2011. 36, 37

[62] G. Marcano, C. Rincón, L.M. De Chalbaud, D.B. Bracho, and G. Sánchez Pérez. Crystal growth and structure, electrical, and optical characterization of the semiconductor Cu_2SnSe_3. *Journal of Applied Physics*, 90(4):1847–1853, 2001. 36, 37

[63] G.E. Delgado, A.J. Mora, G. Marcano, and C. Rincón. Crystal structure refinement of the semiconducting compound Cu_2SnSe_3 from X-ray powder diffraction data. *Materials Research Bulletin*, 38(15):1949–1955, 2003. 36, 37, 62

[64] E.J. Skoug, J.D. Cain, and D.T. Morelli. Thermoelectric properties of the Cu_2SnSe_3-Cu_2GeSe_3 solid solution. *Journal of Alloys and Compounds*, 506(1):18–21, 2010. 36

[65] G.H. Chandra, O.L. Kumar, R.P. Rao, and S. Uthanna. Influence of substrate and selenization temperatures on the growth of Cu_2SnSe_3 films. *Journal of Materials Science*, 46(21):6952–6959, 2011. 36

[66] G.S. Babu, Y.B.K. Kumar, Y.B.K. Reddy, and V.S. Raja. Growth and characterization of Cu_2SnSe_3 thin films. *Materials Chemistry and Physics*, 96(2-3):442–446, 2006. 36, 62

[67] J.A. Rivet. Contribution à l'étude de quelques combinaisons ternaires sulfurées, seleniées ou tellurées du cuivre avec les elements du groupe IV. *J. Ann. Chim.*, 10:243, 1965. 36

[68] G. Marcano, C. Rincón, G. Marín, R. Tovar, and G. Delgado. Crystal growth and characterization of the cubic semiconductor Cu_2SnSe_4. *Journal of Applied Physics*, 92(4):1811–1815, 2002. 36, 62

[69] B. Li, Y. Xie, J. Huang, and Y. Qian. Solvothermal synthesis to Cu_2SnSe_4 nanocrystals at low temperature. *Solid State Ionics*, 126(3):359–362, 1999. 36

[70] Z. Zainal, A. Kassim, M.Z. Hussein, and C.H. Ching. Effect of bath temperature on the electrodeposition of copper tin selenide films from aqueous solution. *Materials Letters*, 58(16):2199–2202, 2004. 36

[71] T.M. Khan, M.F. Mehmood, A. Mahmood, A. Shah, Q. Raza, A. Iqbal, and U. Aziz. Synthesis of thermally evaporated ZnSe thin film at room temperature. *Thin Solid Films*, 519(18):5971 – 5977, 2011. 37

[72] M. Arslan, A. Maqsood, A. Mahmood, and A. Iqbal. Structural and optical properties of copper enriched ZnSe thin films prepared by closed space sublimation technique. *Materials Science in Semiconductor Processing*, 16(6):1797–1803, 2013. 37

[73] N.K. Morozova, I.A. Karetnikov, V.V. Blinov, and E.M. Gavrishchuk. A study of luminescence centers related to copper and oxygen in ZnSe. *Semiconductors*, 35(1):24–32, 2001. 37, 69

[74] J.C. Irwin and J. LaCombe. Phonon dispersion in ZnSe. *Canadian Journal of Physics*, 50(21):2596–2604, 1972. 38, 108

[75] I. Lefebvre, M.A. Szymanski, J. Olivier-Fourcade, and J.C. Jumas. Electronic structure of tin monochalcogenides from SnO to SnTe. *Physical Review B*, 58(4):1896–1906, 1998. 38

[76] H.S. Soliman, D.A. Abdel Hady, K.F. Abdel Rahman, S.B. Youssef, and A.A. El-Shazly. Optical properties of tin-selenide films. *Physica A: Statistical Mechanics and its Applications*, 216(1-2):77–84, 1995. 38

[77] H.R. Chandrasekhar, R.G. Humphreys, U. Zwick, and M. Cardona. Infrared and Raman spectra of the IV-VI compounds SnS and SnSe. *Physical Review B*, 15:2177–2183, Feb 1977. 38, 39

[78] D.G. Mead and J.C. Irwin. Raman spectra of SnS_2 and $SnSe_2$. *Solid State Communications*, 20(9):885 – 887, 1976. 39

[79] K.-M. Chung, D. Wamwangi, M. Woda, M. Wuttig, and W. Bensch. Investigation of SnSe, $SnSe_2$, and Sn_2Se_3 alloys for phase change memory applications. *Journal of Applied Physics*, 103(8):083523, 2008. 39

[80] K. Bindu and P.K. Nair. Semiconducting tin selenide thin films prepared by heating Se-Sn layers. *Semiconductor Science and Technology*, 19(12):1348–1353, 2004. 39

[81] D.J. Gardiner, P.R. Graves, and H.J. Bowley. *Practical Raman Spectroscopy*, volume 21. Springer-Verlag Heidelberg, Germany, 1989. 43

[82] J.J. Scragg, D.M. Berg, and P.J. Dale. A 3.2% efficient kesterite device from electrodeposited stacked elemental layers. *Journal of Electroanalytical Chemistry*, 646(12):52–59, 2010. 46

[83] A. Weber, R. Mainz, and H.W. Schock. On the Sn loss from thin films of the material system Cu-Zn-Sn-S in high vacuum. *Journal of Applied Physics*, 107(1), 2010. 47, 48

[84] A. Redinger, D.M. Berg, P.J. Dale, and S. Siebentritt. The consequences of kesterite equilibria for efficient solar cells. *Journal of the American Chemical Society*, 133(10):3320–3323, 2011. 47, 48

[85] M. Mousel, T. Schwarz, R. Djemour, T.P. Weiss, J. Sendler, J.C. Malaquias, A. Redinger, O. Cojocaru-Mirédin, P.-P. Choi, and S. Siebentritt. Cu-rich precursors improve kesterite solar cells. *Advanced Energy Materials*, 4, 2013. 49, 67, 68

[86] P. Hovington, D. Drouin, and R. Gauvin. CASINO: A new monte carlo code in C language for electron beam interaction part I: Description of the program. *Scanning*, 19(1):1–14, 1997. 50

[87] P. Villars, A. Prince, and H. Okamoto. *Handbook of ternary alloy phase diagrams*, volume 5. ASM International, 1995. 54, 55

[88] A. Redinger, R. Djemour, T.P. Weiss, J. Sendler, and S. Siebentritt. Raman scattering as a probe of phonon confinement and surface optical

modes in semiconducting nanowires. *Proc. 39th IEEE PV Specialist Conference, Tampa*, 2013. 56

[89] A.J. Smith, P.E. Meek, and W.Y. Liang. Raman scattering studies of SnS_2 and $SnSe_2$. *Journal of Physics C: Solid State Physics*, 10(8):1321, 1977. 59, 64

[90] I. Bonev. On the terminology of the phenomena of mutual crystal orientation. *Acta Crystallographica Section A*, 28(6):508–512, Nov 1972. 61

[91] N. Beigom Mortazavi Amiri and A. Postnikov. Secondary phase Cu_2SnSe_3 vs. kesterite $Cu_2ZnSnSe_4$: Similarities and differences in lattice vibration modes. *Journal of Applied Physics*, 112(3), 2012. 61, 62, 63

[92] S. Siebentritt and S. Schorr. Kesterites - a challenging material for solar cells. *Progress in Photovoltaics*, 20(5):512–519, 2012. 62, 90

[93] A. Redinger, M. Mousel, R. Djemour, L. Gütay, N. Valle, and S. Siebentritt. $Cu_2ZnSnSe_4$ thin film solar cells produced via co-evaporation and annealing including a $SnSe_2$ capping layer. *Progress in Photovoltaics: Research and Applications*, 2013. 63, 69

[94] G. Lucovsky, A. Mooradian, W. Taylor, G.B. Wright, and R.C. Keezer. Identification of the fundamental vibrational modes of trigonal, monoclinic and amorphous selenium. *Solid State Communications*, 5(2):113 – 117, 1967. 65

[95] R.C. Sharma and Y.A. Chang. The Se-Sn (selenium-tin) system. *Bulletin of Alloy Phase Diagrams*, 7(1):68–72, 1986. 65

[96] H. Wiedemeier and G. Pultz. Equilibrium sublimation and thermodynamic properties of SnSe and $SnSe_2$. *Zeitschrift für anorganische und allgemeine Chemie*, 499(4):130–144, 1983. 65

[97] S. Chen, A. Walsh, X.G. Gong, and S.H. Wei. Classification of lattice defects in the kesterite Cu_2ZnSnS_4 and $Cu_2ZnSnSe_4$ earth-abundant solar cell absorbers. *Advanced Materials*, 25(11):1522–1539, 2013. 67

[98] R. Djemour, A. Redinger, L. Gütay, M. Mousel, A. Crossay, D. Colombara, P.J. Dale, and S. Siebentritt. Detecting ZnSe secondary phase in $Cu_2ZnSnSe_4$ by room temperature photoluminescence. *Applied Physics Letters*, 102(22), 2013. 67

[99] A. Redinger, D.M. Berg, P.J. Dale, R. Djemour, L. Gütay, T. Eisenbarth, N. Valle, and S. Siebentritt. Route toward high-efficiency single-phase $Cu_2ZnSnSe$. *IEEE Journal of Photovoltaics*, 1(2):200–206, 2011. 67, 69

[100] T. Schwarz, O. Cojocaru-Mirédin, P.-P. Choi, M. Mousel, A. Redinger, S. Siebentritt, and D. Raabe. Atom probe study of $Cu_2ZnSnSe_4$ thin-films prepared by co-evaporation and post-deposition annealing. *Applied Physics Letters*, 102(4):042101–042104, 2013. 67, 68, 69, 82, 121

[101] S. Ahn, S. Jung, J. Gwak, A. Cho, K. Shin, K. Yoon, D. Park, H. Cheong, and J.H. Yun. Determination of band gap energy (E_g) of $Cu_2ZnSnSe_4$ thin films: On the discrepancies of reported band gap values. *Applied Physics Letters*, 97(2), 2010. 68

[102] S. Bag, O. Gunawan, T. Gokmen, Y. Zhu, T.K. Todorov, and D.B. Mitzi. Low band gap liquid-processed CZTSe solar cell with 10.1% efficiency. *Energy and Environmental Science*, 5:7060–7065, 2012. 68

[103] N.K. Morozova, I.A. Karetnikov, V.V. Blinov, and E.M. Gavrishchuk. Studies of the infrared luminescence of ZnSe doped with copper and oxygen. *Semiconductors*, 35(5):512–515, 2001. 69

[104] G.B. Stringfellow and R.H. Bube. Photoelectronic properties of ZnSe crystals. *Physical Review*, 171(3):903–915, 1968. 69

[105] E. Mellikov, M. Altosaar, M. Krunks, J. Krustok, T. Varema, O. Volobujeva, M. Grossberg, L. Kaupmees, T. Dedova, K. Timmo, K. Ernits, J. Kois, I.O. Acik, M. Danilson, and S. Bereznev. Research in solar cell technologies at Tallinn University of Technology. *Thin Solid Films*, 516(20):7125–7134, 2008. 70

[106] J.L. Rodgers and W.A. Nicewander. Thirteen ways to look at the correlation coefficient. *The American Statistician*, 42(1):59–66, 1988. 72

[107] R. Djemour, A. Redinger, M. Mousel, L. Gütay, X. Fontané, V. Izquierdo-Roca, A. Pérez-Rodríguez, and S. Siebentritt. The three A symmetry Raman modes of kesterite in $Cu_2ZnSnSe_4$. *Optics Express*, 21:A695–A703, 2013. 78

[108] E. Rudigier, T. Enzenhofer, and R. Scheer. Determination of the quality of $CuInS_2$-based solar cells combining Raman and photoluminescence spectroscopy. *Thin Solid Films*, 480:327–331, 2005. 80

[109] A.L. Stancik and E.B. Brauns. A simple asymmetric lineshape for fitting infrared absorption spectra. *Vibrational Spectroscopy*, 47(1):66–69, 2008. 80, 103

[110] X. Fontané, V. Izquierdo-Roca, E. Saucedo, S. Schorr, V.O. Yukhymchuk, M.Y. Valakh, A. Pérez-Rodríguez, and J.R. Morante. Vibrational properties of stannite and kesterite type compounds: Raman scattering analysis of $Cu_2(Fe,Zn)SnS_4$. *Journal of Alloys and Compounds*, 539(0):190–194, 2012. 82

[111] P.K. Sarswat, M.L. Free, and A. Tiwari. Temperature-dependent study of the Raman A mode of Cu_2ZnSnS_4 thin films. *Physica Status Solidi B-Basic Solid State Physics*, 248(9):2170–2174, 2011. 83

[112] M. Grossberg, J. Krustok, J. Raudoja, K. Timmo, M. Altosaar, and T. Raadik. Photoluminescence and Raman study of $Cu_2ZnSn(Se_xS_{1-x})_4$ monograins for photovoltaic applications. *Thin Solid Films*, 519(21):7403–7406, 2011. 85

[113] S. Adachi. *Physical properties of III-V semiconductor compounds*. Wiley. com, 1992. 91

[114] T. Sander, S. Eisermann, B.K. Meyer, and P.J. Klar. Raman tensor elements of wurtzite ZnO. *Physical Review B*, 85:165208, Apr 2012. 104

[115] B. Shin, Y. Zhu, N.A. Bojarczuk, S. Jay Chey, and S. Guha. Control of an interfacial $MoSe_2$ layer in $Cu_2ZnSnSe_4$ thin film solar cells: 8.9% power conversion efficiency with a TiN diffusion barrier. *Applied Physics Letters*, 101(5), 2012. 116, 117, 118

[116] A.M. Hermann and L. Fabick. Research on polycrystalline thin-film photovoltaic devices. *Journal of Crystal Growth*, 61(3):658–664, 1983. 119

[117] A. Redinger, K. Hoenes, X. Fontané, V. Izquierdo-Roca, E. Saucedo, N. Valle, A. Pérez-Rodríguez, and S. Siebentritt. Detection of a ZnSe secondary phase in coevaporated $Cu_2ZnSnSe_4$ thin films. *Applied Physics Letters*, 98(10), 2011. 121

[118] M. Mousel, A. Redinger, R. Djemour, M. Arasimowicz, N. Valle, P.J. Dale, and S. Siebentritt. HCl and Br_2-MeOH etching of $Cu_2ZnSnSe_4$ polycrystalline absorbers. *Thin Solid Films*, 535(1):83–87, 2013. 121

[119] G. Brammertz, Y. Ren, M. Buffiére, S. Mertens, J. Hendrickx, H. Marko, A. E. Zaghi, N. Lenaers, C. Köble, J. Vleugels, M. Meuris, and J. Poortmans. Electrical characterization of $Cu_2ZnSnSe_4$ solar cells from selenization of sputtered metal layers. *Thin Solid Films*, 2012. 122

[120] V. Deprédurand, Y. Aida, J. Larsen, T. Eisenbarth, A. Majerus, and S. Siebentritt. Surface treatment of CIS solar cells grown under Cu-excess. *Conference record of the IEEE Photovoltaic Specialists Conference*, pages 000337–000342, 2011. 122

[121] R. Klenk and H.W. Schock. Photocurrent collection in thin film solar cells calculation and characterization for $CuGaSe_2$/(Zn,Cd)S. *Proceedings of the 12th European Photovoltaic Solar Energy Conference*, pages 1588–1591, 1994. 122

[122] E. Lotter. Diplot, 2009. 123

[123] S. Siebentritt, L. Gütay, D. Regesch, Y. Aida, and V. Deprédurand. Why do we make Cu(In,Ga)Se_2 solar cells non-stoichiometric? *Solar Energy Materials and Solar Cells*, 119:18–25, 2013. 123

[124] U. Rau and J.H. Werner. Radiative efficiency limits of solar cells with lateral band-gap fluctuations. *Applied Physics Letters*, 84(19):3735–3737, 2004. 124

Publication List

1. R. Djemour, A. Redinger, M. Mousel, L. Gütay, and S. Siebentritt. Multiple phases of $Cu_2ZnSnSe_4$ detected by room-temperature photoluminescence. *submitted*, 2014.

2. R. Djemour, L. Gütay, I. Riedel, C. Stroth, A. Redinger and S. Siebentritt. Vibrational properties of CZTSe. *in preparation*, 2014.

3. R. Djemour, A. Redinger, M. Mousel, L. Gütay, X. Fontané, V. Izquierdo-Roca, A. Pérez-Rodríguez, and S. Siebentritt. The three A symmetry Raman modes of kesterite in $Cu_2ZnSnSe_4$. *Optics Express*, 21(13), pp. A695-A703, 2013.

4. R. Djemour, A. Redinger, L. Gütay, M. Mousel, A. Crossay, D. Colombara, P.J. Dale and S. Siebentritt. Detecting ZnSe secondary phase in $Cu_2ZnSnSe_4$ by room temperature photoluminescence. *Applied Physics Letters*, 102(22), 222108, 2013.

5. D. Colombara, E.V.C. Robert, A. Crossay, A. Taylor, M. Guennou, M. Arasimowicz, J.C.B. Malaquias, R. Djemour, P.J. Dale. Quantification of surface ZnSe in $Cu_2ZnSnSe_4$-based solar cells by analysis of the spectral response. *Solar Energy Materials and Solar Cells*, 123, pp. 220-227, 2014.

6. M. Mousel, T. Schwarz, R. Djemour, T.P. Weiss, J. Sendler, J.C. Malaquias, A. Redinger, O. Cojocaru-Mirédin, P.-P. Choi, and S. Siebentritt. Cu-rich precursors improve kesterite solar cells. *Advanced Energy Materials*, 4(2), 1300543, 2014, .

7. A. Redinger, M. Mousel, R. Djemour, L. Gütay, N. Valle, S. Siebentritt. $Cu_2ZnSnSe_4$ thin film solar cells produced via co-evaporation and annealing including a $SnSe_2$ capping layer. *Progress in Photovoltaics: Research and Applications*, 22 (1), pp. 51-57, 2014.

8. M. Mousel, A. Redinger, R. Djemour, M. Arasimowicz, N. Valle, P.J. Dale, S. Siebentritt. HCl and Br_2-MeOH etching of $Cu_2ZnSnSe_4$ polycrystalline absorbers. *Thin Solid Films*, 535 (1), pp. 83-87, 2013.

9. M. Steichen, R. Djemour, L. Gütay, J. Guillot, S. Siebentritt, P.J. Dale. Direct synthesis of single-phase p-type SnS by electrodeposition from a dicyanamide ionic liquid at high temperature for thin film solar cells. *Journal of Physical Chemistry C*, 117 (9), pp. 4383-4393, 2013.

10. A. Redinger, R. Djemour, T.P. Weiss, J. Sendler, and S. Siebentritt. Raman scattering as a probe of phonon confinement and surface optical modes in semiconducting nanowires. *Proc. 39th IEEE PV Specialist Conference, Tampa*, 2013.

11. D.M. Berg, R. Djemour, L. Gütay, G. Zoppi, S. Siebentritt, P.J. Dale. Thin film solar cells based on the ternary compound Cu_2SnS_3. *Thin Solid Films*, 520 (19), pp. 6291-6294, 2012.

12. D.M. Berg, R. Djemour, L. Gütay, S. Siebentritt, P.J. Dale, X. Fontané, V. Izquierdo-Roca, A. Pérez-Rodriguez. Raman analysis of monoclinic Cu_2SnS_3 thin films. *Applied Physics Letters*, 100(19), 192103, 2012.

13. L. Gütay, A. Redinger, R. Djemour, S. Siebentritt. Lone conduction band in $Cu_2ZnSnSe_4$. *Applied Physics Letters*, 100(10), 102113, 2012

14. A. Redinger, D.M. Berg, P.J. Dale, R. Djemour, L. Gütay, T. Eisenbarth, N. Valle, and S. Siebentritt. Route toward high-efficiency single-phase $Cu_2ZnSnSe$. *IEEE Journal of Photovoltaics*, 1(2):200–206, 2011.

15. A. Redinger, J. Sendler, R. Djemour, T.P. Weiss, G. Rey S. Siebentritt. Different bandgaps in $Cu_2ZnSnSe_4$: A high temperature coevaporation study. *submitted*, 2014.

16. D. Berg, M. Arasimowicz, R. Djemour, L. Gütay, S. Siebentritt, S. Schorr, X. Fontané, V. Izquierdo-Roca, A. Pérez-Rodríguez and P.J. Dale. Discrimination and detection limits of secondary phases in Cu_2ZnSnS_4 using X-ray diffraction and Raman spectroscopy *submitted*, 2014.

17. H.J. Meadows, J. Malaquias, M. Steichen, R. Djemour, D. Regesch, A. Malyeyev, M. Kurihara, A.A. Taylor, B.G. Mendes, S. Siebentritt and P.J. Dale. On the relationship between the composition and morphology of electrodeposited Cu/Ga/In precursors and the properties of the resulting $Cu(In,Ga)Se_2$ absorber layers *submitted*, 2014.

Acknowledgments

I would like to start to thank Alejandro Pérez Rodríguez for being in my CET committee, (I especially appreciated the fast and thorough paper review) as well as Jens Kreisel and Yaroslav Romanyuk for being in the jury. I hope you did not groan too much while reading my thesis!

I am especially grateful to my supervisor Susanne Siebentritt for the possibility of doing my thesis in this interesting field. Thank you for your help, patience and guidance over the years. Thank you for always having an open door.

To the "Auto-meeting Team" (Tobias, Alex and Levent): for the fabulous introduction and animated discussions. Thank you Levent for tuning my skills in the dark art of optics. Thank you Alex and Levent for the help with the first interpretation of the 1.4 eV PL. Thank you Alex for always offering a sounding-board for all my ideas and questions. Thanks for guidance in many things.

A big thank you goes to the whole LPV/LEM team for a fun time during my years with you all. Additionally to those already mentioned I am especially grateful to: Dominik Berg, Marina Mousel, Alex Redinger, Monica Arasimowicz and Alexandre Crossay for the interesting samples ;), Maxim Thevenin for the SEM measurements, Professors Thomas (Schuler) for his technical help and entertainment, Danielle Schoder and Patricia Ramoa for taking exellent care of everybody, to David for lab sharing and smoking, to Mael Guennou for Raman advice, to Mads Weber for being a good Raman buddy, to Marc Steichen for fruitful discussions and advice (also outside of work), to Nathalie Valle for SIMS measurements, to the Barcelona team with Alexandro Pérez-Rodríguez, Victor Izquierdo-Roca and Xavier Fontané for Polarized Raman measurements, to Christiane Stroth and Levent Gütay at the University of Oldenburg for the P/O Raman measurements.

Many thanks also goes to my friends for support and encouragement, especially Andrej, Gregor, Jürgen and Matthias.

Thanks to my brothers, sisters, god parents, grand parents, and birth parents for everything. Thanks to my Anna for help, support, understanding

and much more.